Università di Roma Tre

SCUOLA DOTTORALE IN SCIENZE MATEMATICHE E FISICHE
DOTTORATO IN FISICA

XXVII ciclo

A novel *on-line* dose monitoring technique tailored for Particle Therapy

Dottorando: Ilaria Mattei
Docente: Filippo Ceradini
Coordinatore: Roberto Raimondi

Particle Therapy (PT) is a technique that exploits accelerated charged ions for the treatment of solid cancers. The irradiation accuracy and the conformity achievable with charged particles beams help to minimize damage to the surrounding healthy tissues and Organs At Risk (OAR) in tumor proximity. To fully take advantage of the improved therapy spatial selectiveness a novel monitoring technique is required in order to provide *on-line* a high precision feedback on the position of the maximum dose release, the Bragg Peak (BP), during the treatment.
In the present PhD thesis a novel on-line dose monitoring technique to be applied in particle therapy treatments is described.

The first part of the work concerned the study of the secondary radiation produced in the interactions of hadron beams of therapeutical energies with PMMA phantoms.
Several experiments have been performed at the INFN Laboratori Nazionali del Sud (LNS-INFN, Catania, Italy) with a 80 MeV/u ^{12}C beam and at the GSI laboratory (Darmstadt, Germany) with a 220 MeV/u ^{12}C beam in order to measure the production yields and energy spectra of secondary particles such as prompt photons and secondary charged fragments. Secondary charged particles have been measured for the first time at large angles (90° and 60°) with respect to the beam direction and a technique based on the reconstruction of the secondary charged fragments emission profile has been developed in order to relate such profile to the Bragg peak position. A clear correlation between the charged particles emission profile falling edge and the BP position inside the target has been observed and two parameters characterizing the charged profile have been proposed to monitor the maximum dose release. Moreover, the correlation between the rising edge of the charged fragments emission distribution and the beam entrance position inside the target has been proved.

Dedicated simulations with the FLUKA Monte Carlo code have been also performed and mainly used to drive the secondary charged particles identification. Preliminary results are also shown for the experiment performed at the HIT center (Heidelberg, Germany) with Helium ion beams (102 MeV/u, 125 MeV/u, 145 MeV/u) and Oxygen ion beams (210 MeV/u, 300 MeV/u).
All the performed measurements suggest that the rate of produced protons and prompt photons is large enough to supply the particle sample needed for a fast on-line monitor operating during a treatment, with the capability to provide the required $\mathcal{O}$(mm) spatial resolution.

In the second part of this contribution a novel on-line dose monitoring technique based on the simultaneous detection of secondary neutral and charged particles is presented. A dual-mode device, named *Dose Profiler* (DP), is under construction at SBAI department laboratory (Sapienza University, Rome, Italy). Working as a Compton camera and a secondary charged particles tracker, the Dose Profiler principal aim is to provide a prompt feedback on the quality of the treatment during the patient irradiation time. The main DP constituents are the tracker, composed of six planes of orthogonal tracking layers of scintillating fibers, an electron absorber, made of plastic scintillator, and a LYSO calorimeter. Such devices have been designed to track both photons and charged particles during a PT treatment, measuring the secondary particles emission distribution and correlating it to the dose release inside the patient. A preliminary evaluation of the detector performances has been done using a dedicated full FLUKA Monte Carlo simulation.
The Dose Profiler device has been developed as part of the INSIDE project (P.R.I.N. of italian Ministry of University and Research) aiming to build a prototype of a combined multi-mode on-line dose release monitor, compact and manageable, that will be integrated in a treatment room at the CNAO center in Pavia (Italy) starting in 2016.

ROMA TRE
UNIVERSITÀ DEGLI STUDI

SCUOLA DOTTORALE IN SCIENZE MATEMATICHE E FISICHE
DOTTORATO IN FISICA

XXVII CICLO

A novel *on-line* dose monitoring technique tailored for Particle Therapy

Dottorando: Ilaria Mattei

Docente: Prof. Filippo Ceradini

Coordinatore: Prof. Roberto Raimondi

A mio fratello

Che tu sia sempre tra i *Felici Pochi*
la cui infelicità è allegra,
mentre la felicità degli *Infelici Molti*
è triste da asfissiare.

Contents

Introduction

According to the World Health Organization (WHO), cancer is one of the major death causes in the high-income countries. Treatment options depend on the type of cancer, its stage, the cancer spread over the patient body and on the patient general health. The main solid tumors treatments are surgery, that attempts for a direct removal of the tumor, and radiation therapy (RT), using X-rays for killing cancer cells. Chemotherapy is another technique that employs chemical vectors to kill cancer cells, that can be used in a systemic or regional way, depending on whether the drugs travel through the bloodstream to reach cells throughout the body or they are directed to a specific area, respectively. Radiation therapy can be applied in combined modalities: for example, chemo-radiotherapy can be used in order to shrink a tumor volume and then treat it, while, after surgery, radiotherapy is used as an adjuvant treatment.

Since the goal of a treatment is to kill as many cancerous cells while minimizing the damage to normal cells nearby, in order to minimize also side effects and complications, sometimes surgery, as well as radiation therapy, is not permitted due to the tumor localization close to organs at risk.
The Intensity Modulated Radiation Therapy (IMRT) is, at present, the pioneering technology in traditional RT (photons or electrons). IMRT uses six up to nine non coplanar X-ray fields combined with multi-leaves collimator and CT imaging. Modulating and controlling the intensity of the radiation beam in multiple small volumes involving different X-ray fields, the IMRT technique enables the possibility to achieve a custom tailored radiation dose very conformal to the tumor region, while helping to spare the healthy tissues and organs at risk in tumor proximity.

In recent years, the rapid advance in technology has led to the evolution of radiation oncology techniques. About sixty years ago, an alternative to the traditional radiotherapy involving X-rays has been proposed: the *hadrontherapy*. Hadrontherapy, or *Particle Therapy* (PT), employs hadrons (from the greek *adrós*, strong), which are composite particles made of quarks held together by the strong force. The advantage of using these particles in cancer treatment with respect to X-rays is due to their peculiar mechanism of energy loss in matter. The hadrons released energy per unit mass (*dose*), that is related to the cells killing power, is very low at the beginning of the tissues penetration and it's maximum at the end of the particle range, in a narrow region called the *Bragg peak*. Instead, the X-rays dose release follows an exponential decrease distribution as a function of the depth into the absorbing medium, with a non negligible dose released to healthy tissues surrounding the tumor. Another advantage in using hadrons is their high biological damage with respect to X-rays, especially for light ions (α, ^{12}C ...). X-rays passing through matter

have a low ionization density, producing free-radicals and then inducing the cells damage mostly in an indirect way. Instead, light ions are characterized by a high ionization density which is maximum at the Bragg peak, producing direct breaks of the DNA helix (*strand breaks* or *double strand breaks*) causing the cells death. Hence, since free-radicals are produced in well oxygenated tumor areas, hypoxic tumors, for example, turn out to be *radioresistant* to traditional RT, that becomes less effective in such cases with respect to particle therapy.

The use of hadrons in radiotherapy allows for a very selective dose release, capable of destroying cancerous cells with high efficiency and preserving the surrounding healthy tissues. Therefore, hadrontherapy is a particularly suitable technique to treat deep and radioresistant tumors close to organs at risk. On the other hand, due to the high localization of the Bragg peak, the dose release monitoring over the tumor volume in particle therapy is highly requested in order to assess the beam range inside tissues and verify the PT treatment effectiveness.

Nowadays, there are many centers all over the world using particle therapy for tumor treatment, involving mainly protons and, as a recent development, also carbon ion beams. In order to allow for a widespread clinical use of the particle therapy, a huge effort should be devoted to improve the dose monitoring devices and techniques. As of today, the only dose monitoring technique that has been attempted even on an experimental basis is the *off-line PET*, the Positron Emission Tomography used after the PT treatment, based on the detection of *back to back* photons (*PET photons*) produced in the positrons annihilation following a radioactive isotope beta decay. Such isotopes are created by the interactions of the hadron beam with the target. The PET based monitoring technique suffers, mainly, for the reduced statistics available that limits the imaging resolution achievable.

New methods, based on the detection of secondary fragments produced in the nuclear interactions of the hadron beam projectiles with the target nuclei, aiming for an *on-line* dose release monitoring capable of being operated during the radiation treatment, are under study. The secondary particles available for such studies, emitted within few nanoseconds from the time of interaction, can be either prompt photons or charged particles.

The work presented in this thesis describes a novel approach for an on-line dose release monitoring in PT treatments. In Chapter 1 I will first review the basics of the interaction of radiation with matter for the particles of interest of this work. In Chapter 2 I will introduce the particle therapy and its physical and biological specific variables, while in Chapter 3 I will describe in detail the characteristics of the secondary fragments produced in PT treatments, as well as their detection techniques. Chapter 4 is dedicated to the experiments performed to characterize the secondary particles production from carbon ion beams impinging on a 'human like' target. The energy spectrum and the flux of secondary radiation, such as prompt photons and secondary charged particles, have been measured and a clear correlation between the secondary charged particles emission profile and the Bragg peak position has been observed. The obtained results fully support the feasibility of a novel on-line dose monitoring technique based on the simultaneous detection of secondary neutral and charged radiation.
In Chapter 5 I will outline the *Dose Profiler* project. The Dose Profiler (DP) is a

dual-mode device designed to track both neutral and charged particles during the hadrontherapy treatment, in order to measure the emission distribution of secondary fragments and relate it to the beam dose release inside the patient.
The DP is under construction and it has been developed as part of the INSIDE project aiming for a combined multi-mode on-line dose release monitor, compact and manageable, that will be integrated in a treatment room at the CNAO center in Pavia (Italy) in 2016.

Chapter 1

Radiation interaction with matter

The interaction of radiation with matter is a topic of outmost importance. In the last decades, it has driven the effort of both experimentalists and theoreticians in order to improve the knowledge of interaction mechanisms and allow a widespread of techniques and applications that are related to such phenomena. The design and characterization of novel radiation detection techniques, the optimization of radiation shielding materials and the implementation of radiation techniques for tumor treatments are all examples of such applications.
Depending on the radiation type, energy and target material, radiation interaction with matter is driven by quantum mechanics, that rules the propagation of radiation through matter and its detection characteristics, as well as its effects on a biological organism. Some typical processes undergone by neutral or charged radiation when passing through matter are the electromagnetic interactions and inelastic collisions with the atomic electrons. In particular, charged radiation has to be distinguished in light and heavy charged radiation, such as electrons and positrons with respect to protons, alpha particles and other ions.

Since this thesis mainly concerns medical physics application, in this chapter it will be discussed the interactions of radiation with matter that are of interest in this field.

1.1 Heavy charged particles

In this section the passage of heavy charged particles through matter is discussed, with special emphasis on the exchange of energy between the projectile particles and the target and on the deflections from the incident direction.
A charged particle impinging on a material makes collisions with the target atomic electrons and nuclei. For particles heavier than electrons, the mentioned collisions have different consequences. When entering any absorber the charged particle simultaneously interacts with many electrons, and each electron is affected by the impulse due to the Coulomb force as the heavy charged particle passes nearby. Therefore, the electron can take up an appreciable amount of energy from the incident particle, rising up to a higher-lying shell within the atom, or the atom

can undergo ionization, when the electron is completely removed from the atom, depending on the closeness of the interaction. No significantly deflections of the primary particle trajectory will be observed, as the electron mass is much smaller than the heavy charged particle mass. Whereas, when the collisions are with the target nuclei, those absorb a very little amount of energy, since the mass of the target nuclei is usually much bigger compared to the mass of the incident particle. Because of their greater charge, massive nuclei scatter the incident particle, causing particle deflections on the trajectory that are anyhow confined to small angles. Thus, the energy loss by the heavy charged particle occurs almost entirely in collisions with electrons. Other processes responsible for the particle energy loss are the emission of Cherenkov radiation, nuclear reactions, and bremsstrahlung that are extremely rare with respect to the atomic collisions processes, so they will not be discussed in this chapter (except for the nuclear fragmentation).

When the heavy charged particle loses its energy, there is a consequent decrease of its velocity. The maximum energy that can be transferred to an electron of mass m_e in a single collision from a charged particle of mass M with a kinetic energy T is actually small and equal to $4Tm_e/M$. On the other hand, many collisions occur per unit path length, so a substantial energy loss is observed even for thin layers of material, producing a continuous decrease of particle's velocity until the particle is even stopped. As already mentioned, the number of collisions per unit path length is usually large, causing the collisions to be statistical. Since the fluctuations in the total energy loss are small, it is possible to work with the average energy loss per unit path length, the so called *stopping power* dE/dx. This quantity was first calculated by Bohr using classical mechanics while Jackson has evaluated a simplified version (*Jackson* [1]), followed by the quantum mechanics approach of *Bethe and Ashkin* [2].

1.1.1 The Bethe-Bloch formula

When a heavy charged particle of charge ze and mass M collides with an atomic electron, if the particle velocity is greater than the electron orbital velocity, during the collision the bounded atomic electron can be treated as free and initially at rest. The momentum transfer can be assumed to be sufficiently small, so the particle trajectory is essentially not deflected and the recoiling electron does not move during the interaction. Another approximation is that the particle's magnetic interaction is negligible, since the relative velocity is small. The geometry of the collision is shown in Figure 1.1, where a particle of mass M, charge ze and velocity v passes near an electron of mass m ($m \ll M$) and charge e at an impact parameter b.

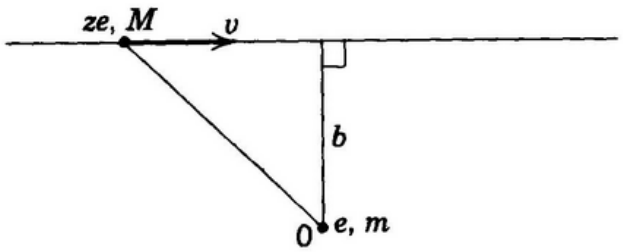

Figure 1.1. Scheme of a collision between a heavy charged particle and an atomic electron.

The approximated formula for the energy loss as evaluated by *Jackson* [1] express all the features of the classical result due to Bohr (1915):

$$-\frac{dE}{dx} = \frac{4\pi z^2 e^4}{mc^2\beta^2} n \ln \frac{mc^2\beta^2\gamma^2}{\hbar\langle\omega\rangle} \tag{1.1}$$

where E is the particle energy, x the particle's travelled distance in the medium, $\beta = v/c$ with v the particle's velocity and c the speed of light, z is the particle's charge, e the electron charge ($e^2 = 1.44\ MeV\ fm$, it contains $4\pi\epsilon_0$) and m the electron rest mass; $n = \frac{N_A \rho Z}{A}$ is the electron density with N_A the Avogadro constant ($6.022045 \times 10^{23}\ mol^{-1}$), Z and A respectively the atomic and mass number and ρ the density of the absorber material; $\gamma = (\sqrt{1-\beta^2})^{-1}$ is the Lorentz factor, $\hbar$ is the reduced Planck constant and $\langle\omega\rangle$ is the average electron revolution frequency. It has to be underlined that for light charged particles as protons, the classical formula of the stopping power does not work properly, even if it contains all the description of the electronic collision loss. Thus, quantum effects have been taken into account and a complete quantum mechanical calculation of the energy loss has been performed by Bethe, Bloch and others:

$$-\frac{dE}{dx} = \frac{2\pi N_A Z}{A}\frac{mc^2\rho z^2 r_e^2}{\beta^2} \cdot \left[\ln\left(\frac{2m\gamma^2 v^2 W_{\max}}{I^2}\right) - 2\beta^2 - \delta(\beta\gamma) - 2\frac{C}{Z}\right] \tag{1.2}$$

where $r_e = \frac{e^2}{mc^2}$ is the classical electron radius, I is the mean ionizing potential of the target, $W_{\max}$ is the maximum energy transfer in a single collision, $\delta(\beta\gamma)$ is the density correction and C is the shell correction.

The mean ionizing potential I is one of the most important terms of the Bethe-Bloch formula, and it is usually computed experimentally for each determined medium. It can be defined as:

$$I = \hbar\langle\omega\rangle \tag{1.3}$$

with $\hbar$ and $\langle\omega\rangle$ as defined from Bohr's formula in equation 1.1. The maximum energy transfer is produced by a head-on collision and, for an incident particle of mass M colliding with an electron of mass m, the kinematics gives:

$$W_{\max} = \frac{2mc^2\eta^2}{1 + 2s\sqrt{1+\eta^2} + s^2} \tag{1.4}$$

where $\eta = \beta\gamma$ and $s = m/M$. If $M \gg m$ then

$$W_{\max} \simeq 2mc^2\eta^2\ . \tag{1.5}$$

The corrections δ and C intervene at high and low energy respectively. Considering the density correction, the incident particle has an electric field that tends to polarize the atoms along its path inside the target. The effect is an intense

full electric field that shields the electrons far from the particle trajectory. All the collisions with the outer electrons will contribute less to the total energy loss than as predicted by the equation 1.2. The shell correction, instead, arises when the velocity of the particle is comparable or even smaller than the orbital velocity of the atomic electrons. In these scenario, the hypothesis that the electron is stationary with respect to the incident particle no longer exists and the equation 1.2 is not valid anymore. Figure 1.2 shows a comparison of the total energy loss with and without the density correction and the loss from transfers of less than 10 keV for a typical medium. As can be observed, for large values of the Lorentz factor γ, the density correction limits the logarithmic growth of the energy loss.

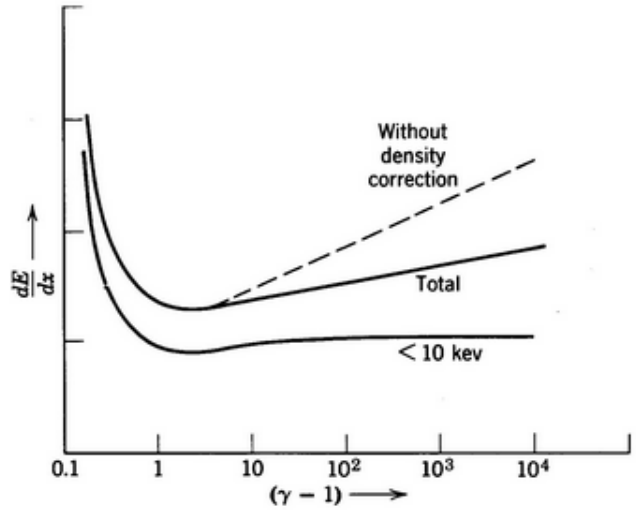

Figure 1.2. Total energy loss and loss from individual energy transfers of less than 10 keV, including the density effect (solid lines). The total energy loss without density correction is also shown (dotted line) (*Jackson* [1]).

Stopping power energy dependence

The dependence of the stopping power as a function of the kinetic energy for different particles is shown in Figure 1.3.
For a non relativistic particle, dE/dx is dominated by the overall factor $1/\beta^2$ and decreases with increasing velocity until a minimum is reached at $v \sim 0.96c$. At this point, particles are usually referred to as Minimum Ionizing Particles (MIP). As the energy increases beyond the MIP point, the term $1/\beta^2$ becomes almost constant and dE/dx rises again due to the logarithmic contribution in equation 1.2. Anyway, the relativistic rise is compensated by the density correction, as previously shown in Figure 1.2. When different charged projectiles with the same velocity are compared, z is the only factor that change outside the logarithmic term in equation 1.2. Therefore, particles with greater charge will have a larger specific energy loss. The study of dE/dx for different materials as absorbers has also shown the energy loss dependence on the electron density of the medium: the higher density materials, the higher energy loss.

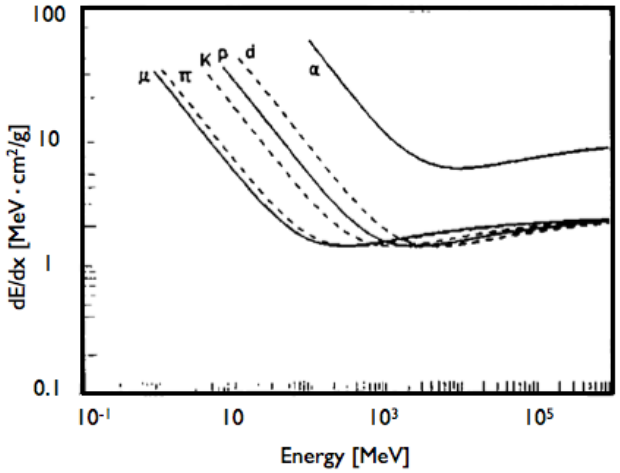

Figure 1.3. The stopping power as a function of the kinetic energy for different particles (*Leo* [3]).

Taking into account all the aforementioned considerations, a heavy charged particle deposits more energy per unit path length at the end of its path inside the target, rather than at its beginning, as shown in Figure 1.4. The amount of ionization created by a heavy charged particle as a function of its penetration depth inside the target is known as the *Bragg curve*. This behaviour can be explained observing that since the particle spends a longer time in the proximity of any given electron when its velocity is low, the impulse felt by the electron, and so the energy transferred, is larger. At the very end of the Bragg curve, the incoming particle begins to pick up electrons, lowering the effective charge of the projectile and thus the dE/dx drops.

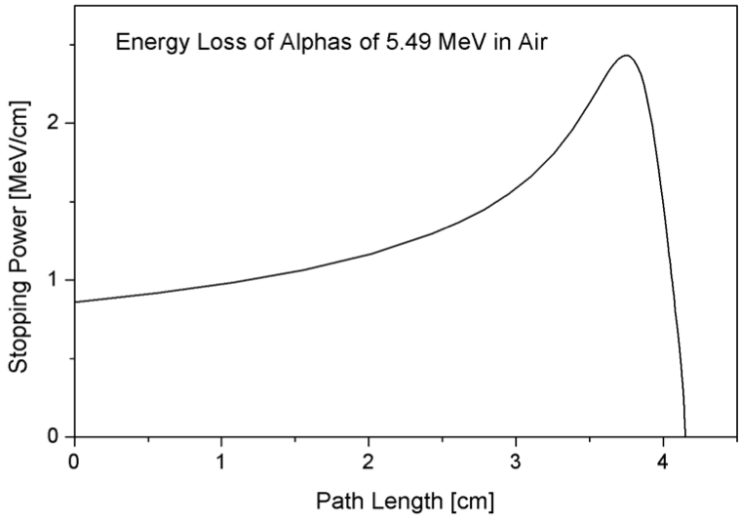

Figure 1.4. A typical Bragg curve shows the stopping power of air for 5.49 MeV α particles produced from the ^{241}Am radioactive decay.

1.1.2 Range

The *range* of a particle is its penetration depth through a traversed medium until the particle loses all its energy. The range of a particle depends on the type of the particle, on its initial energy and on the material traversed. From an experimental point of view, the range can be measured using a collimated beam of fixed energy particles impinging on a material of different thickness (t) and measuring the ratio of transmitted to incident particles (I and I_0 respectively). Figure 1.5 shows a typical plot of the ratio I/I_0 in function of the absorber thickness t. As it can be observed for

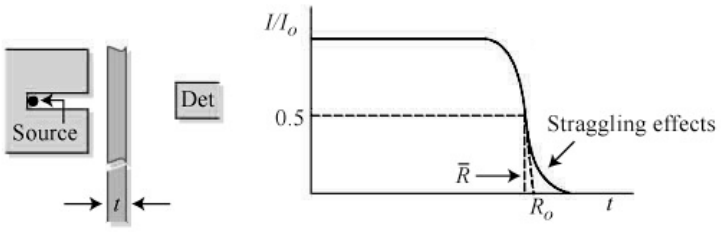

Figure 1.5. A typical *range number-distance* curve for an alpha particle collimated source.

small thicknesses almost all the particles survive ($I = I_0$). As the material thickness approaches the range value, the I/I_0 ratio does not drop immediately to zero, but it slopes down with a non zero spread of thicknesses. This behaviour is named *range straggling* and can be justified by the statistical nature of the energy loss mechanism. Therefore, two identical particles with the same initial energy traveling in the same material will not undergo the same number of collisions and hence the same energy loss. In a first approximation, the range straggling measured for a set of identical particles has a gaussian shape, where the gaussian mean value is called the *mean range* $\bar{R}$, corresponding to the point in the middle of the descending slope, as can be seen in Figure 1.5. Thence, for a thickness $t = \bar{R}$ almost half of the incident particles are absorbed, but the interesting thickness value, where all the particles are absorbed, can be extrapolated by taking the tangent to the *range number-distance* curve at the $\bar{R}$ point and its t axis intercept (R_0). This parameter is usually known as the *extrapolated range*.

1.1.3 Nuclear fragmentation

The nuclear fragmentation is a nuclear physics process that occurs after the nuclei interactions. It has to be taken into account when heavy charged particles accelerated to energies up to hundreds of MeV are involved.
The nuclear collisions of the particle projectile with the target nuclei can be distinguished in central (or near central) and peripheral collisions depending on the size of the impact parameter with respect to the size of the interacting particles. Central collisions occur for small values of the impact parameter, with the subsequent complete fusion of the projectile and target nucleus. On the other hand, the peripheral collisions occur with increasing size of the impact parameter, where the overlapping region between the projectile and the target nucleus is small inducing their incomplete fusion (see Fig. 1.6).

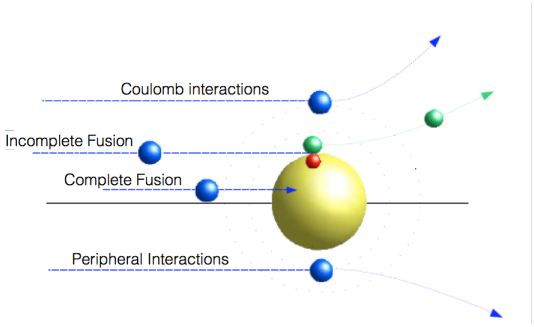

Figure 1.6. Semi-classical representation of the nuclear reaction mechanisms.

The Complete Fusion (CF) and Incomplete Fusion (IF) cross sections change as a function of the projectile energy. At high energies the CF probability is very low while the IF probability is very high. Instead at low energies, in the Bragg peak region, the CF probability reaches values of $\sim 40 - 50\%$ or even more, depending also on the projectile mass.

According to *Serber* [4], inelastic nuclear reactions at relativistic energies occur in two different steps, defining two different time scales. The first interaction transfers a certain amount of excitation energy to a target nucleus, in a characteristic time of 10^{-23} s, and the composition of the reaction partners can be modified. This step is called as the *abrasion* process. In the second step, called *ablation*, the nucleus de-excitation takes place by evaporation of neutrons, protons and light nuclei, fission and gamma rays emission. The characteristic time for particles emission varies in a range between 10^{-21} s to 10^{-16} s for an excitation energy of 200 MeV and 10 MeV, respectively.

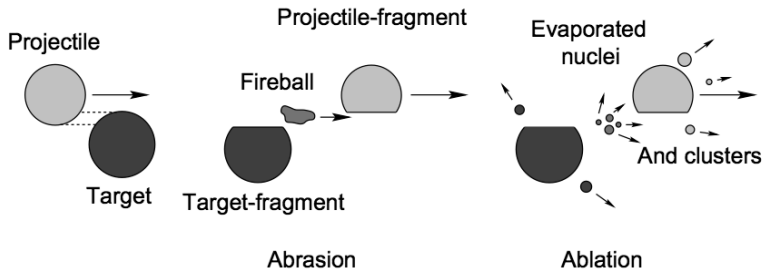

Figure 1.7. Scheme of the abrasion and ablation nuclear processes occurring in the peripheral collision between a particle projectile (light grey) and a target nucleus (dark grey), producing secondary neutral and charged fragments.

Bowman, Swiatecki and Tsang [5] introduced the abrasion-ablation model, schematically shown in Figure 1.7. In the overlapping zone between the particle projectile and target nucleus, nucleons are abraded and the hot reaction zone (fireball) is created, while the outer nucleons (spectators) are only slightly affected by the collision. The fireball is a composite nucleus and the energy initially concen-

trated on a few nucleons spreads through the composite nucleus in order to reach the equipartition of the excitation energy, *i.e.* the state of statistical equilibrium. In this phase called *thermalization* particles can be emitted into the continuum with energies higher than if they would be emitted by a *fully*-equilibrated nucleus. Such continuous emission is called the *pre-equilibrium* emission.
When the statistical equilibrium is achieved, the fragments emission stops and if the composite nucleus is not in the fundamental state, as well as the particle and target fragments, the ablation process occur: the fireball and the fragments undergo by de-excitation by evaporating nucleons, light clusters and gammas (prompt gamma emission). The secondary products emitted by the projectile fragments are forward peaked in the laboratory frame, due to the high velocity of the projectile, having almost the same velocity of the primary particle. On the other hand, neutrons and clusters produced by the target fragments are emitted isotropically and with much lower velocities. The particles ablated from the fireball cover the range between the projectile and target emission.

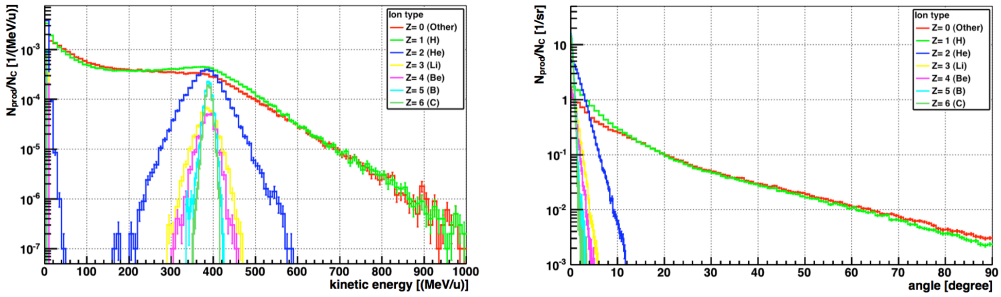

Figure 1.8. FLUKA simulation of kinetic energy (left) and angular (right) distributions of the yield ($N_{\mathrm{prod}}/N_{\mathrm{C}}$) of secondary fragments produced in the interaction of a 400 MeV/u ^{12}C ion beam impinging on a carbon target 5 mm thick. The angular distribution is reported for fragments with kinetic energy $T > 30.0$ MeV/u (*Pleskac et al.* [6]).

Figure 1.8 shows a simulation with the Monte Carlo FLUKA code (*Ferrari et al.* [7]) of the kinetic energy (left) and angular (right) distributions of the yield of secondary fragments (N_{prod}) produced in the interaction between 400 MeV/u ^{12}C ions (N_{C}) impinging on a carbon target 5 mm thick (*Pleskac et al.* [6]). The fragments kinetic energy per nucleon is peaked at the primary carbon energy and the angular distribution shows that $Z \geq 2$ fragments are emitted within 12°, while neutrons and hydrogen ions cover a wider angular range.

1.2 Electrons and positrons

Like heavy charged particles, electrons and positrons also suffer a collisional energy loss when passing through matter, but their small mass change some assumptions on the interaction's behaviour between the incident particle and the material. A large deflection from the primary electron (or positron) direction has to be taken into account and an additional energy loss mechanism comes into play, the *bremsstrahlung*. In this section, the main processes occurring in the electron and positron interactions with matter will be described.

1.2.1 Collisional and radiative energy loss

With respect to heavy charged particles, electrons and positrons Bethe-Bloch formula must be slightly modified. Electrons and positrons mass is equal to that of the orbital electrons with which they interact, causing large deviations in the electron path, while for incident heavy charged particle the assumption that it remains undeflected during the collision was made.
Since for electrons the collisions are between identical particles, a much larger fraction of energy can be lost in a single impact. Equation 1.2 has to be modified, starting from the maximum energy transfer that is $W_{\max} = T_{\mathrm{e}}/2$, where T_{e} is the kinetic energy of the incident electron (or positron). Furthermore, because of their small mass, an additional energy loss mechanism occurs: the emission of electromagnetic radiation arising from scattering in the electric field of a nucleus (bremsstrahlung). From classical theory, any charge must radiate energy when accelerated, causing both energy loss and angular deflection of the interacting electron (positron).
The total energy loss of positrons and electrons can be expressed by the sum of two terms:

$$-\left(\frac{dE}{dx}\right)_{tot} = -\left(\frac{dE}{dx}\right)_{rad} - \left(\frac{dE}{dx}\right)_{coll} \ . \tag{1.6}$$

The linear specific energy loss through the radiative process is given by:

$$-\left(\frac{dE}{dx}\right)_{rad} = 4\alpha N_A \frac{Z(Z+1)}{A} r_e^2 E \ln\frac{287}{Z^{1/2}} \tag{1.7}$$

where $\alpha = \frac{e^2}{\hbar c}$ is the fine structure constant and the other quantities are defined as in equation 1.1. This radiation component exists also for heavy charged particles, but it is generally negligible for the energies of interest of this thesis.
Radiative losses depend strongly on the absorbing material and they increase significantly in materials with high atomic number. It is possible to define for each material a critical energy E_c at which the radiation loss is equal to the collision loss:

$$\left(\frac{dE}{dx}\right)_{rad} = \left(\frac{dE}{dx}\right)_{coll} \qquad \text{for} \quad E = E_c \ . \tag{1.8}$$

Above the critical energy, the radiation component will dominate over the collision component and vice-versa. Bethe and Heitler evaluated an approximated formula to estimate E_c:

$$E_c \simeq \frac{1600 mc^2}{Z} \ . \tag{1.9}$$

Table 1.9 shows a short list of critical energies for several materials commonly used in experimental physics applications. As the energy is increased, the probability of bremsstrahlung rapidly rises, so that at a few tens of MeV radiation loss is comparable to or even greater than the collision loss.

The electrons of interest in this thesis have typical energies lower than 10 MeV.

Material	Critical energy [MeV]
Pb	9.51
Al	51.0
Fe	27.4
Cu	24.8
Air (STP)	102
Lucite	100
Polystyrene	109
NaI	17.4
Anthracene	105
H_2O	92

Figure 1.9. Critical energy values of some materials.

1.2.2 Multiple Coulomb scattering

When charged particles cross matter, together with inelastic collisions with atomic electrons, also repeated elastic Coulomb scatterings from target nuclei occur. In a first approximation, the cross section of these collisions can be described by the Rutherford formula:

$$\frac{d\sigma}{d\cos\theta} = Z^2 r_e^2 \frac{(mc/\beta p)^2}{4\sin^4(\theta/2)} \tag{1.10}$$

where θ is the deflection angle from the particle trajectory. Assuming that the target nuclei mass is much greater than the incident particle mass, so that the energy transfer to the nucleus is negligible, the majority of such elastic scattering result in a small angular deflection, due to the $(sin^4(\theta/2))^{-1}$ cross section dependence.
There are three different types of Coulomb scattering that can take place:

- Single Scattering: when the absorber is very thin such that the probability of more than only one Coulomb scattering is very small. The angular distribution is then given by the Rutherford equation 1.10.
- Plural Scattering: when the average scattering number is $N < 20$. This is the most difficult case to treat since neither the Rutherford formula nor statistical methods can be applied.
- Multiple Scattering: when the average number of collisions is $N > 20$ and the energy loss is small or negligible. The problem can be treated statistically to obtain the probability distribution for the net deflection angle as a function of the material traversed thickness.

The multiple scattering (MS) is the most frequently case found in common applications. Rigorous calculations of multiple scattering are extremely complicated but the mainly used ones are the small angle approximations by Molière and by

Snyder and Scott. Their formulations have been demonstrated to be generally valid for almost all particles up to angles of $\theta \simeq 30°$. Ignoring the small probability of large-angle single scattering, the effect of multiple scattering in a given material can be obtained by considering the distribution resulting from the small angle ($\theta < 10°$) single scattering only. Then the probability distribution is approximately Gaussian and can be written as follows:

$$P(\theta)d\Omega \simeq \frac{2\theta}{\langle\theta^2\rangle} exp\left(\frac{-\theta^2}{\langle\theta^2\rangle}\right) d\theta \ . \tag{1.11}$$

The parameter $\langle\theta^2\rangle$ represents the variance of the scattering angle distribution, obtained by the integral:

$$\int \theta^2 P(\theta)\, d\Omega \ . \tag{1.12}$$

The square root $\sqrt{\langle\theta^2\rangle}$ is known as the RMS scattering angle. However, a better estimation is obtained by using an empirical formula proposed by *Highland* [8] which is valid to within 5% for target atomic number $Z > 20$ and for target thickness $10^{-3}L_{rad} < x < 10L_{rad}$. An empirical estimation of the Gaussian sigma is:

$$\sigma_\theta[rad] = \frac{14.1[\text{MeV}]}{p\beta c} Z\sqrt{\frac{x}{L_{rad}}}\left(1 + \frac{1}{9}\log_{10}\frac{x}{L_{rad}}\right) \tag{1.13}$$

with L_{rad} the material's radiation length, x the material's thickness and p the particle's momentum. Therefore, the multiple scattering effect is enhanced for high Z targets and it increases as the particle energy decreases, due to the $(1/p\beta c)$ term. On the other hand, thin absorbers (low x values) reduce the angular spread of the trajectory of the incident particle.

1.2.3 Backscattering of low energy electrons

Because of the small mass, electrons suffer from large deflection angles by scattering from target nuclei. An electron entering an absorber surface can undergo to such great deflection that it is *backscattered* out of the absorber, as illustrated in Figure 1.10.

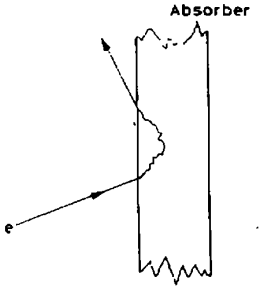

Figure 1.10. Illustration of a backscattering process of an electron.

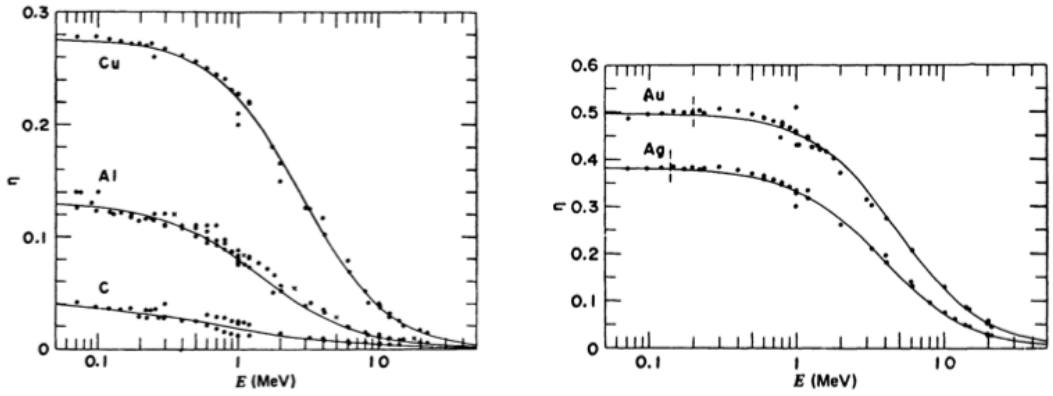

Figure 1.11. Fraction η of normally incident electrons that are backscattered from a thin slab of various materials, as a function of the incident energy E (*Tabata et al.* [9]).

The probability of this phenomenon is higher for electrons with energy less than 10 MeV and absorbers with high atomic number.

The backscattering process has a significant effect on the response of detectors designed to measure the low energy of incident electrons, since backscattered electrons do not deposit all their energy in the absorbing medium. As an example, for non-collimated electrons impinging on a high Z material such as NaI, as much as 80% may be scattered back. The measured ratio (η) of backscattered electrons to incident electrons as a function of the electrons incident energy E is shown in Figure 1.11. The primary electrons are mono energetic and perpendicularly incident on the surface of various materials.

1.3 Photons

At the energy of interest of this work (100 keV − 10 MeV) photons interact with matter via three principal mechanisms: photoelectric absorption, Compton scattering and pair production. All these processes lead to the partial or complete photon energy transfer to atomic electrons. In this section such processes will be described.

1.3.1 Photoelectric absorption

In the photoelectric effect a photon is absorbed and gives all of its energy to an atomic electron. In the interaction the atom can be ionized ejecting the electron, usually referred to as *photoelectron*, from one of the atom's bound shells. This interaction cannot take place with free electrons, since a free electron cannot absorb a photon and also conserve momentum. For bounded electrons the nucleus absorbs the recoil momentum instead. Thus, the photoelectron energy is:

$$E = h\nu - B.E. \tag{1.14}$$

with B.E. the electron binding energy. The photoelectric effect is therefore observed only for photon energies greater than the binding energy of the atomic electrons. The applications of this process include virtually all dental and medical diagnostic

X-rays, airport baggage inspection X-rays, and X-rays emitted during relaxation of the atomic electrons following radioactive nuclear decay.

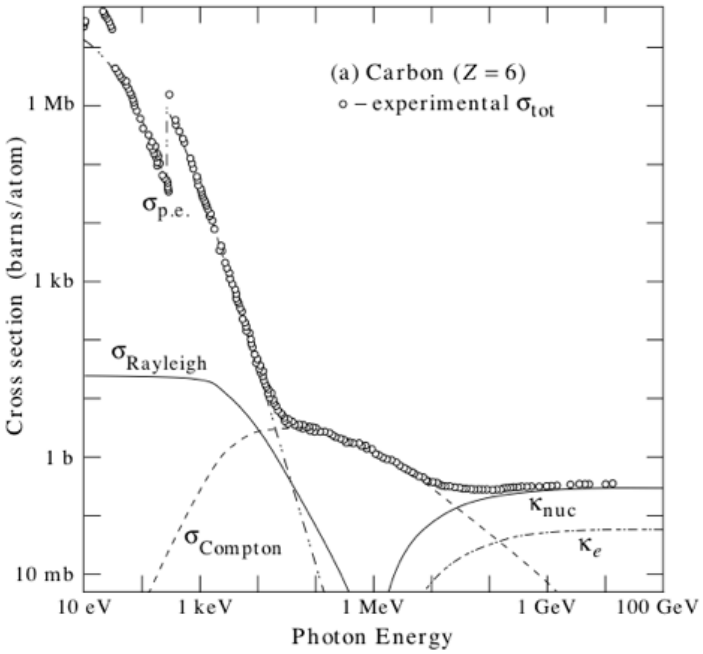

Figure 1.12. Photons total cross section σ_{tot} as a function of the photon energy in carbon, with the contribution of: $\sigma_{\text{p.e.}}$ = photoelectric effect, σ_{Rayleigh} = Rayleigh (coherent) scattering, σ_{Compton} = incoherent scattering, κ_{nuc} = pair production in nuclear field, κ_e = pair production in electron field.

Figure 1.12 shows the photon total cross section σ_{tot} and all the contributions of different processes as a function of the photon energy for a carbon target. The K-shell electrons are the most tightly bounded, and are the most important contribution to the atomic photoelectric cross section. However, if the photon energy drops below the binding energy of a given shell, an electron from that shell cannot be ejected. For photon energies greater that the highest atomic binding energy, the photon cross section dependence on the medium atomic number Z is given by:

$$\sigma_{\text{p.e.}} = constant \cdot Z^n/(h\nu)^3 \tag{1.15}$$

where n is a number which varies between 4 and 5.
In high Z materials the photoelectric effect is enhanced and, therefore, high Z materials are often used to build photon detectors, as it will be discussed in next chapters.

1.3.2 Compton scattering

In Figure 1.13 (*Klein and Nishina* [10]) is shown the Compton scattering process: a photon collides with an electron, called *recoil electron*, loses some of its energy and then it is deflected from its original direction.

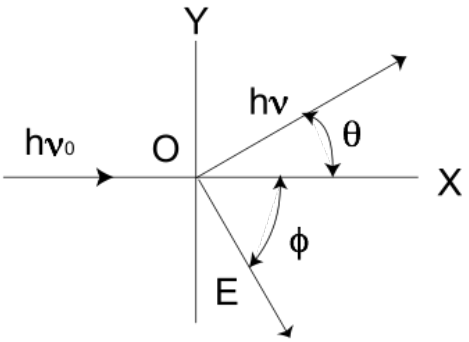

Figure 1.13. Scheme of the Compton scattering of an incoming photon with energy $h\nu_0$ with a free electron at rest in the origin of the reference coordinate system. $h\nu$ is the energy of the scattered photon while E is the energy of the scattered electron.

If the photon energy is much higher with respect to the electron binding energy, the electron can be considered as basically free. The relation between the photon deflection angle θ and the energy loss in the Compton scattering arises from the momentum and energy conservation laws in the interaction between the photon and the recoiling electron. The kinematics of the photon and of the scattered electron can be described by the following equations:

$$h\nu = \frac{h\nu_0}{1 + \left(\frac{h\nu_0}{m_e c^2}\right)(1 - \cos\theta)}, \tag{1.16}$$

$$E = h\nu_0 - h\nu = m_e c^2 \frac{2(h\nu_0)^2 \cos^2\phi}{(h\nu_0 + m_e c^2)^2 - (h\nu_0)^2 \cos^2\phi}, \tag{1.17}$$

$$\tan\phi = \frac{1}{1 + \left(\frac{h\nu_0}{m_e c^2}\right)} \cot\frac{\theta}{2} \tag{1.18}$$

where $h\nu_0$ and $h\nu$ are the initial and final energy of the photon and θ is the photon scattering angle. E is the recoil energy of the electron, scattered with an angle ϕ, m_e is the rest mass of the electron and c is the speed of light.
The probability of the occurrence of Compton scattering per atom of the absorber depends on the number of electrons available and therefore increases linearly with the atomic number Z of the target material. The contribution of the Compton scattering cross section σ_{Compton} to the total photon cross section as a function of the photon energy is shown in Figure 1.12 for a carbon target.
σ_{Compton} decreases with increasing photon energy. The Compton scattering cross section is known as the *Klein-Nishina* formula and is given by:

$$\frac{d\sigma_{\text{C}}}{d\Omega} = \frac{1}{2} \frac{r_0^2(1 + \cos^2\theta)}{[1 + \varepsilon(1 - \cos\theta)]^2} \cdot \left\{1 + \frac{\varepsilon^2(1 - \cos\theta)^2}{(1 + \cos^2\theta)[1 + \varepsilon(1 - \cos\theta)]}\right\} \tag{1.19}$$

with $r_0 = \frac{e^2}{m_e c^2}$ the classical electron radius and $\varepsilon = \frac{h\nu_0}{m_e c^2}$. Figure 1.14 shows the scattered photon angular distribution. An enhancement of the forward scattering at high photon energy values is clearly shown.

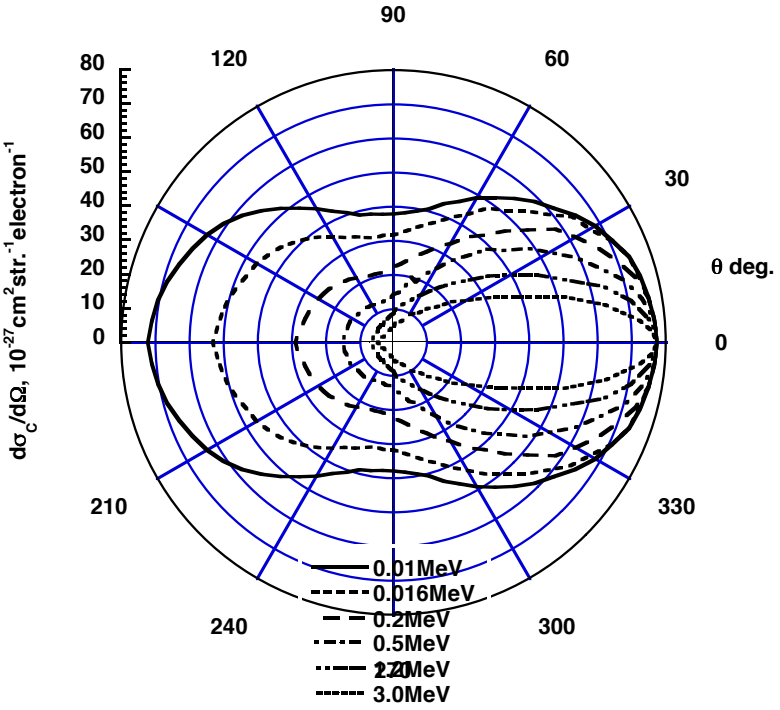

Figure 1.14. Polar plot of the differential cross section of Compton scattering for different initial photon energy values.

1.3.3 Pair production

The most frequent photon interaction at energies larger than twice the electron mass is the pair production, where the incident photon disappears and an electron-positron pair is created. From the energy and momentum conservation laws, the pair production occurring in the field of a nucleus of mass M ($M \gg m_e$) has an energy threshold of $T_{thr} = 2m_e c^2 = 1.022$ MeV.

All the photon energy exceeding the pair production energy threshold goes into kinetic energy shared by the electron and the positron. The positron will subsequently slow down in the absorber and annihilate with another electron of the medium, producing two annihilation photons.

The pair production cross section rises with energy, as shown in Figure 1.12. The main contributions to the pair production cross section are due to the photon interactions with nuclei ($\kappa_{\rm nuc}$) and electrons (κ_e) and it varies with the absorber atomic number as:

$$\kappa_{\rm nuc} \sim Z^2 \quad , \quad \kappa_e \sim Z \ . \tag{1.20}$$

κ_e is of minor importance, except for low-Z materials.

Finally, the angle in between the initial direction of the incoming photon and the

direction of the produced electron (or positron) is:

$$\theta \sim \frac{m_e c^2}{h\nu} \ . \tag{1.21}$$

1.3.4 Attenuation coefficient

The total interaction probability for a photon can be expressed as the sum over contributions of the principal cross sections aforementioned. Following the notation introduced in Figure 1.12, the total cross section σ_{tot} is:

$$\sigma_{\text{tot}} = \sigma_{\text{p.e.}} + \sigma_{\text{Compton}} + \kappa_{\text{nucl}} + \kappa_e \ . \tag{1.22}$$

The *total absorption coefficient* (μ) is given by the probability per unit length for an interaction to occur and it can be obtained multiplying σ_{tot} by the atom density N:

$$\mu = N\sigma_{\text{tot}} = \sigma_{\text{tot}}(N_A \rho / A) \tag{1.23}$$

where N_A is the Avogadro's number, ρ is the material density and A is the relative atomic mass of the material. The total absorption coefficient is also the inverse of the mean free path of a photon in the target. For a narrow beam of mono energetic photons with an incident intensity I_0 that penetrates a thickness x of material with a density ρ, the fraction of photons emerging with an intensity I can be expressed as:

$$I/I_0 = exp[-(\mu/\rho)x] \ . \tag{1.24}$$

In the next chapter will be introduced the particle therapy and its main physical and biological aspects. PT exploits the characteristics of the interactions of radiation with matter described in this chapter in order to treat patients affected by cancer.

Chapter 2

Particle Therapy

Radiation therapy is one of the essential instruments for cancer treatment, and nowadays it is used to treat localized malignant tumors, alone or combined with chemotherapy or surgery.
Ionizing radiations are a powerful tool for human cells killing, since a high dose of radiations can control the tumor growth and efficiently destroy the tumor. Nevertheless, the presence of healthy cells surrounding the tumor volume limits the effective dose that can be delivered to the target: during a radiation treatment the dose release in tissues before and around the tumor area must be taken into account. Therefore, the dose delivered to the cancer cells is limited to the dose absorbed by healthy tissues.

Conventional RT uses X-rays (high energy photons or electrons) with an energy up to 25 MeV. The X-rays dose release in tissues is peaked at the beginning of their path in the patient, and it decreases with the penetration depth in tissues. An example of 21 MeV photons dose release in water is shown in Figure 2.1.
X-ray beams are produced by electron linear accelerators (*linacs*). Today there are almost $10,000$ linacs installed and operational in hospitals all over the world and radiation therapy is used every year more than about two-third of all cancer patients.

In the last decade the interest on another type of radiation therapy for tumor treatment has rapidly grown. The so called *Particle Therapy* (PT), or *hadrontherapy*[1], is based on protons or light ions as carbon ions. The use of such beams for medical applications was first proposed in the late 1946 by Robert R. Wilson.
At the Berkley laboratory, Wilson observed that the released dose profiles of charged particles as a function of their penetration in water were characterized by a small dose release at the beginning of ions path and by a maximum at the end of their range called the *Bragg peak* (see Figure 2.1). Wilson, in his paper, wrote: "The intense specific ionization of alpha particles [...] will probably make them the most desirable therapeutically when such large alpha particle energies are attained" [12]. Thus, charged particles have started to be used to treat deep sited tumors due to the high localization of their dose released that allows for a high efficiency in killing cancer cells, sparing healthy tissues and organs at risk. Following the Wilson's idea,

[1]Hadrontherapy is a common word that indicates all kind of particle therapies that use "light" particle beams such as protons, neutrons, pions and helium ions (alpha particles), carbon, oxygen ions and so forth (*Amaldi* [11]).

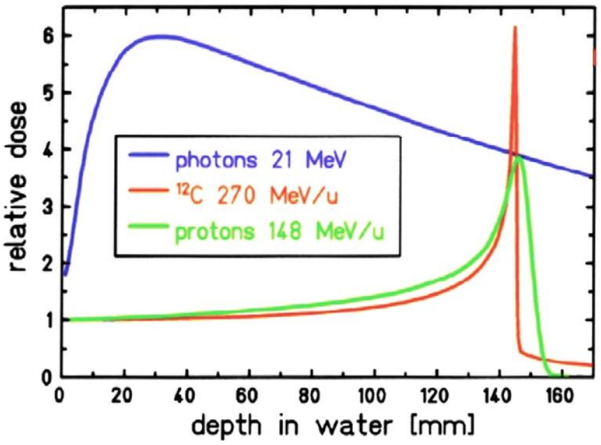

Figure 2.1. Relative dose in function of the depth in water for 21 MeV photons (blue line), 270 MeV/u ^{12}C ions (red line) and 148 MeV/u protons (green line).

the first patient was treated in 1954 with an hydrogen beam and helium and neon beams have been employed in 1957 and 1975, respectively. In those years about 1,000 of patients affected by tumors experienced the radiation therapy with protons. In Europe, at the Uppsala cyclotron in 1957, B. Larsson treated the first cancer case with protons, while in 1970s, at the LBL, the hadrontherapy with ions heavier than protons began to be tested, from Cornelius A. Tobias' suggestions (*Tobias et al.* [13]).

Concerning the present situation, in October 2014 the Particle Therapy Co-Operative Group (PTCOG), an international institution that monitors the hadrontherapy facilities all around the world, published that 95,429 patients have been treated with protons and more than 10,000 with carbon ions, as shown in Table 2.1.

In Europe, the development of proton therapy in cancer treatment first occurred in Villigen (Switzerland), at the Paul Scherrer Institute (PSI) (*Pedroni et al.* [14]), while carbon ion therapy first took place in Darmstadt (Germany), at the GSI Helmholtz Centre for Heavy Ion Research (*Haberer et al.* [15]). Then in Heidelberg (Germany) the Heidelberg Ion Therapy center (HIT) (*Haberer et al.* [16]) was built. CATANA [17] has been the first hadrontherapy center in Italy, at Laboratori Nazionali del Sud of the National Institute of Nuclear Physics (LNS - INFN) in Catania, and it deals with choroidal and iris melanomas. CATANA treated its first patient in 2002 and since then, other 349 patients have been irradiated with protons [18]. The other operational center in Italy is the Centro Nazionale di Adroterapia Oncologica (CNAO) in Pavia [19], that treated its first patient with protons in 2011 and the year after it started to use also carbon ion beams. Together with the HIT center in Heidelberg, CNAO is the only facility in Europe that allows both for proton and carbon ion therapy. In 2014 the proton facility ATreP in Trento (Italy) also became operational and the first patient has been treated in October 2014.

In this chapter the physical and biological aspects of particle therapy will be described. The main techniques of beam delivery will be introduced and a short review of the status and prospects of particle therapy will be presented.

Country	Facilities in operation		Facilities planned (or under construction)		Patients treated (operative facilities)	
	Protons	Light ions	Protons	Light ions	Protons	Light ions
USA	16	0	15	0	44458	
Europe	13	2	15	1	27479	1473
Japan	9	4	3	1	13859	11055
Russia	3	0	2	0	6701	
China	1	2	2	1	1078	249
South Korea	1	0	1	1	1158	
South Africa	1	0	0	0	521	
Canada	1	0	0	0	175	
Taiwan	0	0	2	0		
Saudi Arabia	0	0	1	0		
India			1			

Table 2.1. Geographical distribution of particle therapy facilities until October 2014. Data from Particle Therapy Co-Operative Group 2014 survey [18].

2.1 Physical aspects

In this section, the fundamental physic quantities that characterize the particle therapy are outlined.

2.1.1 Absorbed Dose

Radiobiological and clinical effects in radiation therapy are correlated to the absorbed dose, a physical quantity defined in equation 2.1 as the mean energy deposited by ionizing radiation (E) per unit mass (m) (*ICRU report* [20]):

$$D = \frac{dE}{dm} \, . \tag{2.1}$$

In the international system of unit (SI) the dose unit of measurement is the *gray* and 1 Gy corresponds to 1 J of absorbed radiation by 1 kg of mass (1 Gy = 1 J/kg). The released dose in a thin slice of absorber material with mass density ρ for a parallel particle beam with fluence F (dN particles traversing a surface dS) can be calculated as:

$$D[\mathrm{Gy}] = 1.6 \times 10^{-9} \times \frac{dE}{dx}\left[\frac{\mathrm{keV}}{\mu\mathrm{m}}\right] \times F[\mathrm{cm}^{-2}] \times \frac{1}{\rho}\left[\frac{\mathrm{cm}^3}{\mathrm{g}}\right] \tag{2.2}$$

where dE/dx is the stopping power, defined in the previous chapter (see Section 1.1.1).

2.1.2 Linear Energy Transfer

The Linear Energy Transfer (LET) refers to the transferred energy from a ionizing radiation to a medium. It describes how much energy a ionizing particle transfers to the traversed matter per unit distance and it is equal to the breaking force acting on a charged ionizing particle traveling inside a material. The LET is then related only to the energy loss of the charged particle due to electronic collisions. The unit of measurement for the LET is the keV/µm. The LET is directly coupled to the DNA damages, but it limits the radiation range in matter. Therefore, the linear energy transfer is closely related to the stopping power.

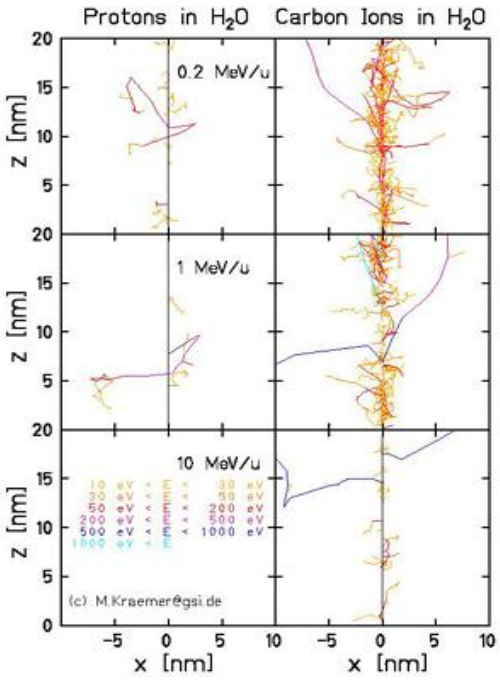

Figure 2.2. Comparison between proton and carbon tracks at different energies. Protons energy loss is small and single following events occur distant from each other, implying the DNA lesions repair. For carbon ions the ionization density increases with decreasing energy, *i.e.* at the end of the particle path in tissues, producing multiple localized damages to the DNA molecule (*Fokas et al.* [21]).

When a charged particle crosses a medium, secondary electrons are produced by ionization processes. If their energy is large enough to allow further medium ionizations, secondary electrons are called *delta rays*. It can be of interest to focus on the energy transferred in the proximity of the primary particle track, excluding the interactions that produce delta rays with energies larger than a determined value Δ. In this approach secondary electrons that carry energy far from the primary particle track are not taken into account, since larger energy implies larger range (see

Section 1.1.2). The directional distribution of secondary radiation and the non-linear path of delta rays are then neglected. The result of this approach is the *restricted* linear energy transfer:

$$L_\Delta = \frac{dE_\Delta}{dx} \tag{2.3}$$

where dE_Δ is the energy loss of the charged particle due to the electronic collisions when traversing a distance dx, without taking into account all secondary electrons with kinetic energies larger than Δ.

In the $\Delta \to \infty$ limit the linear energy transfer becomes the *unrestricted* LET which is equal to the linear electronic stopping power (see equation 1.2).
Photons and protons have a sparse ionization density and so are called *low-LET* radiation, while carbon ions are *high-LET* particles due to their larger ionization density as shown in Figure 2.2. On the other hand, it has to be considered that protons can reach high LET values at the end of their range in tissues (in proximity of the BP). Details on the DNA damages due to ionization processes are given in Section 2.2 concerning particle therapy biological effects.

2.1.3 Energy deposition

While photons energy released decreases exponentially with the penetration depth (see Figure 2.1), showing a maximum between $1 \div 3$ cm for photon energies of interest in radiotherapy, charged particles lose their energy per unit length following the Bethe-Bloch formula defined in Section 1.1.1. Equation 1.2 shows that in the entry channel of the particle in the target, *i.e.* for high velocity, the energy loss is small, while it maximizes at the end of the particle range, when the particle is about to stop in the target. The particle range inside the target, described in Section 1.1.2, strongly depends on the beam initial energy, so the BP position can be shifted changing the beam energy, as shown in Figure 2.3.

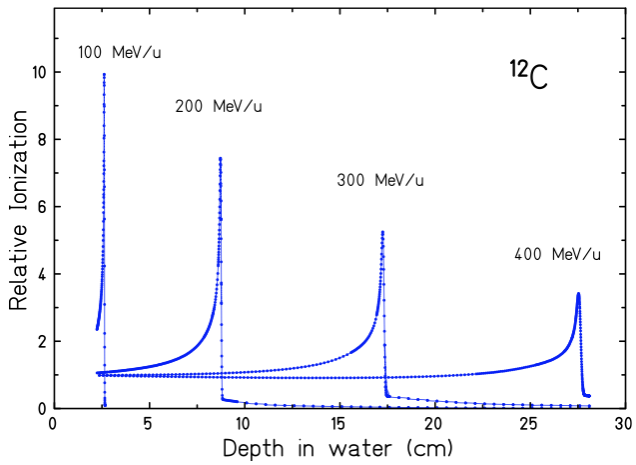

Figure 2.3. Carbon ions measured depth-dose distributions in water for different beam energies (*Schardt et al.* [22]).

In Figure 2.4 is reported a simplified scheme of the dose release in radiotherapy: in (a) is presented the ideal dose-depth relation where only the tumor (pink box) is irradiated while in (b) the photon dose-depth relation in shown; in (c) and (d) the dose-depth profile is shown for protons and carbon ions, respectively. From this simple sketch it can be easily understood how in PT treatments tumors near Organs At Risk (OAR, yellow volume) could be treated with a reduced damage to the surrounding healthy tissues with respect to radiation therapy with photon (b). It has to be pointed out that the nuclear fragmentation of charged particles interacting with target nuclei has to be considered for carbon beams (see Section 1.1.3): the produced projectile fragments, due to the conservation of the projectile momentum, are responsible of an overdosage that is delivered to tissues beyond the tumor volume, due to a tail of the released dose after the BP (Figure 2.4 (d)). Such overdosage is not present for protons (Figure 2.4 (c)).

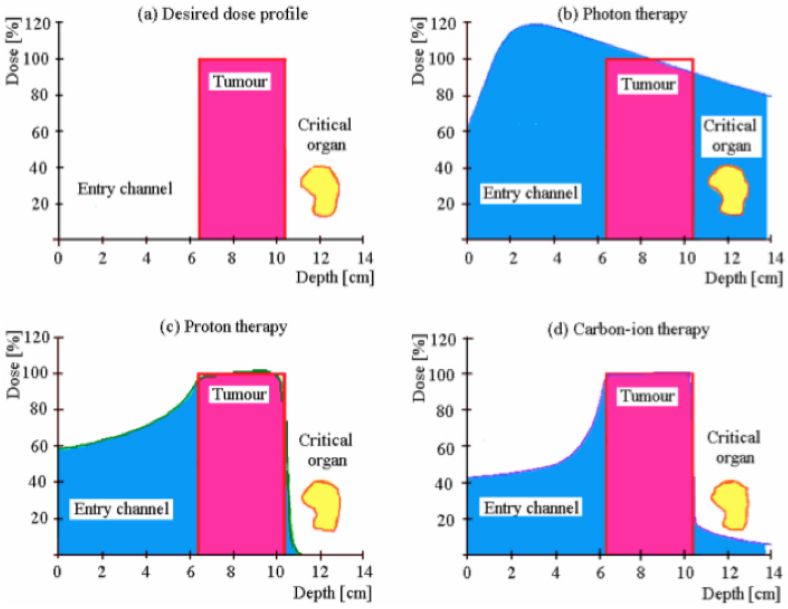

Figure 2.4. Comparison between desired dose profile (a), photon therapy with a single field (b), proton therapy (c) and carbon ion therapy (d) for a given tumor volume (pink box) in proximity to an OAR (yellow area). Therapies with protons or carbon ions lead to achieve a higher conformity of the dose released to the target volume and the OAR receives a much lower dose with respect to photon therapy.

2.1.4 Lateral beam spread

The charged particle beam undergoes a diffusion due to the interaction with the patient body. As a consequence the beam is spread in the transverse direction with respect to its original size. This spread is mainly caused by multiple scattering, *i.e.* elastic Coulomb interaction with target nuclei (see Section 1.2.2). If the spread is small, the angular spread distribution can be approximated by a Gaussian function, as described in equation 1.13. Considering a proton and a carbon beam having the

same range R in a material (e.g. 150 MeV protons and 285 MeV/u carbon ions with $R = 15.6$ cm), the lateral beam spread is expected to be three times larger for protons. An idea of this effect is given by Figure 2.5.

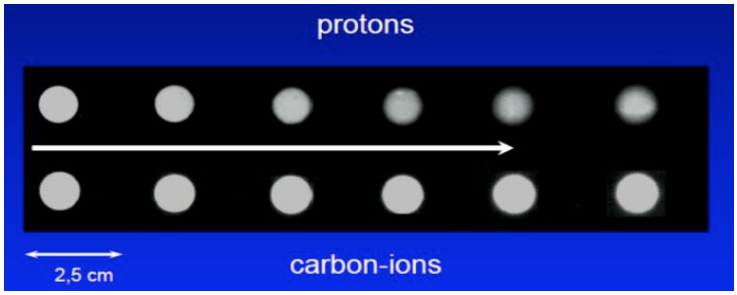

Figure 2.5. Image of the diffusion of protons (top) and carbon ions (bottom) as a function of depth in tissues.

There are two distinguishable contributions to the overall MS: the contribution due to the interaction of the beam with materials before the patient as the beam pipe exit window, the external beam monitors, collimators and air and the contribution due to the interaction with the patient tissues. The former contribution dominates at low energies, while the latter dominates at high energies, when the beam range increases inside the patient.

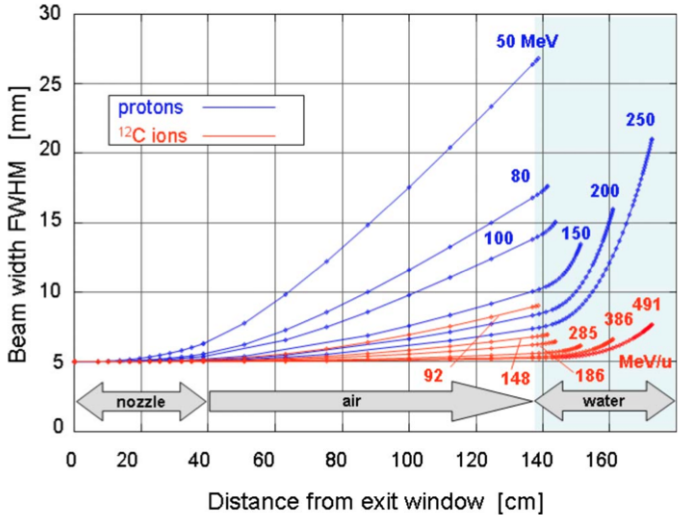

Figure 2.6. Calculated beam spread for carbon ions (red) and protons (blue) in a typical treatment beam line. A parallel particle beam of 5 mm FWHM, that passes through a nozzle (including a thin vacuum window and beam monitors) and enters a water target placed at a distance of 1 m from the nozzle exit has been simulated. At low energies the beam width is mainly dominated by the scattering in the nozzle, while at higher energies the scattering in the target dominates. Carbon ions show a much smaller spread than protons for the same penetration depth (*Schardt et al.* [23]).

For all the aforementioned reasons, materials in between the beam exit window and the patient should be minimized, especially for proton therapy. Figure 2.6 and Figure 2.7 display some examples of lateral beam spread Monte Carlo calculations for protons and carbon ions.

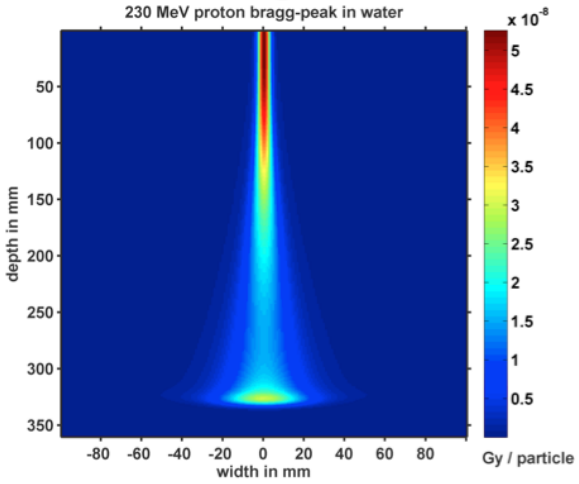

Figure 2.7. Monte Carlo simulation of a 230 MeV proton pencil beam traversing a water phantom. Picture courtesy of K. Zink.

2.2 Biological aspects

The capability of radiations (photon or charged particles) to destroy a tumor is related to the induced biological damage of cancer cells. Such damage regards the DNA strands that can be break in an indirect or direct way, bringing the cell to death. A drawing of an animal cell is shown in Figure 2.8: the cell diameter is of ~ 100 µm, while the DNA helix dimension is of 2 nm and it is contained within the cell nucleus that has a diameter of ~ 6 µm.

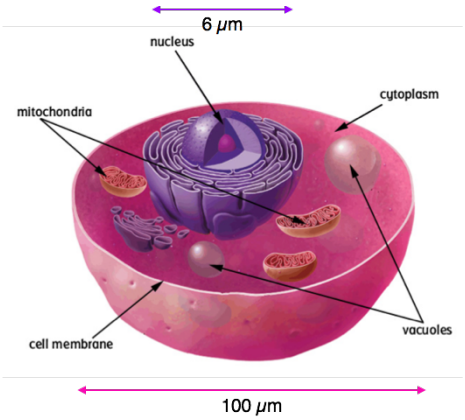

Figure 2.8. Drawing of an animal cell: the cell and nucleus dimensions are outlined.

An example of the DNA break is shown in Figure 2.9 for a photon beam: when a neutral radiation crosses the patient tissues, it ionizes the cells (healthy or cancerous). The produced electrons can themselves ionize water molecules, that compose the 80% of the human body, producing free radicals (OH, H). Such free radicals are chemically very reactive and, even if they have a very short life, they can reach the cell nucleus and damage the DNA.
On the other hand, charged particle beams induce more direct DNA breaks.

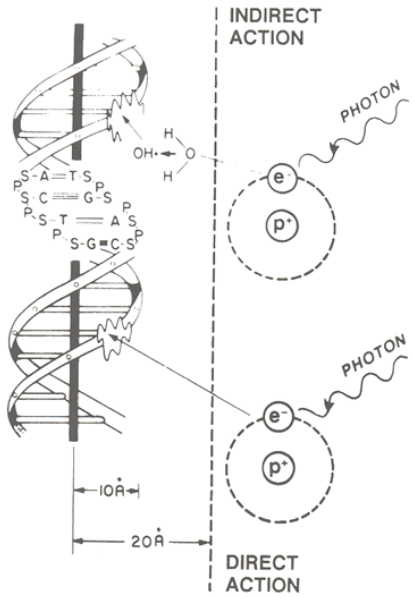

Figure 2.9. Top: DNA helix broke by the indirect action of a free radical (OH) induced by a photon radiation ionizing a tissue cell. Down: DNA helix broke by the direct action of a ionized electron by the crossing photon radiation.

The DNA lesions can be repairable or non-repairable: high-LET radiations (light ions and protons at the BP) produce more non-repairable lesions, as the DNA *double strand* breaks, than low-LET radiation (photons) (see Section 2.1.2).
The cell ability to repair the DNA lesions is an advantage for healthy cells that have also been injured by the crossing radiation, but it limits the power of radiation in killing the tumor cells.

In this section, the fundamental biological aspects and variables that characterize the particle therapy biological damage to the DNA molecule are outlined.

2.2.1 Ionization density

An example of the difference in the dose release pattern in traditional RT with respect to the corresponding pattern induced by light ions is shown in Figure 2.10 for photons (left) and ^{12}C ions (right). It is evident the concentration of the dose release around the ^{12}C tracks with respect to the uniform release induced by the photon flux.

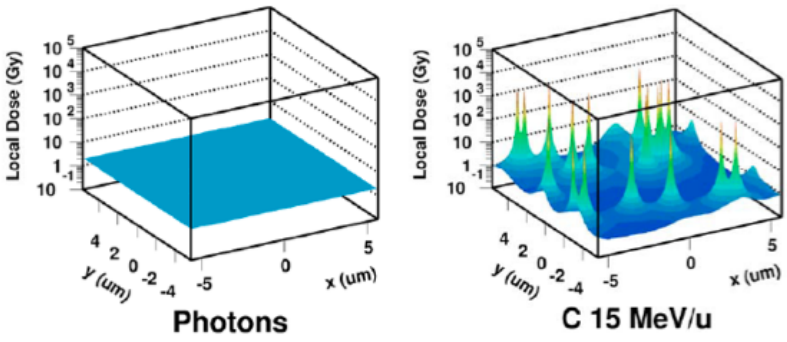

Figure 2.10. Microscopic dose distribution of photons (left) and 15 MeV/u carbon ions (right). The macroscopic dose is 2 Gy in both cases (*Scholz* [24]).

In order to deposit a relevant value of dose on the tumor volume, it is necessary to radiate it with a large number of photons, due to their low ionization probability within a single cell. The photons interactions are randomly distributed in tissues, so the ionization density, related to the LET (see Section 2.1.2), can be considered as homogeneous. Considering a typical RT photon beam, the distance d between two adjacent ionization is ~ 200 nm for all the photon range inside the patient.

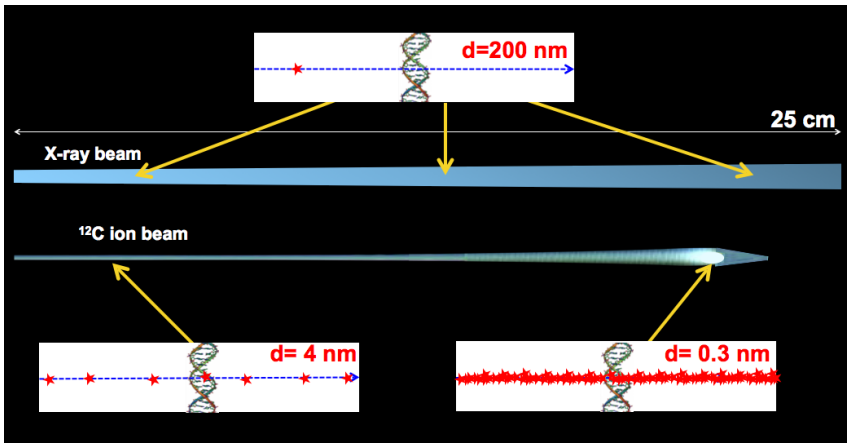

Figure 2.11. Comparison between the ionization density of an X-ray beam (top) with respect to a ^{12}C ion beam (bottom), traversing a medium from left to right. The distance d between two adjacent ionizations is shown.

Instead, the dose release distribution can vary a lot for hadrons. The distance d between two adjacent ionizations assumes very different values within the beam range inside the target. For a carbon ion, this distance can be as large as $d \sim 4$ nm at the entry point in the patient and reaches $d \sim 0.3$ nm at the Bragg peak position. Figure 2.11 shows a comparison between an X-ray beam (top) and a ^{12}C ion beam (bottom), both penetrating ~ 25 cm in a medium: the distance d between two consequent ionizations is depicted (red stars); the yellow arrows indicate where the

reported d value is assumed within the beam range. On top of that, must be taken into account that the ionization electrons produced in the light ion beam interactions have a mean free path of the order of few nanometers, providing a high probability for double ionizations on the DNA opposite strands (see Figure 2.12), especially in the Bragg peak region. The so called double strand break is more difficult to repair by the cell itself, resulting in a higher damage capability of light ions with respect to photons.

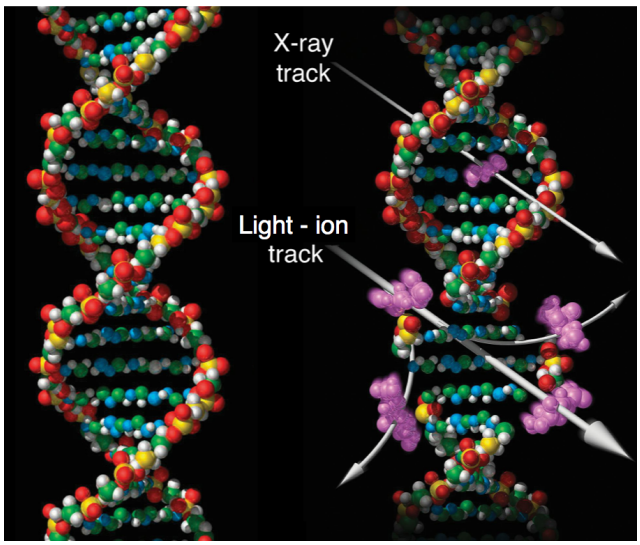

Figure 2.12. Schematic image of the DNA damages (violet) caused by X-rays and light ions.

2.2.2 Relative Biological Effectiveness

To compare the different biological effects for different radiations, the cell survival curves are commonly used, showing the relationship between the fraction of cells preserving their reproductive integrity and the absorbed dose. The ratio between survivor cells and seed cells defines the *Survival fraction* (S), shown in Figure 2.13 as a function of the Dose.

The Relative Biological Effectiveness (RBE) is an estimation of the efficiency of a given kind of radiation to kill cells with respect to photon radiation, taken as reference radiation. The RBE depends on the radiation type and energy, on the dose deposition and on the biological system (cell or tissue type). It is defined in equation 2.4 as the ratio of a reference absorbed dose of a standard radiation (D_{ref}), typically ^{60}Co γ-rays, to the absorbed dose of the radiation under study (D_{test}) that produces the same survival rate:

$$RBE_{iso} = \frac{D_{ref}}{D_{test}} \ . \tag{2.4}$$

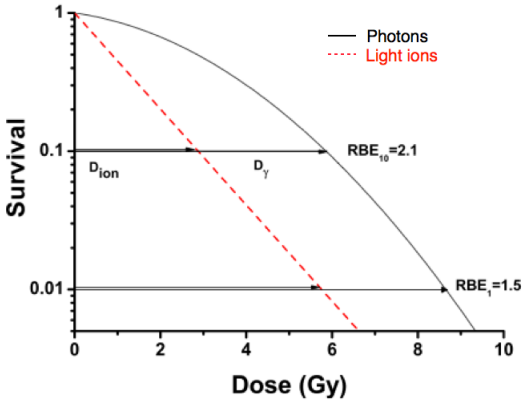

Figure 2.13. Cell survival curves and RBE determination for 10% and 1% survival levels for a typical light ion (red dashed line) and photon (black solid line) radiation. Comparing the two curves for a survival rate, the RBE is not constant with the dose even for the same radiation.

It has to be taken into account that the RBE can be different in different tissues or organs, and it can vary also inside the tumor itself.

As observed in Figure 2.13, each radiation type is characterized by its own contour shape with corresponding different RBE with respect to photons ($RBE = 1.0$). Fixing a Survival level, in Figure 2.13 is shown how to graphically determine the RBE values for a radiation type.
In a logarithmic representation the relationship between the survival fraction and the dose for densely ionizing radiations (light ions) is almost exponential, while for sparsely ionizing radiations (photons) there is an initial linear decrease followed by a "shoulder" and then an almost straight line for high dose values. Using the Linear Quadratic (LQ) model developed by *Hall* [25], the survival fraction S of cells irradiated with a dose D is described by:

$$S(D) = \frac{N_{surv}}{N_{seed}} = e^{-(\alpha D + \beta D^2)} \tag{2.5}$$

where α and β are two experimental parameters measuring the amount of lethal and sub-lethal cell damage, respectively. Depending on the tissue and kind of tumor, these parameters characterize the initial slope of the Survival curves while the ratio α/β determines the curve "shoulder" bending.

The RBE is a very powerful tool which describes the radiation "strength" in killing the tumor cells, but it cannot be uniquely assigned to a given radiation. As previously assessed, the RBE of a given type of radiation varies with energy, cell or tissue type. The situation becomes particularly complex for light ions where the RBE strongly depends on the position within the treatment beam range, *i.e.* the beam energy[2]: as shown in Figure 2.11, for fast moving light ions, at the beginning of their path in tissues, the LET is very low and hence RBE is approximately one, while for slow light ions near the BP position, the LET is very high and so it is the RBE.

[2]For protons, a typical value of $RBE = 1.1$ is used in treatment planning calculations.

A tumor volume grows if new vessels are generated to oxygenate tumor cells, but if vessels are not generated sufficiently fast or don't work well, hypoxic regions can develop within the tumor. These regions are usually deep inside the cancer mass and the radio-sensitivity of cells is significantly reduced, pushing the tumor therapy to tougher challenges. This effect may be described, in principle, by the Oxygen Enhancement Ratio (OER) parameter:

$$OER = \frac{D_{hypox}}{D} \tag{2.6}$$

where D_{hypox} and D are the biologically iso-effective doses for hypoxic and well-oxygenated tumors, respectively.

Typical OER values vary from 1 (well oxygenated tumor) to 3 (strongly hypoxic tumor). However, hypoxia, as previously indicated, is a complex phenomenon which results from an interaction between tumor growth and tumor angiogenesis. For that reason, the OER can be different for different parts of the tumor and it can highly change even within a fractionated radiotherapy course.

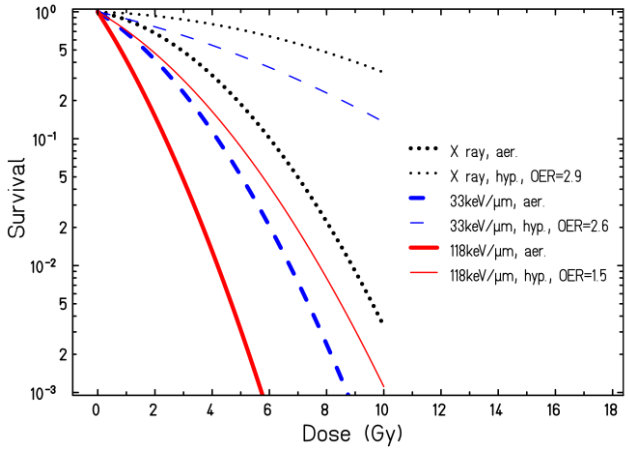

Figure 2.14. Influence of oxygen level on cell survival of human kidney cells for carbon ions at different energies and hence different LET as 33 keV/µm (blue) and 118 keV/µm (red) compared to X-rays (black). Curves based on experimental data by *Blakely et al.* [26] and *Schardt et al.* [23].

Cell survival studies carried out at LBL laboratories are shown in Figure 2.14, reporting that for the high-LET radiation (118 keV/µm), the curves for hypoxic and normal cells tends to converge, no matter about the difference in OER values (see Section 2.1.2 and 2.2.1 for the LET description). Radiations with high-LET usually have a lower OER, which effect is used to increase the power of radiation treatment.

Barendsen et al. [27], *Bewley* [28], *Furusawa et al.* [29] and *Staab et al.* [30] performed some studies observing a wide ions variety. The minimum OER values have been found for heavier ions, such as neon or carbon with respect to lighter

ions, as helium, and this constant behaviour may be directly related to the high radiation damage. As a matter of fact, the radiation damage is caused by ion direct collisions, less sensitive to the presence of oxygen compared to indirect hits induced by free-radicals, typical of X-rays. Indeed, free-radicals are less produced in hypoxic regions than in normally oxygenated cells, keeping the dose constant.

2.3 Beam Delivery Techniques

As previously reported light ion beams are a valuable tool in radiation therapy, in particular for those applications where photons are not giving positive results or surgery cannot be employed, *e.g.* for deep seated tumors surrounded by organs at risk. The difference between hadrons and photons in the dose release in tissues calls for a different way in "planning" the treatment.
The narrow extension of the BP of the hadron beams asks for an accurate and precise positioning of this dose release maximum on the tumor region. Eventual mistakes in "pointing" the BP on the tumor would imply at the same time overdosage of healthy tissues and underdosage of the tumor.
Moreover, tumors have volumes of the order of centimeters, while the Bragg peak extension is of the order of few millimeters and this difference in size must be taken into account in the clinical treatment. At the same time other important aspects have to be considered, as the minimization of the impact of the intrinsic patient body movements, due for example to breathing, or the necessity to choose the best treatment angle to spare as much as possible healthy tissues.

These problematics are deal in this section. The concept of the *Spread Out Bragg Peak* is introduced and the principal beam delivery techniques are outlined.

2.3.1 Spread Out Bragg Peak

As previously stated the BP extension is of the order of few millimeters while usually tumor volumes are of the order of some centimeters. Then it is necessary to overlap many BP using beams with different energies to cover the entire tumor region. The result is the so called Spread Out Bragg Peak (SOBP) and an example is shown in Figure 2.15.
In order to have a constant biological effect within the target volume, the planned treatment has also to take into account the RBE variation as a function of the penetration depth. As shown in Figure 2.15, hadron beams with different energies give different dose-depth distributions (solid lines), each one with its RBE value. The sum of the contributions of traversing hadrons will led to the total dose deposition (dotted line), and so to the SOBP.

Two main strategies are applied in PT facilities in order to homogeneously distribute the dose on the tumor area: passive beam modulation and active beam scanning. The first technique generates the SOBP using passive field shaping elements, as schematically shown in Figure 2.16: the narrow monoenergetic beam delivered by the accelerator is broadened by a scattering system followed by a range-modulator to modulate the beam energy, producing different Bragg peaks in different positions. The scattering system is made of several devices: the range-shifter (see Figure 2.16) shifts the SOBP in order to cover the effective target depth.

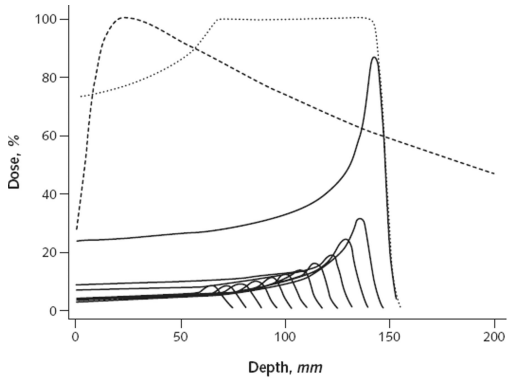

Figure 2.15. Percentage Dose distribution as a function of depth in water for a proton beam. The dotted line shows the SOBP as the result of the sum of different dose distributions (solid lines). The dashed line shows the same distribution for 10 MeV gammas (*Terasawa et al.* [31]).

The collimator and compensator are used to shield healthy tissues and adapt the beam shape to the tumor volume, respectively, in a specific way for each patient.

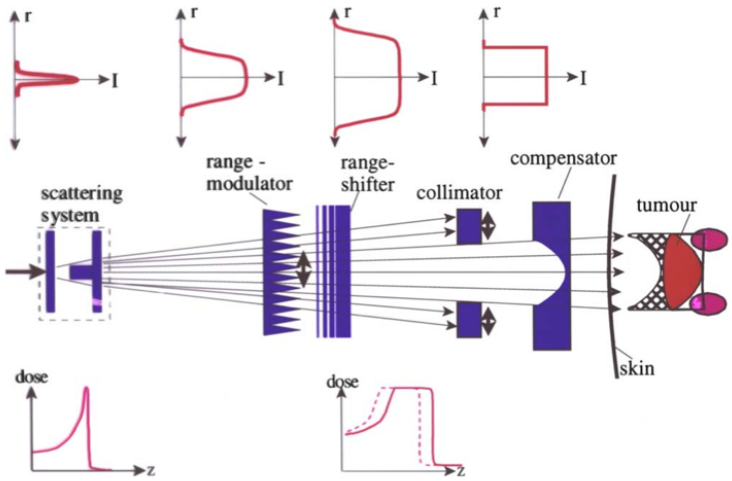

Figure 2.16. Scheme of a fully passive modulation delivery system. All the principal constituent elements are shown: the scattering system broadening the beam, the range-modulator for energy modulation and the range-shifter to spread out the Bragg peak and shift it over the tumor volume, respectively. The collimator shields healthy tissues and the compensator adapts the SOBP to the distal contour of the tumor. A non negligible dose release to normal tissues in the proximal part of the tumor (double hatched area) is outlined (*Schardt et al.* [23]).

The limitations of this passive technique is the non negligible dose delivered to normal tissues in the proximal part of the tumor due to the secondary particles (mainly neutrons) that are produced in the interaction of the beam with the scattering system.

The active beam scanning technique, instead, splits the treatment volume in several iso-energetic slices, each one divided in an elementary volumes (*voxels*) grid. A scheme of this approach is outlined in Figure 2.17. After a slice selection, each voxel is irradiated by scanning the same energy beam using deflecting magnets, giving a typical *zigzag* scan path. After an entire slice has received its planned dose, the beam extraction is interrupted, the beam energy is changed and the irradiation of another slice can start. The main advantages of the active beam scanning are that no patient specific hardware for the treatment is needed, except for the immobilization, and the possibility to vary the deposited dose on each voxel, in order to create more specific planned treatments, theoretically permitting a specific irradiation also for irregular volumes. Moreover, the beam attenuation, scattering and fragmentation are reduced.
Such delivery system is called Intensity Modulated Particle Therapy (IMPT). On the other hand, this technique requires more demanding control and safety systems with high accelerator performances on energy stability and beam exit position reproducibility.

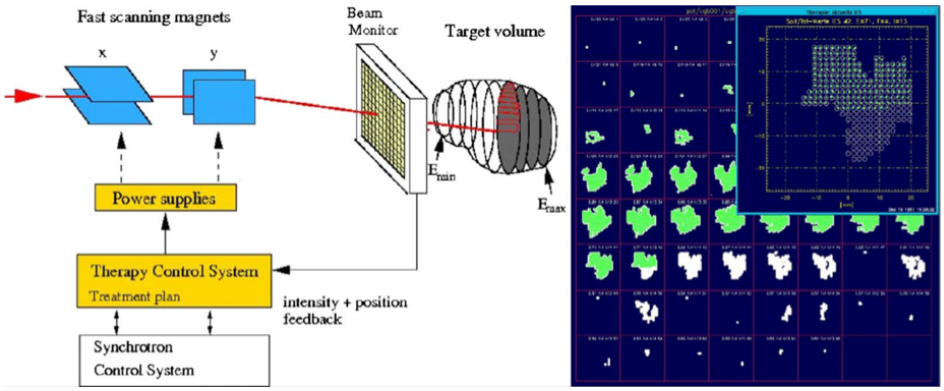

Figure 2.17. Left: GSI active scanning system working principle. The target volume is irradiated by moving a pencil beam with fast scanning magnets and the beam parameters are supplied synchronously to each pulse by a control system. Right: the entire tumor is divided in several iso-energetic slices (the slice being irradiated is expanded). During the irradiation each voxel (white dot) receives the planned dose; the green dots represent the pencil beam arrival points (*Schardt et al.* [23]).

For a long time the only two facilities that pioneered the IMPT approach were the Paul Scherrer Institute (PSI) in Switzerland and the GSI Helmholtz Centre for Heavy Ion Research (GSI) in Germany.

2.3.2 Gantries

A promising technique for the beam delivery proposes to improve the treatment quality introducing a rotational support, *i.e.* the *gantry*, in order to optimize the angles for the beam direction. Such a technique is commonly used in RT and allows for an almost free choice of the beam direction. On the other hand, such a freedom is not available in PT.

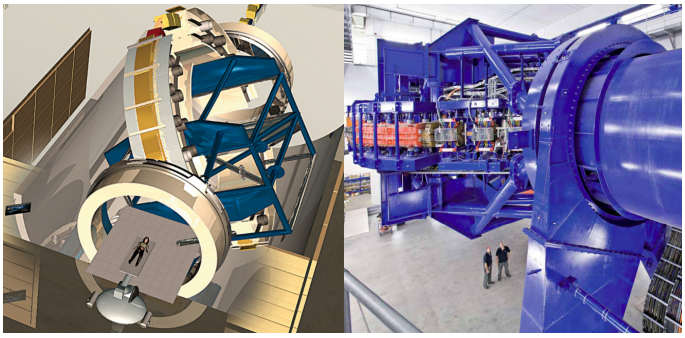

Figure 2.18. Left: 3D drawing of the HIT gantry treatment room from the HIT website [32]. Right: Gantry view from the accelerator room, courtesy of the Heidelberg University Hospital.

Considering protons, the high magnetic rigidity of the beam implies a bending radius of the order of 1 m. For carbon ions the situation is even worse (this is the reason why carbon ion facilities need larger accelerators). For example, for a 380 MeV/u carbon ion beam, having a range in water of 25 cm, the magnetic rigidity is ~ 3 times the one of a proton beam with the same range. Moreover, a high precision on the rotating movement is required. Therefore, in hadrontherapy the need of the most preferable depth-dose profile in treating tumor volumes asked for a very challenging and expensive work of engineering. The first rotating isocentric gantry for carbon ions was built at the HIT center in Heidelberg (Germany). It is a gigantic steel construction, 25 m long, with a diameter of 13 m and it weighs 670 tons. The HIT gantry is in operation for both protons and carbon ions since 2012 (see Figure 2.18).

2.3.3 Moving Targets

So far the organ irradiation with scanned beams has been performed only in stationary mode, where the patient is kept still by external supports. In this situation the target can be assumed to be fixed and the uncertainties due to patient motion (*e.g.* by breathing) are negligible.

The patient immobilization, with masks or special frames, is necessary in order to take advantage of the highly conformal dose deposition of PT. However, if the tumor is placed in an abdominal organ, breathing motion is absolutely not negligible. This could lead to variations in the path range of the beam in tissues, shifting the BP position with a high impact on the treatment quality, according to Figure 2.19 and Figure 2.20.
The breathing motion started to be considered as an important issue only recently in traditional radiation therapy, due to the low impact on photons as can be observed in Figure 2.20, but for light ions therapy, the irradiation of moving targets is a very active research field.
Some suggested options to take into account the patient motion are listed below:

1. Irradiation of planning target volume: the moving target is fully covered at any time. The limit of this technique is on the overall dose that can be given

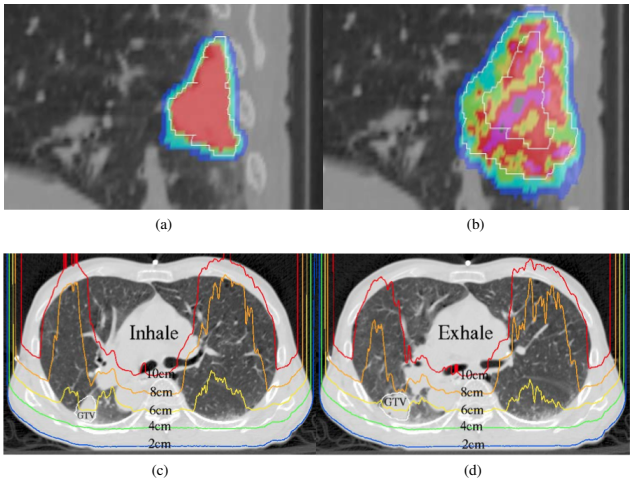

Figure 2.19. Calculated dose deposition for a lung tumor (a) without and (b) with motion, leading to severe over or under dosage in the target volume. (c) and (d) show the carbon ions range modification during the breathing phase of inhaling and exhaling, respectively. Different iso-range curves are shown. Figures courtesy of C. Bert, private communication.

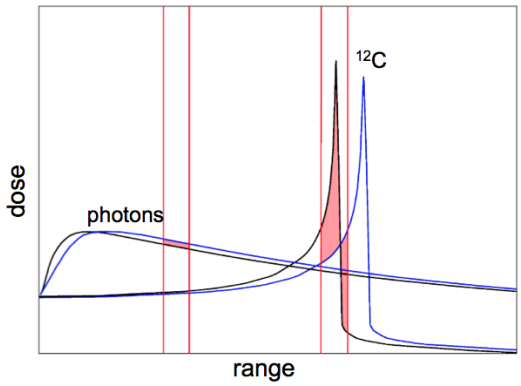

Figure 2.20. The breathing induced motion produces a shift on the BP position for the same beam traveling trough different beam paths. The black line is relative to the no-motion case, while the blue line shows the absorbed dose in the motion case. This effect is almost negligible for photons (black and blue lines are almost overlapped), but it has a huge impact at the end of the range for carbon ions: considering the BP of the no-motion case (black line) over the tumor volume (in between the second two vertical red lines), a large amount of dose will be deposited outside the tumor volume.

to the target volume, in order to minimize the dose released on healthy tissues.

2. Rescanning: if target motion and beam motion are considered uncorrelated, the variance of the average dose decreases with a factor of $1/\sqrt{N}$, with N the scan repetition times. Since the dose per scan has to be lowered, the disadvantage of this technique is on the irradiation time which is extended. Moreover, the beam monitoring ionization chambers are not sensitive to low currents.

3. Gating: this system involves the radiation management within a particular portion of the patient's breathing cycle, referred to as the "gate". The position and width of the gate within a respiratory cycle are determined by monitoring the patient's respiratory motion, usually applied in relation to a flat minimum region at the end of the exhale phase. If the irradiation is limited to the gate, uncertainties due to target motion can be reduced to less than 10% of the free breathing situation. The disadvantage of the gating system is the extended treatment time in order to ensure the delivered dose to be constant over the tumor volume.

4. Tracking: a synchronous three dimensional online motion compensation is required in order to allow the beam to follow the target movements at any time, leading, theoretically, to the same static case results. This tracking process presents some critical issues in technological development as the dynamic treatment planning and the beam delivery system should be able to permit a lateral tracking and a fast range adaptation.

Gottschalk and Pedroni [33] have recently proposed a combined method using gating and rescanning systems and it will be tested at the gantry2 at PSI.

2.4 Particle Therapy: status and prospects

In this section the present techniques involved in advanced radiation therapy treatments with photons (or electrons) and charged particles are introduced.

For both photon and charged particle therapy, the first step of the treatment configuration regards a pre-simulation of the therapy treatment: the description of the "environment" of the tumor (patient body) and the exact localization of the tumor are performed by using 3-D computed tomography (CT) or magnetic resonance (MRI) in order to create a 3-D image of the treatment area. The medical personnel decides the zones to be irradiated and the OAR that have to be spared as well as the treatment angles of the beam entrance inside the patient by means of a rotating couch or a gantry if this is available (see Section 2.3.2). Exploiting both the radiotherapist prescription and the informations from the imaging, a complex software called Treatment Planning System (TPS) computes the treatment plan. The bidimensional iso-dose curves are then outlined.

In photon therapy, the patient positioning is verified before and during the treatment with the so called "radiotherapy localization" and "radiotherapy verification" methods, respectively. These techniques use proper photographic films in order to obtain the patient's image: during the "localization" the image acquisition is

very fast, while for the "verification" a "slow" photographic film is exposed to the beam during the whole treatment time. For particle therapy, there are no "radiation verification" techniques already implemented in a clinical environment, since the charged particle beam stops inside the patient.

In a therapy treatment, the amount of radiation used varies depending on the type and stage of cancer that is treated. A typical radiation treatment foresees, for example, a total dose provided to a patient of about $60 - 70$ Gy for a solid epithelial tumor, while lymphomas are treated with $20 - 40$ Gy. The issue related to the maximum dose release allowed for a given treatment can be somehow overcome by fractionating the total released dose: in this case, the human cells are able to repair the DNA damages caused by radiations exposition. For the solid epithelial tumor, the provided total dose of about $60 - 70$ Gy can be delivered in $30 - 35$ daily fractions of 2 Gy each.

Taking into account that, especially for PT techniques, the dose released to tissues surrounding the tumor volume is anyway lower than the dose released over the cancer area, where the highest destructive power of radiations is concentrated, the rate of the DNA repairs is thus higher for healthy cells than for cancer cells. Moreover the DNA repair is less effective in cancer cells than in normal cells.
The hypofractionation, a treatment schedule in which the total dose of radiation is divided into large doses, is today considered as a viable option in photon and charged particle therapy: the possibility to reduce the total number of treatment sessions from ~ 30 to $4 - 5$ sessions implies a clear advantage for the patient quality of life and a more effective use of the treatment centers.

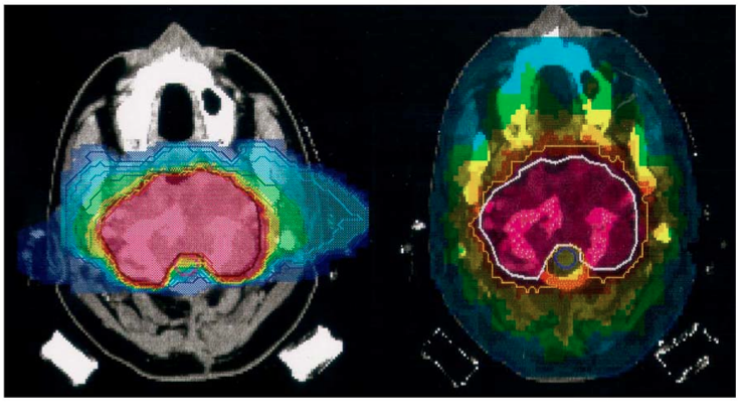

Figure 2.21. Treatment plans comparison for a target volume sited in the skull base irradiated with two fields with carbon ions (left) and nine fields with IMRT (right). A comparable dose conformation over the tumor volume can be achieved with both techniques, but the use of carbon ions would reduce dramatically the integral dose to the surrounding healthy tissues, sparing OAR in proximities (*Durante and Loeffler* [34]).

Concerning the technological challenges required by the PT, this new and very conformal irradiation technique asks for sophisticated treatment plans, as well as for techniques able to keep under control during the treatment the beam position and dose delivered, the absorbed dose by tissues and finally the patient positioning.

In spite of the intrinsic complexity of the PT treatment, a clear example of the advantage with respect to the modern and effective conventional RT (IMRT) is given in Figure 2.21 where the comparison of a treatment plan for photon therapy and particle therapy is shown. The tumor volume sited in the skull base is irradiated with two fields of carbon ions (left) and nine fields with IMRT (right). As can be observed, despite for both therapies the maximum dose is localized over the tumor area, the delivered dose to the surrounding tissues is much more extended in photon therapy than in particle therapy.

In the following subsection, the difference between proton and carbon ion beams, which are the mainly hadron beams used in PT, are described and some additional aspects are underlined in order to ensure high results of particle therapy in cancer healing.

2.4.1 Protons and ^{12}C ions

In order to give a wide overview and a deep insight on the two main technologies employed in hadrontherapy, in this section the main advantages and disadvantages of protons with respect to carbon ions will be briefly discussed.

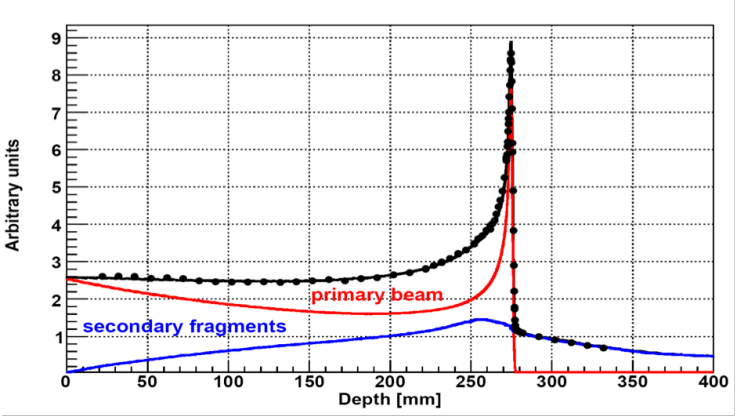

Figure 2.22. Bragg curve as a function of the depth in water for a 400 MeV/u carbon ion beam. The experimental data (dots) [35] [36] and the FLUKA calculation (solid line) [37] [38] are shown. The dose contribution from primary ^{12}C ions (red line) and secondary fragments (blue line) is also reported.

As introduced in Chapter 1, light ions can undergo nuclear fragmentation when interacting with the target nuclei (fragmentation in air has a much smaller impact). Low Z fragments are then produced, leading, from a therapy treatment point of view, to several drawbacks: fragments have longer range, different directions and different RBE with respect to primary particles.

The result of the nuclear fragmentation is visible in the Bragg peak tail, shown in Figure 2.22 for carbon ion therapy (*E. Haettner* [35], *E. Haettner et al.* [36], *A. Mairani* [37], *G. Battistoni et al.* [38]). On the other hand, protons nuclear fragmentation is a negligible effect and the relative depth-dose curves show an almost

sharp falloff.

Another physical aspect that has to be taken into account when comparing protons and carbon ions is the multiple scattering. As described in equation 1.13, the MS deflection angle is inversely proportional to the incident particle mass. Therefore, carbon ions suffer much less lateral beam spread than protons (see Figure 2.5 and Figure 2.6). Figure 2.23 shows the comparison between a treatment plan with carbon ions (left) and protons (right). A lower beam spread expresses a more localized dose deposition and hence a particle therapy with carbon ions will follow more precisely the tumor volume conformation.

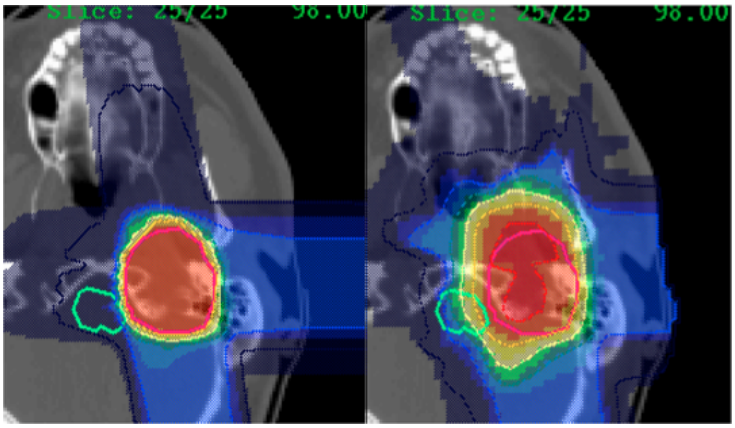

Figure 2.23. Treatment planning comparison for carbon ions (left) and protons (right). Carbon ions shows a more accurate tumor conformation dose deposition and normal tissue sparing due to lower multiple scattering effect with respect protons. Pictures courtesy of GSI (left) and iThemba labs, Cape Town (right).

Another advantage of carbon ions with respect to protons is the high-RBE. Carbon ions are characterized by so dense ionizing tracks, as shown in Figure 2.2 and Figure 2.11, that the probability of double ionizations on both DNA strands is much higher when compared to sparsely ionizing proton tracks, making light ions more effective in tumor cells killing. Even the OER is enhanced for light ions than for protons, reaching a value of ~ 1 when the radiation is close to the BP region. Figure 2.24 shows the RBE as a function of the LET for different kind of particles: carbon ions appear to have a RBE behaviour well suited for tumor treatment, with low RBE at "high" energy (in the healthy tissues) and high RBE when particles stops inside the tumor region (see Section 2.2.2).

However, when a comparison between proton and carbon therapy is made, the cost and the equipment size must be taken into account: the major advantage of proton therapy is the lower cost proton facility with respect to a carbon ion accelerator. The magnetic rigidity, defined as $R = p/q$, with p the particle momentum and q its charge, is twice larger for carbon ions than for protons (being the carbon mass twelve times the proton mass and the carbon ion charge six times the proton one), as mentioned in Section 2.3.2. This means that carbon ion accelerators need a

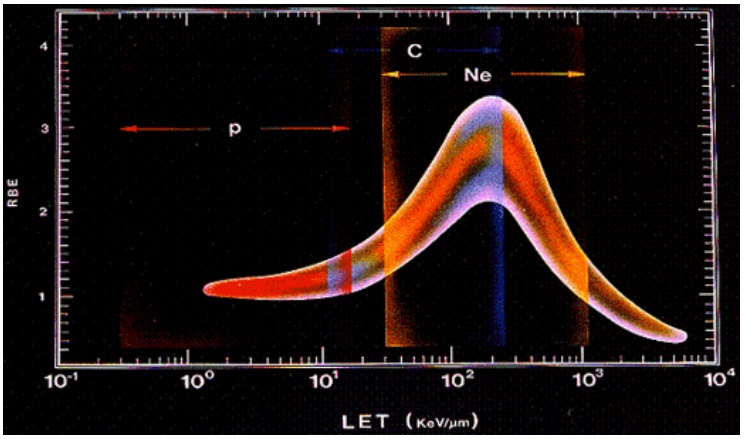

Figure 2.24. Relative biological effectiveness as a function of the linear energy transfer. Carbon ions

larger radius than proton accelerators. Therefore, to reach typical hadron therapy treatment energies, cyclotrons (normal or super conducting) that can be easily fit into a hospital environment are usually used for proton therapy. Carbon ions need much bigger (and so expensive) facilities such as synchrotrons (with a diameter of tens of meters).

Nowadays, other light ions are under study for future PT applications, such as helium and oxygen ions: ^{4}He beams suffer less the MS effect with respect to proton beams and have a RBE value between protons and carbon ions RBE; ^{16}O ions have a greater RBE with respect to ^{12}C due to a very high LET value ($LET \propto Z^2$) (see Section 2.1.2). Oxygen ions can also be used to treat hypoxic zones of radioresistant tumors. On the other hand, light ions nuclear fragmentation has to be considered, taking into account that the effect is enhanced for high Z ions (see Section 1.1.3).

The particle therapy advantages concerning the conformal dose deposition over the tumor volume, the higher biological effectiveness and healthy tissues sparing with respect to the photon therapy have been outlined and show that PT seems a promising alternative to traditional RT for those applications where the use of photons or surgery is particularly discouraged (*e.g.* treatment of deep seated tumors or malignancies near organs at risk). The PT is a quite young technique and a large effort to improve the effectiveness of this treatment in the clinical practice is on going all over the world. One of the main issues to provide better treatment quality is the monitoring of the maximum dose release position, *i.e.* the Bragg peak position. This information during the treatment, *i.e. on-line*, is still missing and since the particle therapy dose deposition is very localized with respect to photon therapy, an instrument of control on BP position is required.

As previously stated, both a beam delivery problem or even a mismatch between the patient physiology and the CT time with respect to the treatment time can easily take to overdosage of healthy tissues and underdosage of the tumor region. Considering that in PT all the beam is absorbed in the patient body, techniques

based on secondary particles produced in the interaction of the charged particle beam with tissues should be developed and operated in a clinical environment.
In the next chapter, the dose monitoring aspects and the secondary particles on which a monitoring device could rely on will be described.

Chapter 3

Dose Monitoring in Particle Therapy

The high precision of particle therapy in spatial releasing the dose delivered to the patient, as presented in the previous chapter, asks for new and necessary dose monitoring techniques.
In order to ensure a high quality particle therapy treatment, it has to be verified that the delivered dose amount is released within the tumor contours during the treatment, *i.e.* on-line, since the heavy ions dose release is very sensitive to patient misplacements (see Section 2.3.3) and morphological variations (*Karger et al.* [39]). Therefore, in order to take advantage of hadrontherapy clinical benefits, this particle therapy special requirement would allow the possibility to intervene during the patient irradiation and give a stop signal to the treatment in order to modify and correct it with respect the TPS (*Pedroni et al.* [40]).
In this chapter, a brief state of the art of the methods already applied or still under evaluation for particle therapy dose monitoring is presented.

3.1 Secondary products

Protons and heavy ions have the typical feature to release almost all their energy at the BP, which characterize the hadrontherapy demanding to have the BP over the tumor volume in order to maximize the beam damage power on cancer cells. This peculiar interaction between charged particles and matter doesn't make possible the use of a direct beam particles detection to perform dose monitoring, as for X-rays beams, since charged particles stops into the patient tissues in proximity of the BP. At present, the existing techniques for dose monitoring in hadrontherapy are based on the detection of different secondary particles produced in the beam interaction with matter.
In this section, the main secondary particles produced in the interaction between a hadron beam and the target are outlined.

3.1.1 PET Gammas

The Positron Emission Tomography (PET) exploits the simultaneous detection of 0.511 MeV back to back photons produced in the annihilation between stationary

positrons and electrons of the medium. Stationary positrons come from β^+ decays, as described in equation 3.1:

$$ {}^{A}_{Z}X \rightarrow {}^{A}_{Z-1}Y + e^+ + \nu_e \ . \tag{3.1} $$

A schematic view of the $\gamma - \gamma$ production is shown in Figure 3.1.

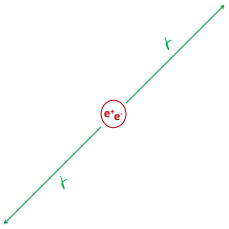

Figure 3.1. Schematic view of the *back to back* gammas with $E_\gamma = 511$ keV produced in the positron-electron annihilation.

The PET first employment is in the functional diagnostic field, obtaining informations on tissues metabolism, but it is also used as a dosimetric technique in hadrontherapy treatments. Pursuing this last application, β^+ emitters nuclei can be activated during the interactions between the hadron beam and the phantom by the nuclear fragmentation of the beam projectiles (if heavy ions) or of the target nuclei. The detection of PET gammas, which are the photons produced after the β^+ decays, makes possible to use the PET as an *in situ* and non invasive dose monitoring technique (*Parodi et al.* [41], *Agodi et al.* [42]), since the distribution of β^+ activity in function of the beam range in tissues is correlated to the released dose distribution, as shown in Figure 3.2.

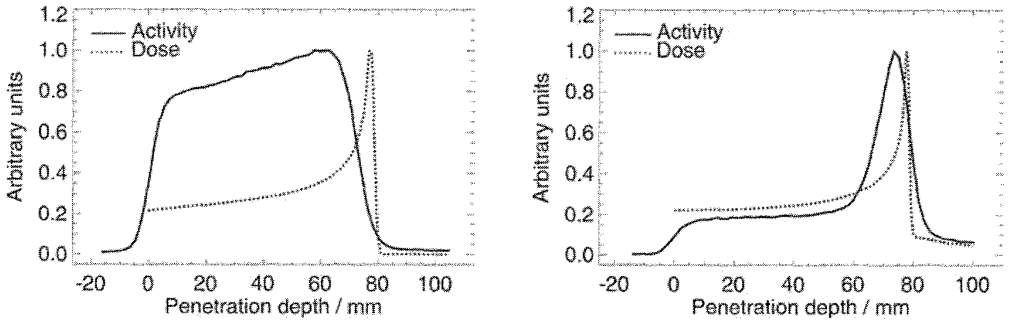

Figure 3.2. PMMA target activation, irradiated with a 110 MeV proton beam (left) and with a 212 MeV/u carbon ion beam (right). The solid line shows the distribution of the β^+ activity in function of the depth, while the dotted line indicates the dose released distribution of the primary beam in function of the depth (*Parodi* [43]).

PET gammas are detected by scintillation detection systems, as in the majority of PET tomographers, using two opposite scintillating crystals in order to detect two PET photons in temporal coincidence that have originated from a single annihilation

event in the body, somewhere along a line between the two detectors. The scintillation process involves the conversion of high-energy photons into visible light via interaction with a scintillating material. The incident photon on the scintillator creates an energetic electron by Compton scatter or by photo-electric absorption. When the electron passes through the scintillator, it loses energy and excites other electrons of the material which decay back to their ground state, giving light. The scintillator is optically coupled to a photomultiplier tube (PMT) which generates an electrical signal in response to the incident light upon its face.

The electrons generated by Compton scatter and photo-electric absorption have different energy distributions. In photo-electric absorption, all the photon energy is transferred to the electron, and the energy distribution of the photo-electrons is sharply peaked close to the energy of the incident photon. In Compton scatter, the recoil electrons have a larger range of energies, depending on the scattering angle. A typical energy distribution for electrons involved in interactions with 511 keV photons is shown in Figure 3.3.

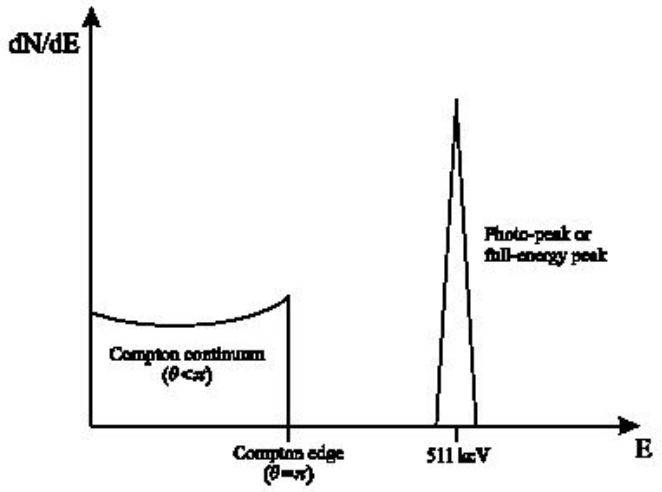

Figure 3.3. Features of a typical energy distribution for electrons involved in interactions with 511 keV photons (*Badawi* [44]).

For real scintillation detectors exposed to mono-energetic photons, the energy measured is the total energy deposited by the photon in the detector and not that of the electron generated by the initial interaction, because photons initially interacting by Compton scatter may then be involved in further interactions within the detector. In a sufficiently large detector, most Compton-scattered photons will eventually deposit all their energy, and most events will be registered in the photon energy peak, *i.e.* the "full-energy peak" or "photo-peak".
In small detectors, photons can escape after depositing only part of their energy in the scintillating crystal, and the measured energy distribution is closer to that shown in Figure 3.4. The energy distribution is also blurred by the not mono-energetic incident radiation that could be undergone by Compton scatter prior to detection and by the energy resolution of the detector itself, defined as the ratio of the full-width at half-maximum (FWHM) to the energy value at the full-energy peak. Some events could have a greater energy than the full-energy peak, when photon interactions

with the detector occur so close together in time that they cannot be resolved as separate events.

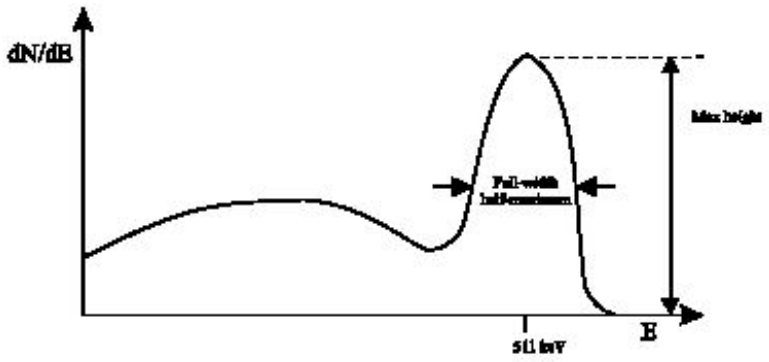

Figure 3.4. Features of a typical energy distribution measured by a scintillation detector system exposed to 511 keV photons (*Badawi* [44]).

The number of events in the full-energy peak increases with increasing detector size. On the other hand, large detectors reduce the spatial resolution of the system. The number of events in the full-energy peak can also be increased by scintillators with a large value of effective atomic number (effective Z). The linear attenuation coefficient also increases with the effective Z, enhancing also the sensitivity. The energy resolution of the detector can be improved with the light yield of the scintillator itself, increasing the number of scintillation photons impinging on the PMT face, giving a higher statistical quality of the signal from the PMT. Summarizing, the qualities required in a scintillator for the detection of PET gammas are a large value of effective Z, a high light yield, a low self-absorption factor for the scintillation light and an index of refraction close to the one of glass, in order to improve the optical coupling between the scintillator and the PMT. Moreover, it is important for the decay time of the scintillator to be short, in order to provide fast signals and good time resolution for coincidence detection.

During a hadrontherapy treatment with a ^{12}C ion beam, the main β^+ emitting isotopes, which are also the only detectable, have an emission time of PET gammas that ranges from ~ 2 min, for the ^{15}O radioactive isotope, to ~ 20 min for the ^{11}C radioactive isotope (*Pawelke et al.* [45]). For PET photons detection, it has to be taken into account that the patient irradiation time is of the order of few minutes to ~ 10 min, depending on the treatment, and that only limited geometries are allowed in the treatment rooms, so only a double head PET could be used during the treatment time instead the scintillating crystals full-ring surrounding the patient body employed in the PET tomographers. Moreover, the statistics of β^+ radiation is dominated by the background coming from random coincidences (detection of two photons arising from two separate annihilations) and scattered events (photons undergone by Compton scattering in the target) within the preset time window. The low PET gammas statistics is not sufficient to perform an on-line dose monitoring, despite the knowledge that the distribution of β^+ activity in function of the beam

range in tissues is correlated to the released dose distribution.
Thus, the PET photons detection for dose monitoring purposes is today used *in situ* and off-line, after the patient irradiation time, even if the radioactive nuclides interact with the metabolic processes (*e.g.* blood circulation), deteriorating the overall image quality and the relation between the deposited dose and the β^+ activity. However, this latter effect is well taken into account by Monte Carlo simulations.

The information on the Time Of Flight (TOF) of PET gammas impinging on two opposite detectors has then been used in order to widen the signal to background ratio and reduce the standard PET images artifacts, thanks to PET scanner employing detectors with time resolutions of the order of a nanosecond (*Crespo et al.* [46]). Using this technique called TOF-PET should be possible an on-line dose monitoring, having speeded up the data analysis time and having reduced, with the TOF information, the volume of the observed region. The study and research in the TOF-PET direction are today of great interest. The off-line PET for dose monitoring purposes in hadrontherapy has been already tested on several clinical cases at the Massachusetts General Hospital and at the HIT centre (*Parodi et al.* [47] [48]).

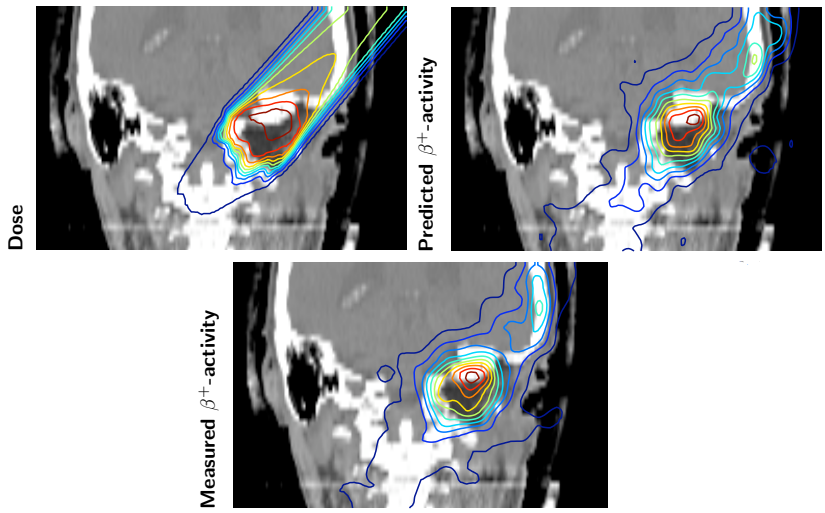

Figure 3.5. Delivered dose distribution (top left) compared with respect to the β^+ activity predicted by the treatment plan (top right) and measured (bottom) after the irradiation of a skull base tumor with a carbon ion beam at the GSI laboratories. The distributions are superimposed to a cranium CT image. The brainstem is the OAR in tumor proximity, pointed out in white colour. It is visible how the carbon ions stop before the brainstem with respect to prediction (*Crespo et al.* [50]).

In Figure 3.2 is shown how the β^+ distribution activity is related to the dose released distribution in function of the penetration depth of a proton beam (left) and a carbon ion beam (right) in a polymethil methacrylate (PMMA) target. For the same amount of absorbed dose, proton beams don't go into fragmentation, inducing a lower β^+ activity with respect to the one induced by carbon ions. As a consequence, the activity is correlated to the Bragg peak but it is not directly proportional, without showing a clear relationship between the induced β^+ activity

and the dose released profile, as for carbon ions. Although, the total activity induced by protons per Gy is about three times larger than the one induced by carbon ions, because to release the same amount of effective dose it is necessary a protons number 40 times higher with respect to carbon ions (*Parodi et al.* [49]). Nowadays, in oncological radiation therapy, the released dose control is realized comparing the β^+ activity measured with PET with respect to Monte Carlo simulations based on the TPS, as shown in Figure 3.5.

3.1.2 Prompt Gammas

The issues of the PET technique ask the scientific community to develop novel techniques for dose monitoring in hadrontherapy. Recent studies have shown that, in proton and carbon ion therapies, the prompt photons spatial distribution is related to the dose released distribution in tissues, as shown in Figure 3.6 (*Min et al.* [51], *Testa et al.* [52], *Agodi et al.* [53] [54]). Prompt photons are the photons produced by the de-excitation of nuclei excited in the interactions between hadrons and matter, emitted in a time of the order of a nanosecond. Considering a proton beam impinging on a phantom composed by carbon-12 nuclei, the reaction between a proton and a carbon nucleus giving a prompt photon emission can be written as the following:

$$\begin{aligned} p + {}^{12}C &\rightarrow p' + {}^{12}C^* \\ {}^{12}C^* &\rightarrow {}^{12}C + \gamma_{4.44\ \mathrm{MeV}} \ . \end{aligned}$$

These production reactions make the prompt photons emission an independent mechanism from the patient metabolism.

For the prompt gammas detection, scintillating crystals can be used and there are less limitations in detector geometries, since prompt gammas are emitted independently one from the other, and the faster emission time with respect to the PET gammas allows for a detection during the patient irradiation time. A standard Single Photon Emission Computed Tomography (SPECT) technique is performed using gamma cameras, which, in principle, could also be employed in the dose monitoring using prompt photons detection. An example of gamma camera is shown in Figure 3.7. Gamma cameras are built with two main elements: the collimator and a system of scintillating crystals for the photon detection and localization. In Figure 3.7 is shown a system of collimators, placed one close to another, but, usually, the collimator is a plate of absorbing material, as lead, with holes in order to preserve only the incident radiations in the desired direction and absorb the other ones. After each hole there is a scintillating detector in order to collect and localize the prompt gammas radiation. The distance between the holes and their length in the collimator, as the detector features and geometry, depend on the energy of the prompt gammas incident radiation and they are responsible for the spatial definition of the system and for the detection efficiency. For example, the more energetic photons are able to pass through a greater length of lead than the less energetic ones, and a thick scintillating crystal is required for the more energetic gammas in order to increase

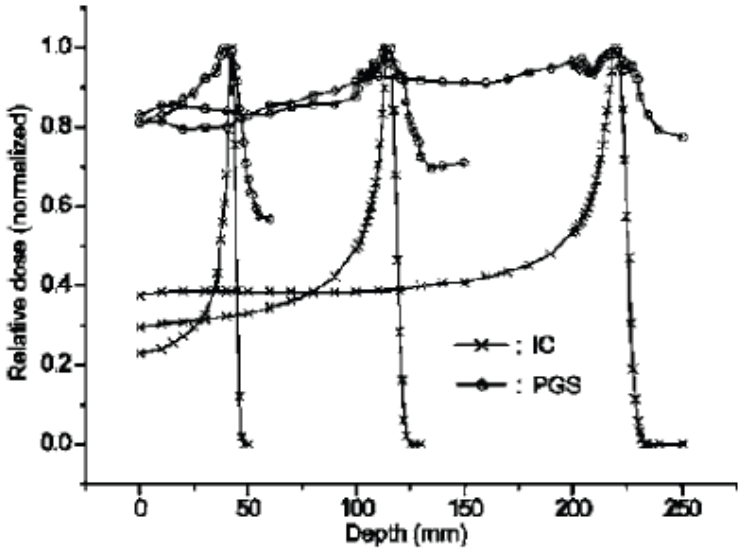

Figure 3.6. Comparison between the released dose distribution as a function of the depth in water for 100 MeV, 150 MeV e 200 MeV proton beams, measured by a Ionization Chamber (IC), and the prompt radiation measured with a Prompt Gamma Scanner system (PGS), placed at 90° with respect to the beam incoming direction. A correlation between the Bragg peak and the prompt radiation within $1 - 2$ mm for the low energy beam (100 MeV) is observed (*Min et al.* [51]).

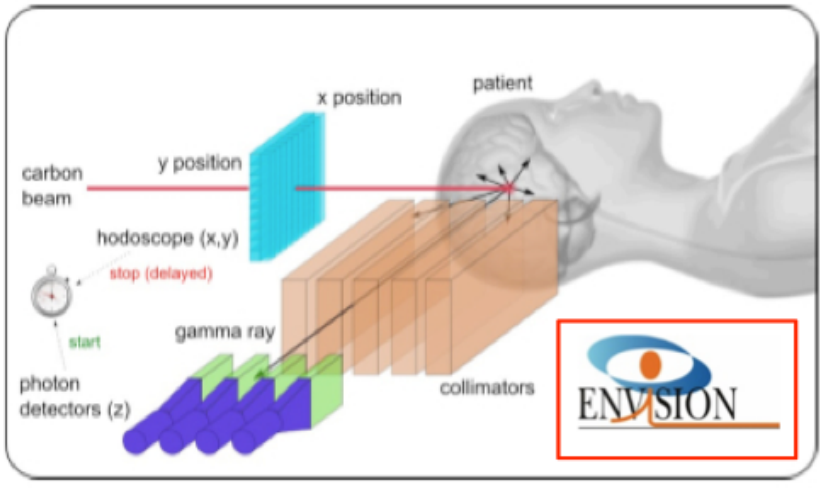

Figure 3.7. Gamma camera: schematic view.

the detection efficiency, but the spatial resolution for low energy photons is decreased by their scattering within the detector. Therefore, the geometry of gamma cameras have to be designed in order to achieve the best compromise between the quantity of signal and background (neutrons or Compton photons scattered) collected.

The main issue in using gamma cameras to detect prompt photons coming from the interaction of a hadron beam with the phantom is that the measured energy spectrum of prompt gammas ranges between $1 \div 7 - 10$ MeV (*Agodi et al.* [53] [54], *Bellini et al.* [55]). An example of a prompt photon energy spectrum is shown in Figure 3.8. This wide range of energy (up to 10 MeV) would require very thick collimators with the consequent decrease of statistics. Moreover, the size of such collimators would be unmanageable in a treatment room.

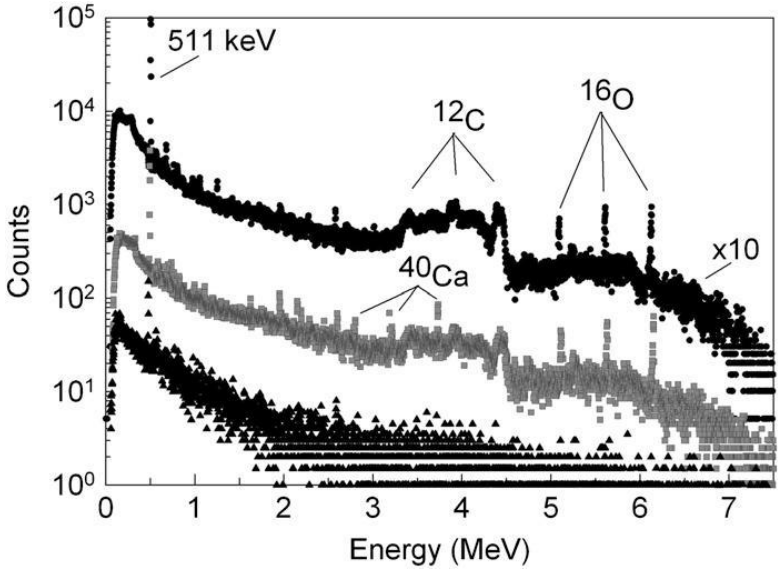

Figure 3.8. Energy emission spectrum of prompt photons measured during the irradiation of a lucite target (black circles) and a bone equivalent target (grey squares) and the measured background (black triangles). The prompt emission peaks are visible, as the single and double escape peaks, for the major constituent nuclei of the targets (carbon, oxygen and calcium). The lucite spectrum has been multiplied by a factor 10 for a better visualization of the spectrum itself [56].

The photon's Compton cross section is described by equation 1.19 and it depends both on the photon incident energy $h\nu$ and on the atomic number Z of the target material. Figure 3.9 shows the relative importance of the three major types of γ-ray interactions, already described in Section 1.3, as a function of the photon incident energy and the atomic number of the target material. For prompt gammas with energies between $1 - 10$ MeV, the Compton effect is dominant. Therefore, another approach proposed by *Kabuki et al.* [57] is to realize a Compton camera to track the prompt gammas, implementing a scatterer and an absorber with a good energy resolution, able to contain Compton electrons and scattered gammas and then reconstruct the original gamma direction via software.

Different sophisticated solutions can be found in astrophysics applications where detectors reconstructing both the Compton electron and scattered gamma trajectories

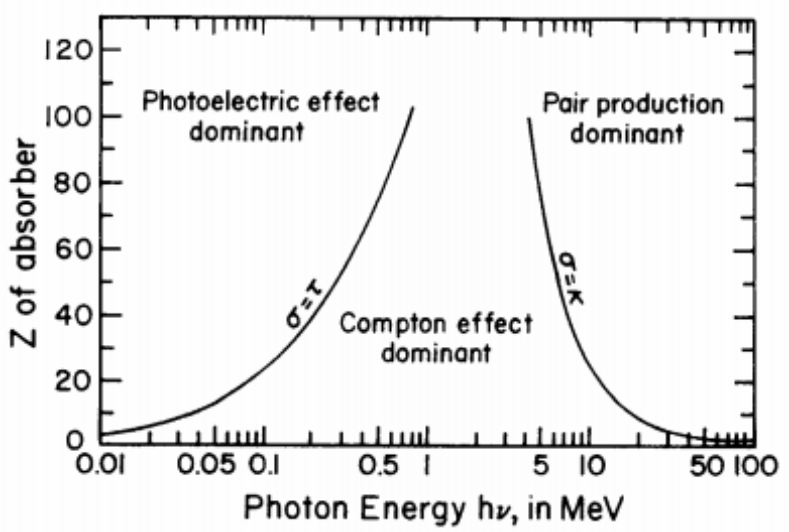

Figure 3.9. Relative importance of the three major types of γ-ray interactions, already described in the first chapter, as a function of the photons incident energy and the atomic number of the target material. The solid lines indicate the values of Z and photon energy $h\nu$ for which two types of effect are equal.

after a Compton interaction within the detector itself are used (*Kormoll et al.* [58]). Anyway, since the number of secondary prompt gammas produced during a standard particle therapy treatment is limited, and considering the non negligible neutrons background in the treatment rooms, the dose monitoring using prompt photons could suffer from low statistics. Widening the detector dimensions, and so the detector angular acceptance, the statistics can be enhanced but there are always geometrical constraints in terms of space availability of the treatment rooms. For the mentioned reasons, prompt gammas have never been used, so far, for dose monitoring purposes in a clinical environment.

3.1.3 Secondary Charged Particles

Braunn et al. [59] and *Agodi et al.* [60] [61] have proposed recently to monitor the Bragg peak position using secondary charged particles produced in the interaction between the therapeutic beam and the target. Such fragments are produced within the whole beam path inside the target and the profile of their longitudinal emission distribution has be shown to be related to the beam range itself, and so to the beam energy, *i.e.* to the BP position, as shown by *Agodi et al.* [60] [61] and *Piersanti et al.* [62] (see Figure 3.10).
Secondary charged particles are mainly protons and other hydrogen isotopes, such as deuterons and tritons, with emission times of the order of few nanoseconds to ~ 20 ns (depending on the beam range inside the target). The main production processes are the inelastic collisions between the beam projectiles and the target atomic electrons and nuclear reactions, as described in Section 1.1. Charged particles emission energy can reach values of $80 \div 150$ MeV, depending on the primary hadron beam energy, but, together with a production energy threshold, an "exit" energy threshold has to be considered. In fact, the material thickness that such fragments

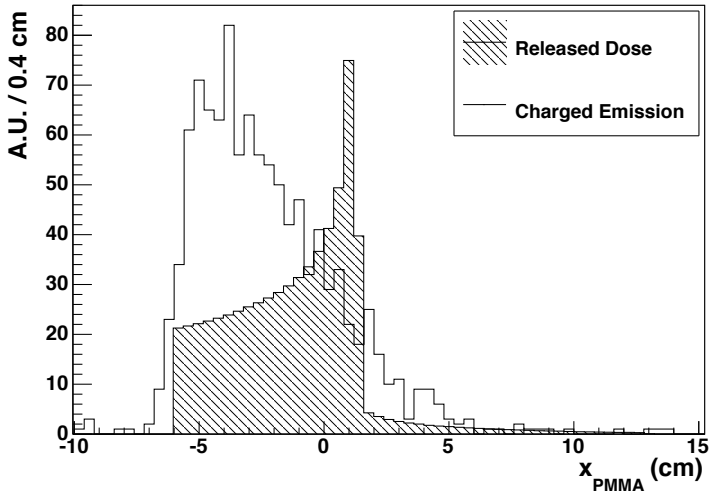

Figure 3.10. Measured longitudinal emission profile (x_{PMMA}) of secondary charged particles (solid line) produced in the interaction of a 220 MeV/u carbon ions beam impinging on a PMMA target and the corresponding expected dose deposition distribution (hatched area) (*Piersanti et al.* [62]). Details on this measurement in Section 4.4.4 .

have to cross before exiting the target and reaching the detector could be enough to stop the secondary charged particles within the phantom, depending on the stopping power value (see equation 1.2).
The detection of such particles can be done with high efficiency tracking systems as, for example, drift chambers, scintillating fibers, silicon detector. Anyway, detectors with tracking resolutions higher than the contribution of the multiple scattering effect, suffered by secondary charged particles inside the patient (see Section 1.2.2), are not interesting to the aim of this work, as will be explained in detail in the following chapter. Although, the principal issue in using charged fragments as a BP position "probe" is the production statistics, that is lowered with increasing angles with respect to the beam incoming direction. This occurs especially for proton beams, where secondary charged fragments come from the target nuclei fragmentation only. Large angles such as 90° or 60° with respect to the beam direction are chosen thinking to a possible detector that could be placed in a treatment room close to a patient for on-line dose monitoring intents. For smaller angles the statistics would increase, but it would be more difficult the detector placement without strike or annoying the patient under treatment. Therefore, it is necessary to have a large solid angle detector in order to increase the collected statistics of such fragments.

The idea to use secondary charged particles for dose monitoring purposes has arisen only in the last years. Moreover, at first, nobody believed that charged particles had a sufficient flux to use them for BP position monitoring, especially at large angles with respect to the beam direction, since high energetic secondary charged particles production is favored by forward emission, varying the energy spectrum with the emission angle, as previously stated.
Agodi et al. [60] [61] performed the first experiment in order to assess the feasibility

of a dose monitoring technique based on secondary charged particles detection at large angle (90°).
Hence, knowing that the emission distribution profile of secondary charged particles is related to the beam range inside the target, and that a sufficient statistics can be produced at large angles with respect to the beam direction, additional measurements have been performed by *Piersanti et al.* [62] at the GSI laboratories and by *Gwosch et al.* [63] at the HIT centre. Some methods to correlate the emission distribution profile to the BP position have been proposed, in order to use the detection of secondary charged particles for the on-line dose monitoring purpose. It has been also shown a clear correlation between the steep rise of the emission distribution profile and the beam entry channel in the phantom, which could in principle give a tool in order to ensure the patient positioning during a particle therapy treatment. All those secondaries characteristics will be described in detail in the next chapter, from data collected by the ARPG group in experiments with carbon ion beams impinging on a PMMA thick target.
Additional data from PMMA irradiation with therapeutical helium and oxygen beams have been collected at the HIT centre by the ARPG group and are about to be published.
Details on advantages and limitations of a dose monitoring technique based on the secondary charged particles detection will be described in the next chapter.

In summary, nowadays PET and SPECT are the only technologies under evaluation for dose monitoring in particle therapy that have been already tested in a clinical environment. However, those systems, based on photons detection, do not appear to provide an effective feasibility for on-line monitoring purposes, since the low PET photons statistics and the prompt photons wide energy spectrum for the PET and SPECT technologies, respectively. Anyhow, the possibility to employ Compton cameras for prompt photons detection or rely on secondary charged particles could open up new opportunities for the on-line dose monitoring research field.
The primary measurements on secondary charged particles for BP position monitoring, that assessed the feasibility of a novel on-line technique based on charged fragments detection at large angles with respect to the beam direction are part of this thesis work, and some methods to correlate the emission distribution profile of secondary charged particles to the BP position have been proposed.

Chapter 4

Measurement of secondary particles production

As stated in the previous chapters, a dose monitoring system is a needed device for particle therapy. The monitoring of the Bragg peak position during particle therapy treatment can be done exploiting secondary neutral and charged radiation produced in the interactions between the beam and the target, as mentioned in Chapter 3.
In my doctorate years, my main activity was focused on the research for an on-line dose monitoring technique in particle therapy. In order to characterize the secondary radiation production, several experiments *on beam* have been performed: a PMMA block has been irradiated with different therapeutic hadron beams of different energy values. In order to better understand the physics of nuclear interactions of the beam projectiles with the target nuclei, the energy spectra and production rates of prompt photons and secondary charged particles have been evaluated. The obtained measurements have been used to design and develop a dose monitoring device, that will be described in the next chapter.
This experimental activity has led to several publications describing measurements on PET gammas (*Agodi et al.* [42]), prompt photons (*Agodi et al.* [53] [54]) and charged particles (*Agodi et al.* [60] [61]) produced from the interaction of an 80 MeV/u fully stripped ^{12}C beam with a thick PMMA target, performed at the LNS-INFN laboratories (Catania, Italy). The measurement on charged particles production (*Piersanti et al.* [62]) from a 220 MeV/u fully stripped ^{12}C beam impinging on a PMMA thick target was instead performed at the GSI laboratory (Darmstadt, Germany). Such beam energy values have been selected in order to collect and study two different samples of secondary fragments produced during carbon ions irradiation of superficial tumors (*i.e.* 80 MeV/u) or deeper seated tumors (*i.e.* 220 MeV/u).

The choice to investigate the secondary fragments production from carbon ions has two main motivations: carbon ion beams are a viable solution for tumor treatment due to their dose-depth features, even with respect to the more widely spread proton beams (see Section 2.4.1). The nuclear interactions of carbon ions with matter need to be further investigated to match the desired precision level needed in PT.

This experimental campaign included also the measurements of secondaries induced by ^4He and ^{16}O ion beams performed at the HIT center [32]. Both these beams are of interest for future applications of hadrontherapy, as reported in Section 2.4.1. The analysis of this data taking is still ongoing and in this thesis preliminary results will be presented both on prompt photons and on charged secondaries.

In this chapter it is described the experimental campaign and the simulation of the experimental setup is outlined. The data analysis and the results of the study of prompt photons and secondary charged particles radiations are then reported.

4.1 Experimental Setup

The setup geometry is common to all the experiments on beam previously cited, with some minor differences due to the beam energy and specific data taking features. The experimental setup is shown in Figure 4.1 for the data taking at the LNS (top) and GSI (bottom) laboratories.

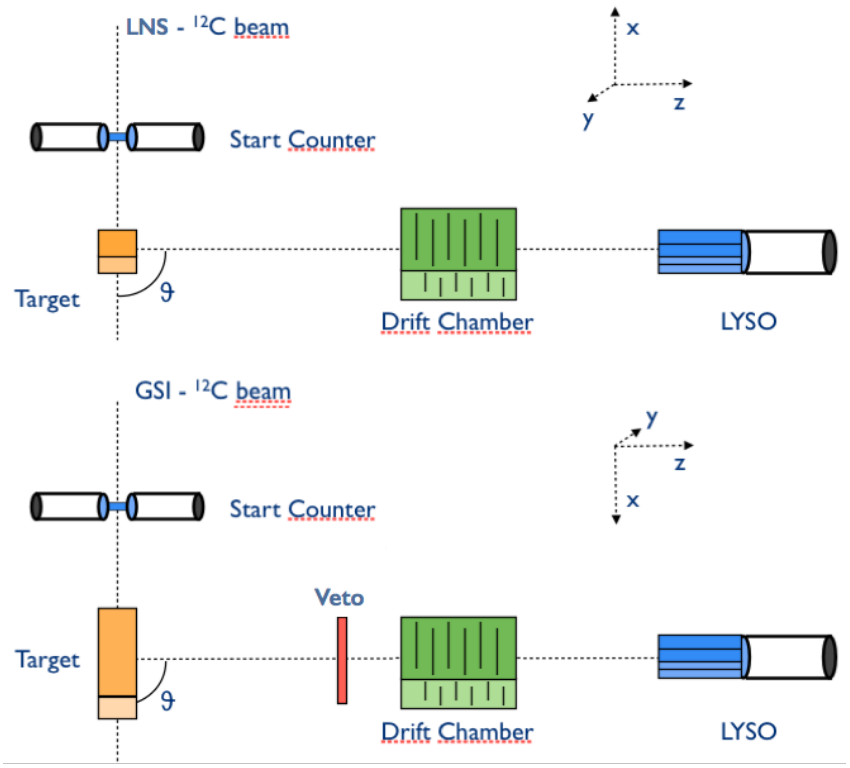

Figure 4.1. Scheme of the experimental setup of the experiments performed at the LNS (top) and GSI (bottom) laboratories. The data acquisition is triggered by the coincidence of the Start Counter and the LYSO crystal. In the GSI data taking the Veto has been included in order to tag events with only neutral particles.

At the Laboratori Nazionali del Sud (LNS) in Catania (Italy), the 80 MeV/u fully stripped ^{12}C beam was impinging on a polymethil methacrylate (PMMA) 4 cm long target with a front area of 4×4 cm^2. Due to the beam range in PMMA of

about ~ 1 cm, the beam stops inside the target.

In the GSI Helmholtz Centre for Heavy Ion Research (GSI) in Darmstadt (Germany), a 220 MeV/u fully stripped ^{12}C beam was impinging on a 20 cm long PMMA target with a front area of 5×5 cm^2. The target size has to be compared with the beam range in PMMA of about ~ 10 cm. A fast plastic scintillator (Start Counter, SC) was placed between the beam exit window and the target, and it has been used as a number of incident primary carbon ions counter. The prompt gammas and secondary charged particles detector was a scintillating crystal of Lutetium and Yttrium Ortho-Silicate doped with Cerium (LYSO). The time coincidence between the SC and the LYSO provided the trigger of both the experiments.
In order to track secondary charged particles, a multi-wire Drift Chamber (DCH) positioned in between the PMMA target and the LYSO calorimeter has been used. The details on neutral and charged detectors will be described in the following subsections. In the GSI experiment a 2 mm thick plastic scintillator (Veto) has been included to tag neutral events.

As shown in the experimental setup figure, the Drift Chamber and the LYSO detector are placed at 90° with respect to the beam direction, aligned to the PMMA center in the LNS experiment and to the expected Bragg peak position at the GSI laboratory. Moreover, in the GSI experiment an angular study at $\theta = 60°$ and 120° has also been performed. The choice of the detection angle θ at which a monitoring detector should be placed with respect to the primary beam direction appears to be crucial in any dose profile monitoring application, as explained in the following subsection.

Detection angle

The prompt gammas emission from nuclear de-excitations is isotropic and therefore the detection angle of a monitor device has a little impact on the monitor performances. On the other hand, for a device exploiting the charged fragments the situation is completely different.

Considering the momentum conservation, the secondary charged particles emission rate is enhanced at small detection angles ($\theta \simeq 0°$). In order to maximize the statistics and to give a prompt measurement of the beam range, a low angle position should be chosen. However, some geometrical and practical aspects related to the operation of a monitor device in a real clinical environment suggest to choose a detection angle in the $60° - 90°$ range.
The back tracking of secondary charged particles to the beam line is needed to reconstruct their emission profile. Such emission distribution suffers from multiple scattering interactions of the track inside the target and from the beam spot size projection on the beam line. This effect is present in both the experiments performed and it is even enhanced in the patient treatment case. The multiple scattering (MS) angle resolution is proportional to the square root of the particle path length inside the target (see equation 1.13), so it is minimized at 90°, while it increases with decreasing particle energy, hence with larger detection angles.

As a consequence of this opposite effect, there is no clear advantage for large or small emission angle as far as the MS is concerned. The situation is very different, however, when the reconstruction accuracy comes into play.

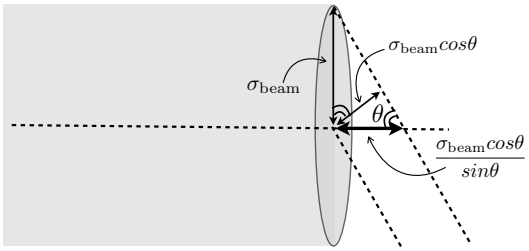

Figure 4.2. Scheme of the beam spot size (grey cylinder) and of its contribution to the reconstruction of the secondary charged particles emission profile with the experimental setup placed at the detection angle θ with respect to the primary beam direction.

Due to the non zero transverse dimension of the hadron beam (σ_{beam}) that can range between ~ 2.5 mm $- 1.5$ cm in clinical practice (depending on the particle, energy and beamline), the uncertainty of the emission point determination has a dependency on the emission angle given by $\sigma = \sigma_{\text{beam}} / \tan(\theta)$, as shown in Figure 4.2. Thus, a large detection angle (as close to 90° as possible) should be preferred.

As last consideration, in view of an actual clinical application, very often the positions at low θ are not available to a monitor device, in particular in the treatment configuration where the patient body is aligned with the beam axis.
In the following subsections the setup elements will be reviewed as well as the Data Acquisition chain.

4.1.1 Start Counter

The 1.1 mm thick Start Counter is a thin plastic scintillator (BC-404), read out by two opposite Hamamatsu H10580 photomultiplier tubes (PMTs). Placed on the beam line, between the beam exit window and the target, the Start Counter is used for the Time of Flight (ToF) measurements of secondary neutral and charged particles and as a primary beam ions counter. The OR of the two PMT signals is used in order to increase the detection efficiency of the SC.

4.1.2 LYSO

Two similar calorimeters, made by a 2×2 matrix of $1.5 \times 1.5 \times 12$ cm^3 LYSO crystals, read out by one photomultiplier (EMI 9814B), have been used in the LNS and GSI experiments. Table 4.1 reports some LYSO properties. Used primarily as prompt photons detector, it has been chosen for its fast time response (decay constant $\tau \sim 42$ ns) in order to discriminate the prompt photons signal from neutrons background. Moreover, the LYSO high density allows for a compact detector, while its high light output response increases its energy resolution. The PMMA-LYSO distance (d) has been computed between the PMMA center and the LYSO front face at the LNS laboratory and between the expected Bragg peak position in the PMMA and the LYSO front face at GSI. The measured distances are $d \sim 74$ cm and $d \sim 65.8$ cm at the LNS and GSI laboratories, respectively.

LYSO Characteristics	
Effective Atomic Number	66
Density (g/cm^3)	7.4
Radiation Length (cm)	1.10
Decay Constant (ns)	$40 - 44$
Peak Emission (nm)	428
Light Yield % NaI (Tl)	75
Index of Refraction	1.82

Table 4.1. Properties of LYSO crystals.

LYSO calibration

In order to fully characterize the prompt photons emission, that will be described in Section 4.3, a detailed calibration of the two LYSO calorimeters in the energy range of interest ($1 \div 10$ MeV) has been performed (*Bellini et al.* [55]).
To obtain such calibrations on an extended gamma energy range ($1-10$ MeV) several radioactive sources have been used in an original and new method proposed in this work. The sources are the ^{22}Na and ^{60}Co radioactive sources (giving the gamma lines at 0.511 MeV and 1.17 MeV, 1.33 MeV respectively) and an AmBe source. An indirect production mechanism has been implemented by the use of AmBe in order to obtain "high" energy gamma lines: since the AmBe source produces $\sim 2.5 \times 10^6$ $neutrons/s$, the source was hosted inside a 5 cm thick paraffin container ($C_{31}H_{62}$) to moderate the neutron flux (and not saturate the detector) and to produce two high energy gamma lines. The neutron-hydrogen interaction produces the 2.22 MeV gamma line from deuteron formation, while the neutron-carbon interaction produces the 4.44 MeV $^{12}C^*$ de-excitation line.

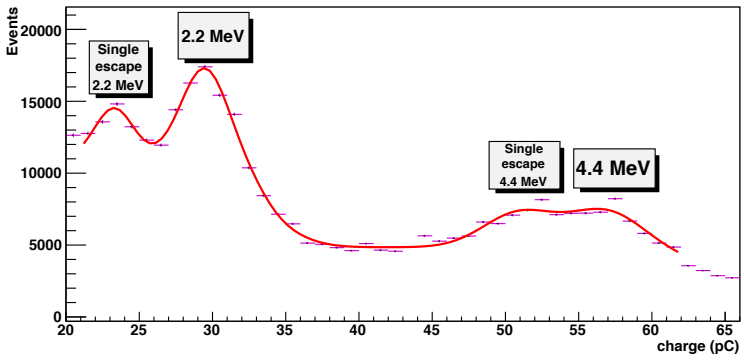

Figure 4.3. LNS LYSO energy spectrum obtained with an AmBe source moderated with paraffin.

Figure 4.3 shows the measured spectrum with the LNS LYSO detector where the two mentioned gamma lines are visible as well as the single escape peaks occurring when a 0.511 MeV photon produced from the electron-positron annihilation escapes the detector volume.

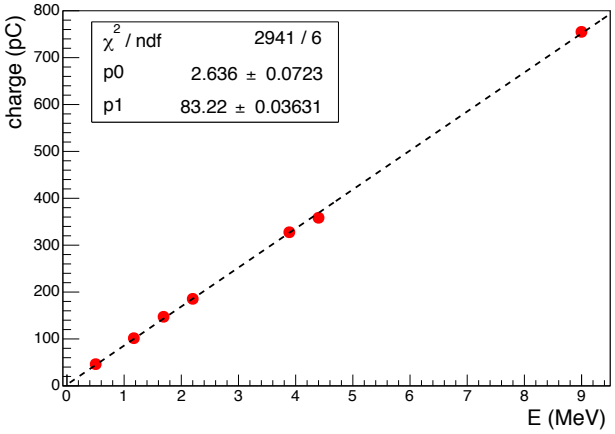

Figure 4.4. LNS LYSO detector linear calibration curve (black dashed line) obtained combining the ^{22}Na and ^{60}Co gamma lines together with the AmBe data (red dots).

In order to have an additional line for calibration, a rod of nickel 2 mm thick has been inserted between the AmBe source and the LYSO detector. A set of high energy lines centered around 8.8 MeV has been obtained. The derived calibration curve is:

$$charge = p_0 + p_1 \cdot E \tag{4.1}$$

with p_0 and p_1 shown in Figure 4.4 for the LYSO used at LNS. From the fit to the spectrum in Figure 4.3 also the detector energy resolution as a function of the deposited energy has been obtained. This information is needed as input to the simulation that will be described in Section 4.2. The result for the LNS detector is shown in Figure 4.5, where the dependence is fitted with the following equation:

$$\frac{\sigma(E)}{E} = \sqrt{p_0^2 + \frac{p_1^2}{E} + \frac{p_2^2}{E^2}} \ . \tag{4.2}$$

For the LNS LYSO crystals it has been obtained: the constant term $p_0 = (3.700 \pm 0.007) \cdot 10^{-2}$, the statistical term $p_1 = (0.0579 \pm 0.0006)$ MeV$^{\frac{1}{2}}$ and the electronic term p_2 consistent with zero.

The same study has been performed for the LYSO detector employed in the GSI experiment. The obtained linear calibration from equation 4.1 has the following parameters:

$$p_0 = (-9.65 \pm 0.05) \text{ pC} \quad , \quad p_1 = (47.79 \pm 0.04) \text{ pC/MeV} \ . \tag{4.3}$$

The energy resolution of the GSI LYSO detector has the same behaviour of the one of the LNS LYSO detector and it has been described by the same fit function in equation 4.2. The obtained parameters for the GSI LYSO calorimeter energy resolution are the following: the constant term $p_0 = (-1.6 \pm 0.3) \cdot 10^{-4}$, the statistical term p_1 is consistent with zero, the electronic term $p_2 = (-0.078 \pm 0.003)$ MeV.

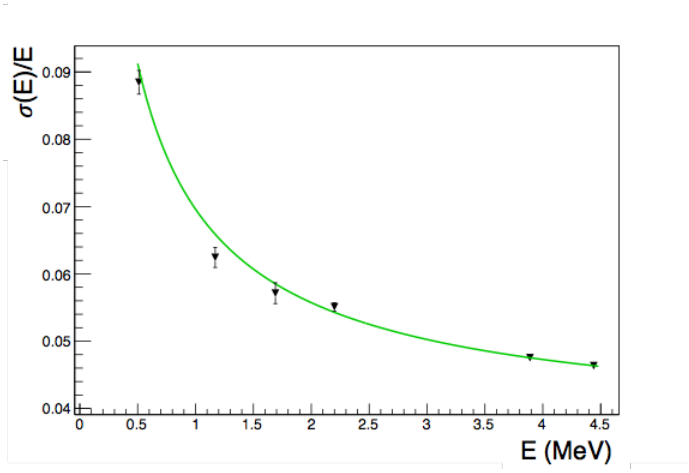

Figure 4.5. LNS LYSO detector resolution as a function of the deposited energy. The fit function described in equation 4.2 is superimposed.

4.1.3 Drift Chamber

A multi-wire Drift Chamber has been used to detect and track secondary charged particles. Drift chambers are devices used in high-energy physics experiments to measure properties of subatomic particles. Drift chambers are filled with a gas mixture (usually argon and carbon dioxin or isobutane) and thousands of wires at high electrical potential. When a charged particle passes through this device, it ionizes the gas atoms. The ionization electrons *drift* to the *sense wire* and are multiplied by the intense electric field near the wire. Such electron cascade is collected on the wire, giving an electric current proportional to the energy loss of the detected particle. A picture of a DCH is given in Figure 4.6.

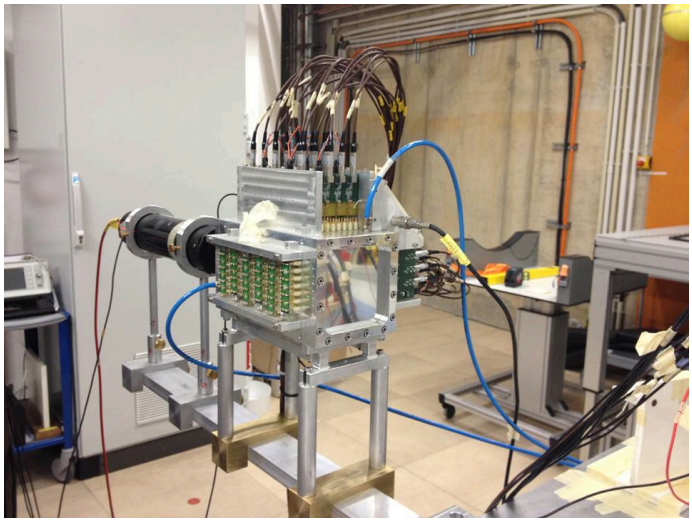

Figure 4.6. Picture of the multi-wire drift chamber used in the LNS and GSI experiments.

Suitable electronic signal processing is then used to determine the position and direction of the crossing particles. Although the wires may be centimeter apart, the position of a particle can be determined with an accuracy of hundred microns.
Using this detector it is possible to reconstruct the emission region profile of the traversing particle back pointing the detected charged tracks to the beam line. An example of a reconstructed track using a multi-wire DCH is shown in Figure 4.7. It has to be taken into account that when secondary charged particles are backtracked, some intrinsic limitations on the reconstructed emission distribution have to be considered, since charged particles suffer from multiple scattering inside the target and the primary charged beam has a non negligible extension (like a cylinder with a diameter of ~ 1 cm). Therefore, the reconstruction of secondary fragments emission distribution has an intrinsic uncertainty of the order of some millimeters. The very efficient and fast response drift chamber is hence a perfect low cost charged particle detector for the aim of the measurements described in this work.

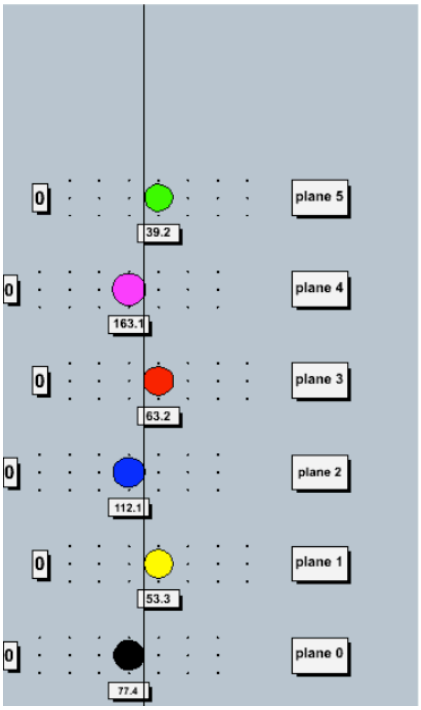

Figure 4.7. Event display of a multi-wire drift chamber showing the reconstructed track (straight line) of a secondary charged particle.

The DCH used in the LNS and GSI experiments is made of 12 planes, 6 planes for the horizontal view (U) and 6 planes for the vertical view (V), and each plane has three sense wires (cells). A schematic view of the Drift Chamber is shown in Figure 4.8. The DCH is filled with an Ar/CO_2 $80\% - 20\%$ gas mixture and its performances have been studied by *Abou-Haidar et al.* [64], that had used the same Drift Chamber as a beam monitor in the FIRST experiment at GSI (*Pleskac et al.* [6]). The single cell efficiency is $\epsilon_{DCH} = (93 \pm 3)\%$ and the measured single cell spatial average resolution is $\sigma_{DCH} = 180$ µm. These values have been obtained by

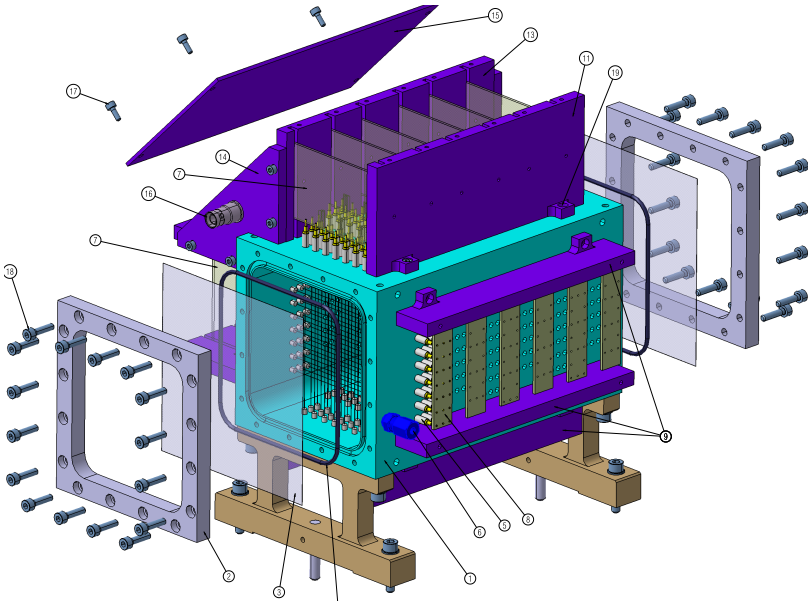

(a)

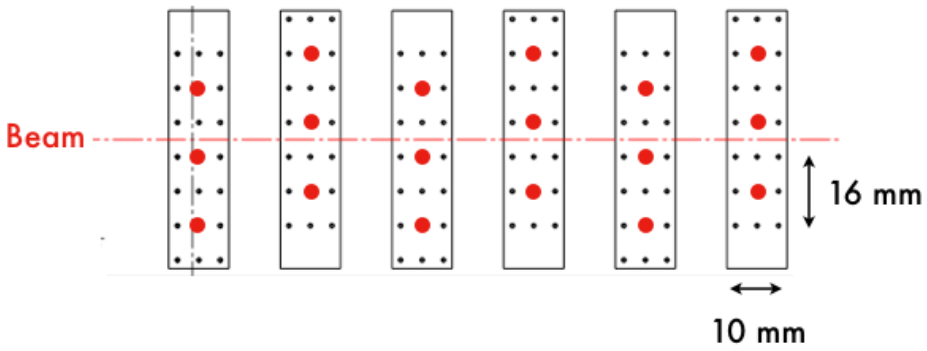

(b)

Figure 4.8. a) Scheme of the Drift Chamber mechanics. b) Drift Chamber lateral layout; the red dots show the sense wires.

some dedicated studies on the Drift Chamber efficiency as a function of the high voltage and on the DCH spatial resolution as a function of the track distance from the sense wire, shown in Figure 4.9 and Figure 4.10 respectively.

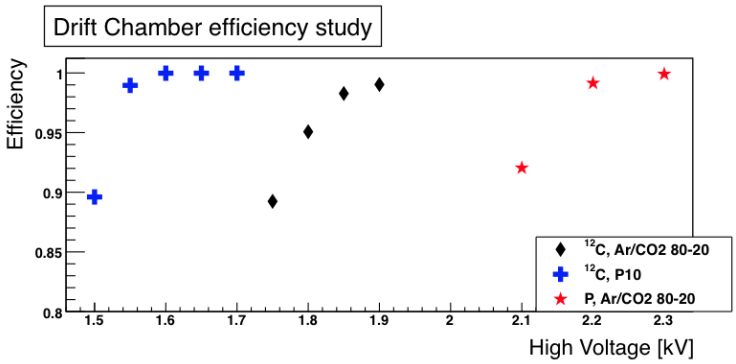

Figure 4.9. Drift Chamber efficiency study performed at LNS with different gas mixtures and ionizing particles as a function of the Drift Chamber high voltage. The blue dots show 80 MeV/u ^{12}C ions in $P10$ (10% Methane in Argon), while the black dots show the same ionizing particles in $Ar/CO2$ $80\% - 20\%$. The red dots indicate 80 MeV protons in $Ar/CO2$ $80\% - 20\%$.

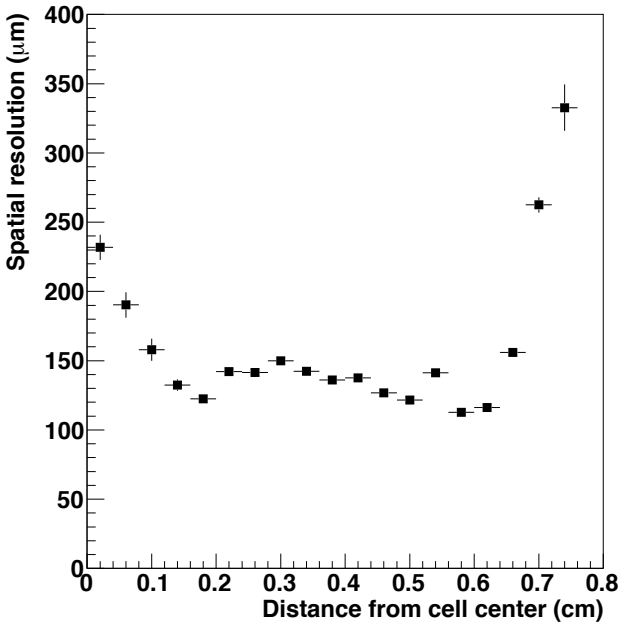

Figure 4.10. Drift Chamber spatial resolution as a function of the track distance from the cell center.

4.1.4 Data Acquisition

A scheme of the Data Acquisition system is shown in Figure 4.11. SC0 and SC1 are the signals from the two opposite PMTs reading the Start Counter, while LYSO is the signal from the LYSO calorimeter. Both charge and arrival time of primary ion beam and of secondary particles are recorded by an ADC and TDC module, respectively.

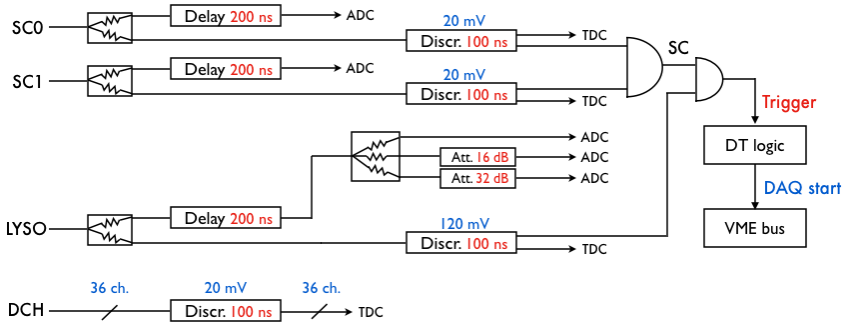

Figure 4.11. Scheme of the DAQ flow chart.

The LYSO charge has been splitted in three, and then two signals have been attenuated by different values in order to ensure a large detection energy range of secondary particles for the subsequent data analysis (we are interested to both low energy prompt gamma signals starting around 1 MeV and secondary charged particle signals that end up at 150 MeV). The time coincidence between SC0 and SC1 forms the SC signal, giving the DAQ Trigger in coincidence with the LYSO signal. This signal starts both a busy signal propagated to all the electronics and the data acquisition itself. The arrival time of ionization electrons on the sense wires of the DCH are recorded in the corresponding 36 read out channels in the TDC.

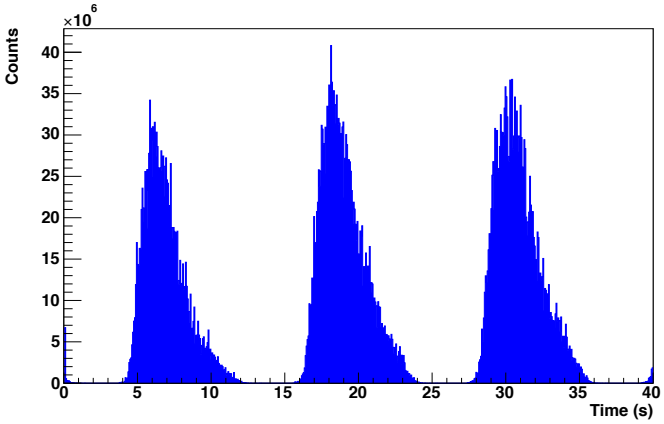

Figure 4.12. Bunched structure of the GSI carbon beam.

While at LNS the beam was provided by a cyclotron and therefore had a continuous time structure, at GSI the beam was given by a synchrotron, with a corresponding bunched time structure. The beam rate for both data taking was of the order of megahertz. An example of the beam structure in the GSI experiment is shown in Figure 4.12. During a "spill", when the accelerated particles are actually "spilled" out of the accelerator, hadrons are not uniformly distributed, as can be observed by the triangular structure of the spill. The GSI spill duration time is ~ 7 s, while the time interval between to consequent spills is ~ 11 s.
The beam rate is computed with the Start Counter and primary particle rates up to 10 MHz can be sustained by the SC scintillator. The trigger rate was in the range between $\sim 1-2$ kHz and $\sim 1-5$ kHz at the LNS and GSI experiments, respectively. However, the Dead Time inefficiency is expected to be not negligible in both data taking, as it will be discussed in the next sections.

4.2 FLUKA Simulation

Since we are interested in exploiting the secondary prompt gamma and charged radiations, a study with the Monte Carlo (MC) FLUKA code has been performed in order to assess what to expect from an 80 MeV/u and a 220 MeV/u carbon ion beams interacting with a PMMA target at the LNS and GSI experiments, respectively.
FLUKA is a general purpose tool for calculations of particle transport and interactions with matter (*Ferrari et al.* [7], *Böhlen* et al. [65]). It is used in many applications such as, for example, proton and electron accelerator shielding, target design, calorimetry, activation, dosimetry, detector design, cosmic rays and radiotherapy. It can simulate a large number of different particles (about 60) covering a wide energy range (from keV to TeV). Whenever it is possible, microscopic models are adopted and the consistency among all the reaction steps and/or reaction types is ensured, as well as the conservation laws. As a result, final predictions can be obtained with a minimal set of free parameters fixed for all energy/target/projectile combinations. Moreover, FLUKA is able to build very complex geometries, using a combinatorial geometry package that allows also to track charged particles in presence of electric or magnetic fields and many visualization and debugging tools are available for the user, without requiring any programming ability. Although, if the user has any special requirement and need to control each step of the simulation, the software is fully customizable via a set of user interface routines (written in Fortran 77). A list of physical models used in a FLUKA simulation is here reported, and almost all the FLUKA interaction models are coded by different packages, specific for two or more energy ranges: hadron inelastic nuclear interactions, elastic scattering, nucleus-nucleus interactions, transport of charged hadrons and muons, low energy neutrons, electrons, photons, optical photons and neutrinos.

The simulations performed for the LNS and GSI experiments used some customized routines in order to tailor the output data to the actual DAQ output. In particular, a general track database has been built to store some fundamental information about all the created particles in each event such as the particle generation (initial i) and death (final f) position $(x, y, z)_{\mathrm{i,f}}$, momentum $(p_x, p_y, p_z)_{\mathrm{i,f}}$, the current particle identity (if, for example, it is a photon, an electron, other particle), the identity of its

parent, the time of generation and so on. For each detector of the total experimental geometry, the released energy at each step has also been stored. Quenching effect inside scintillators has been taken into account according to *Koba et al.* [66]. Finally, a library that interfaces FLUKA to ROOT (*Brun and Rademakers* [67]), a commonly used data analysis framework for high energy physics, has been built.

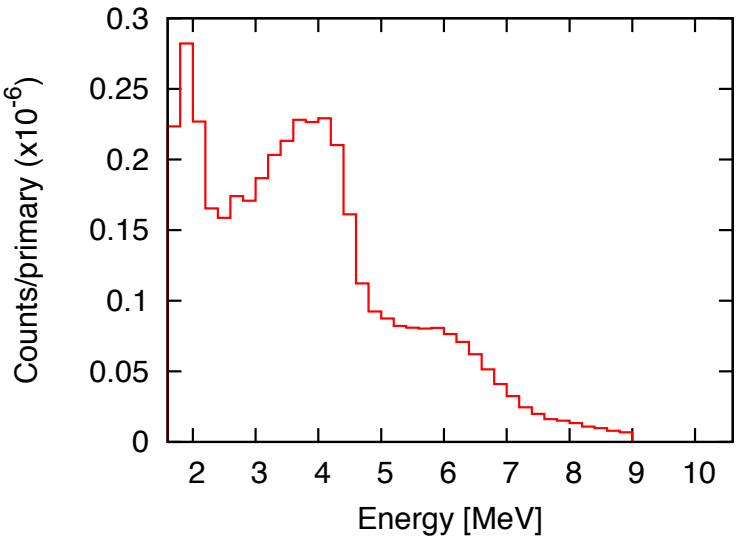

Figure 4.13. Distribution of the simulated production energy spectrum of prompt gammas emitted in the interaction of an 80 MeV/u ^{12}C beam with a PMMA target, detected by a LYSO scintillator placed at 90° with respect to the beam direction.

The experimental setup shown in Figure 4.1 has been simulated with FLUKA in order to reproduce the LNS and GSI experiments. The experimental aluminum table that sustained all the setup components has also been reproduced, as well as the DCH compounding materials and electronics, in order to take into account also the scattering interactions of secondary particles due to such elements.

To assess what to expect by the LNS experiment about the prompt gamma radiation measurements, an 80 MeV/u carbon ions cylindrical beam has been simulated. The neutral radiation has been collected by the LYSO detector placed at 90° with respect to the PMMA position. In order to increase the collected particles statistics, the LYSO detector is virtually replicated in a ring centered in the target, with the axis parallel to the beam, since the distribution of prompt photons is practically isotropic. The energy deposition in the replicas is summed up to obtain the gamma energy spectra (the detector replication is taken into account when normalizing to data statistics). Counts in the scintillator are recorded with a DETECT card, which scores the energy deposition on an event by event basis. The scored counts are then folded with the measured intrinsic energy resolution of the LYSO crystal (see Section 4.1.2). In order to obtain the prompt gammas energy spectrum, the true measured prompt gamma energy distribution has been normalized to the true number of primary carbon ions simulated ($6 \cdot 10^8$). The obtained production energy spectrum is shown in Figure 4.13.

For the secondary charged particles measurements, the FLUKA simulation provides also the Drift Chamber information. For the GSI experiment, a 220 MeV/u ^{12}C cylindrical beam has been simulated and the geometry of the experimental setup has been slightly changed with respect to the one used for the LNS experiment. In both LNS and GSI simulations, the informations about the secondary charged particle Time of Flight (ToF) from the PMMA to the LYSO detector and the deposited energy in the LYSO crystals (E_{LYSO}) have been exploited to guide the particle identification in data (see Section 4.4.1). The bi-dimensional distributions E_{LYSO}-ToF for the LNS (left) and GSI (right) experiments are shown in Figure 4.14.

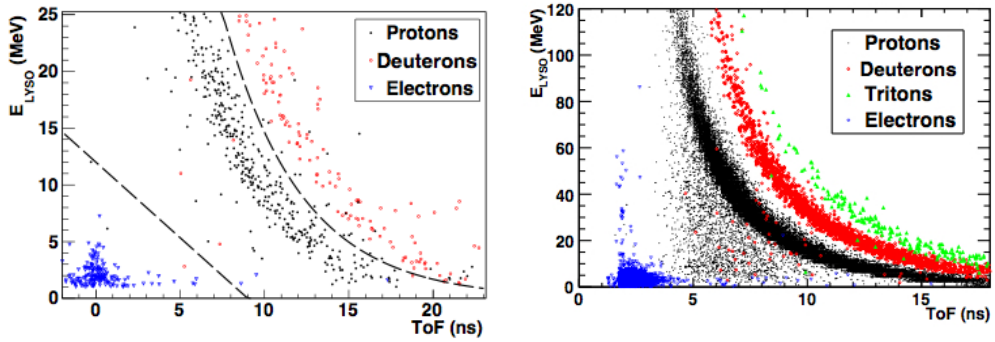

Figure 4.14. LNS (left) and GSI (right) Monte Carlo simulated distributions of the released energy in the LYSO detector (E_{LYSO}) as a function of the Time of Flight (ToF) for the 90° setup.

In the E_{LYSO}-ToF LNS distribution, the ToF has been computed as the time difference between the interaction time in the LYSO detector and the primary ion interaction time in the Start Counter, as performed for the measured data. Instead, for the E_{LYSO}-ToF GSI distribution, in the ToF calculation the time of propagation of the primary beam within the PMMA has been taken into account and properly subtracted, as well as in the GSI data analysis. As expected, the deposited energy in the LYSO scintillator reaches higher values for the GSI distribution, and the triton population appears, as the primary carbon ions energy is much higher for the GSI experiment than for the LNS experiment.
Some dedicated FLUKA simulations have also been performed in order to compute some efficiencies for the production rates calculation, as well as the secondary charged particles velocity distributions in the GSI experiment, as it will be described in the next sections.

4.3 Prompt Photons Measurements

In this section, the measurements of prompt gammas produced in the interaction of an 80 MeV/u ^{12}C beam with a PMMA target are shown. The experimental setup is sketched in Figure 4.1 (top). Some preliminary results from the 220 MeV/u GSI ^{12}C beam impinging on a PMMA are also reported, as well as the ongoing analysis from the data taking performed at the Heidelberg Ion Therapy center (HIT), in Heidelberg, Germany.

4.3.1 Energy spectrum

The prompt gammas energy spectrum has been obtained from the charge and time measurements, using the LYSO detector energy calibration described in Section 4.1.2 (see Figure 4.4).

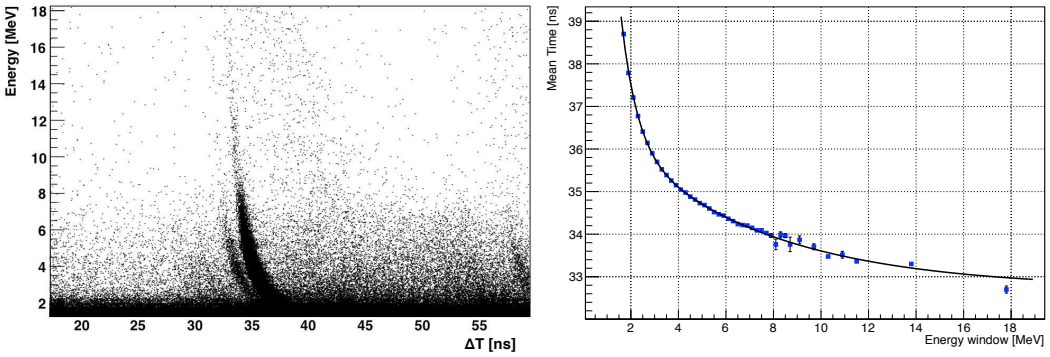

Figure 4.15. Left: Calibrated energy released in the LYSO crystal as a function of the arrival time ΔT. Four components are present: an horizontal band due to the LYSO intrinsic noise; two almost vertical band due to the signal from the prompt photons coming from the target (the slower one) and from the Start Counter; a diffused cloud mainly due to neutrons at ΔT values larger than those of the prompt photons population. Right: estimated time slewing correction.

The information on the time difference (ΔT) between the energy deposition time in the LYSO and the primary carbon ion interaction time in the Start Counter has been used for the selection of a prompt photon event. Figure 4.15 (left) shows the correlation between the reconstructed calibrated energy and the measured ΔT. Four distinct regions can be observed: an horizontal flat band due to the LYSO intrinsic background noise; the main prompt photons population coming from the target and a faster component of prompt photons (due to the shorter path length) produced in the Start Counter and arriving directly on the LYSO; a diffused cloud mainly due to neutrons not correlated with the prompt photons radiation.

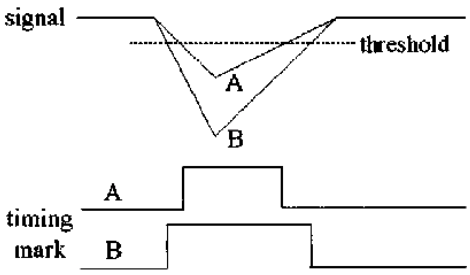

Figure 4.16. Time slewing effect: signals produced at the same time with different amplitudes surpass the front-end electronics fixed voltage threshold at different times.

The shape of the prompt photons signal is not a vertical band as expected, due to the time slewing effect induced by the front-end electronics fixed voltage threshold: two signals produced at the same time with different amplitudes cross the voltage threshold at different times (see Figure 4.16).

The time slewing effect can be corrected by fitting the ΔT distributions in bins of Energy, thus obtaining the correction function $C(E)$, shown in Figure 4.15 (right).

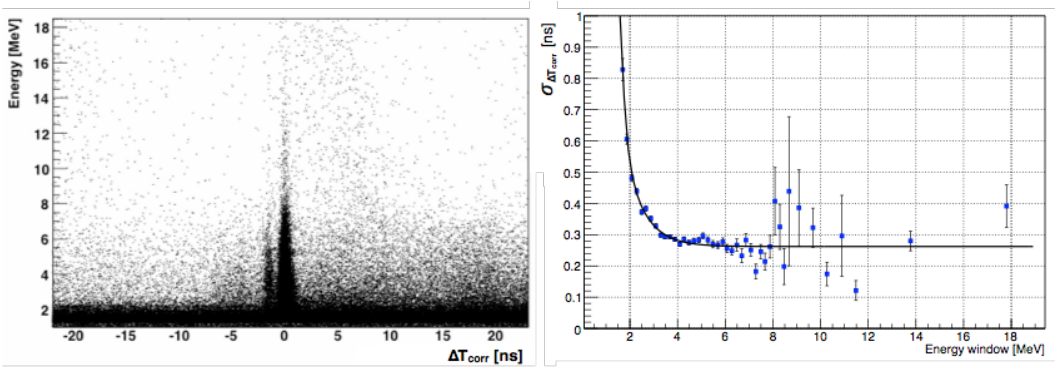

Figure 4.17. Left: calibrated energy released in the LYSO crystal as a function of the arrival time corrected taking into account the slewing effect. Right: measured time resolution as a function of the calibrated energy.

The energy spectrum as a function of the corrected time

$$\Delta T_{corr} = \Delta T - C(E) \tag{4.4}$$

is shown in Fig. 4.17 (left) while the detector time resolution $\sigma_{\Delta t}$ as a function of the energy is shown in Fig. 4.17 (right). For energies greater than 3 MeV, an average time resolution of 270 ps has been achieved.

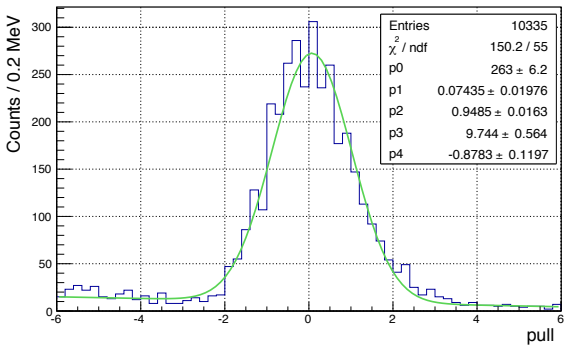

Figure 4.18. Example of a pull distribution in a specific energy bin and the corresponding fit function (green line) described in equation 4.6. The fit parameters are shown.

In order to measure the prompt gammas energy spectrum, the number of prompt photons in each energy bin has been measured from the fit to the *pull* distribution

$$pull = \Delta T_{corr}/\sigma_{\Delta T_{corr}} \tag{4.5}$$

in that bin (see Fig. 4.18).
The fit function (the green line in Figure 4.18) is described by the following relation:

$$f(x) = p_0 \; exp\left(-\frac{(x-p_1)^2}{2\;p_2^2}\right) + p_3 + p_4 \; x \; . \tag{4.6}$$

f(x) is a superimposition of a Gaussian function describing the signal, while the background is described by a polynomial function. The area under the Gaussian function is the prompt photons number in a given energy bin.

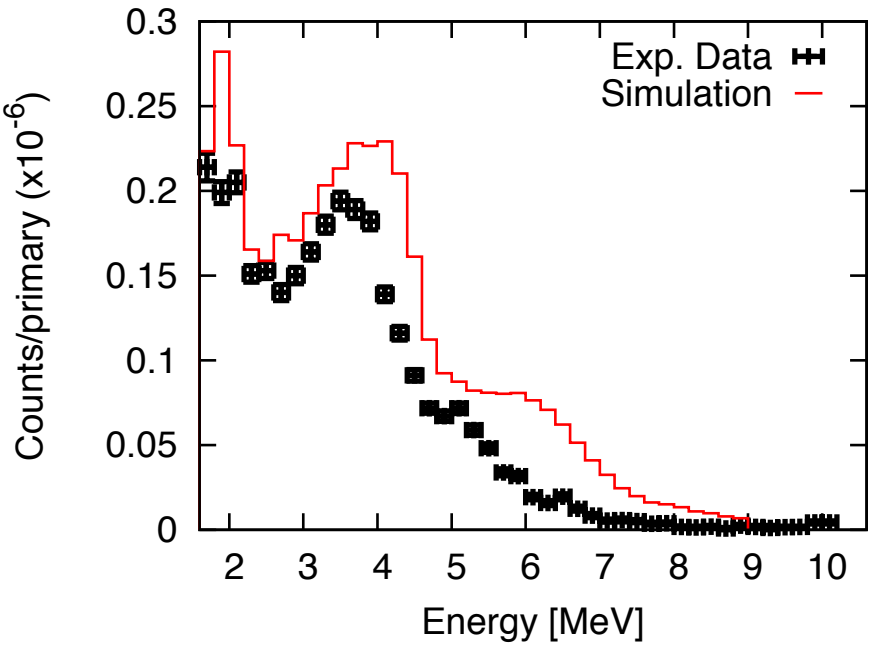

Figure 4.19. Measured prompt photons energy spectrum at production (black dots), compared to the FLUKA simulation (red solid line).

Figure 4.19 shows the measured prompt photons energy spectrum (black dots), normalized to the number of incident carbon ions N_{C} and corrected for the DAQ dead time inefficiency ϵ_{DT}. The dead-time inefficiency ϵ_{DT} has been estimated from the total acquisition time (T_{dead}) and the total run time (T_{tot}) as:

$$\epsilon_{\mathrm{DT}} = 1 - \frac{T_{dead}}{T_{tot}} \; . \tag{4.7}$$

The measured value of ϵ_{DT} ranges from 70% at an average carbon ion rate of 0.6 MHz up to 47% at an average carbon ion rate of 2 MHz.

The number of carbon ions N_{C} reaching the PMMA in a given time interval is evaluated by counting the number of signals given by the Start Counter (N_{SC}) within randomly-triggered time-windows of $T_w = 2$ µs. The number of the impinging carbon ions is then estimated as:

$$N_{\mathrm{C}} = \frac{N_{\mathrm{SC}}}{\epsilon_{\mathrm{SC}}} \frac{T_{tot}}{N_w * T_w} \tag{4.8}$$

with N_w the number of time windows considered and $\epsilon_{\mathrm{SC}} = (96 \pm 1)\%$ the Start Counter efficiency. The SC efficiency has been estimated by exploiting the two-sided PMT readout with negligible dark counts:

$$\epsilon_{\mathrm{SC}} = \epsilon_{\mathrm{sc1}} \cdot \epsilon_{\mathrm{sc2}} = \frac{N_{12}^2}{N_1 \cdot N_2} \tag{4.9}$$

where $N_{1,2}$ are the single PMT counts and N_{12} their coincidences.

The measured energy spectrum in Figure 4.19, obtained by the measured raw photons counts normalized to N_{C} and ϵ_{DT}, is compared to the simulated spectrum (red solid line), that has been already shown in Figure 4.13. As aforementioned, the simulated energy spectrum has been obtained by the simulated prompt photons counts folded with the measured intrinsic energy resolution of the LYSO crystal (see Section 4.1.2) and normalized to the simulated carbon ions number. Since in the simulation the LYSO detector is a ring replication centered in the target in order to increase the collected statistics considering an isotropic prompt photons emission distribution, the simulated energy spectrum has been normalized to data statistics in order to take into account the experimental geometry (for further details see *Agodi et al.* [53] [54] and *Bellini et al.* [55]). The main structure in Figure 4.19 is at ~ 4 MeV and it is due to the $^{12}C^*$, $^{11}C^*$ and $^{11}B^*$ target and projectile nuclei de-excitation lines, mixed as a consequence of the detector energy resolution.

A data-Monte Carlo agreement on the energy spectra shape and normalization is visible. Nuclear cross sections modeling and investigations on possible systematic effects are ongoing.

4.3.2 Production Rate

The γ prompt production rate in principle could assess the possibility of using such secondary radiation for the dose monitoring purpose and the achievable resolution of the technique.
To this aim, only prompt photons with a measured energy $E > 2$ MeV have been selected, in order to reject the LYSO intrinsic radioactivity background and low energy neutron background. For such events, the prompt photon fraction (F_{prompt}) has been evaluated as the ratio of the prompt photon and carbon ion rates (R_{prompt} and R_C respectively), as shown in the following equation:

$$F_{prompt} = \frac{R_{prompt}}{R_C} = \frac{N_\gamma}{\epsilon_{\mathrm{DT}} \epsilon_{\mathrm{SC}} N_{\mathrm{C}}} \ . \tag{4.10}$$

The number of measured prompt photons N_γ has been obtained from a side-band subtraction of the prompt photon fitted $\Delta T_{corr}/\sigma_{\Delta T_{corr}}$ distribution (see Figure 4.18). ϵ_{DT}, N_{C} and ϵ_{SC} are described in equation 4.7, 4.8 and 4.9 respectively.

Fig. 4.20 shows that F_{prompt} is not dependent on the carbon ion rate. The average value obtained for F_{prompt} is:

$$F_{prompt} = (3.04 \pm 0.01_{stat} \pm 0.20_{sys}) \times 10^{-6} \tag{4.11}$$

with the systematic error introduced in order to account for the dispersion of the values which is well above the statistical fluctuations. Under the hypothesis of a flat distribution, the systematic error was estimated as the semi-dispersion divided by $\sqrt{3}$ (as for the uniform distribution uncertainty).

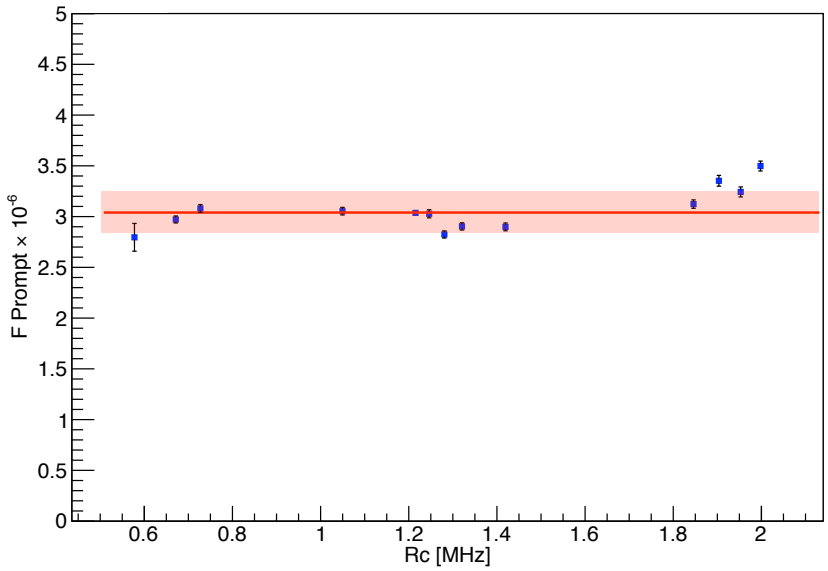

Figure 4.20. Fraction of prompt photons with $E > 2$ MeV as a function of the carbon ion rate. The red fit line is shown with the error band (both statistical and systematic errors are taken into account).

The integrated rate of prompt photons with energy $E > 2$ MeV normalized to the solid angle is evaluated as:

$$\Phi^{\gamma}(\Omega_{\mathrm{LYSO}})_{E>2\mathrm{MeV},\theta=90^{\circ}} = \frac{F_{prompt}}{\epsilon_{LYSO}\Omega_{LYSO}} \tag{4.12}$$

with $\Omega_{LYSO} \sim 1.6\times10^{-3}$ sr the LYSO detector solid angle and $\epsilon_{LYSO} = (81.3\pm2.5)\%$ the LYSO detection efficiency estimated with a dedicated FLUKA simulation.

In summary, for the experimental setup described in Section 4.1, with a primary 80 MeV/u carbon ion beam impinging on a PMMA target, the obtained prompt

photons production rate is:

$$\Phi^{\gamma}(\Omega_{\mathrm{LYSO}})_{E>2\mathrm{MeV},\theta=90^{\circ}} = (2.32 \pm 0.01_{stat} \pm 0.15_{sys}) \times 10^{-3}\ sr^{-1}\ . \qquad (4.13)$$

4.3.3 Preliminary data from 220 MeV/u ^{12}C ion beam

A study on the prompt gamma radiation has been performed also in the GSI experiment, with a 220 MeV/u carbon ion beam impinging on a PMMA target, in the setup configuration at 60°, 90° and 120°. The experimental setup is outlined in Section 4.1. In order to obtain the prompt photons energy spectrum and rate, a similar procedure as the one described in Section 4.3.1 and 4.3.2, respectively, has been followed.

Prompt photon energy spectra

The bi-dimensional distribution of the deposited energy in the LYSO crystal (E_{LYSO}) versus ΔT_{corr}, defined in equation 4.4 (with a specific correction $C(E)$ for the GSI data) has been used in order to separate prompt photons from neutrons and other secondary particles.

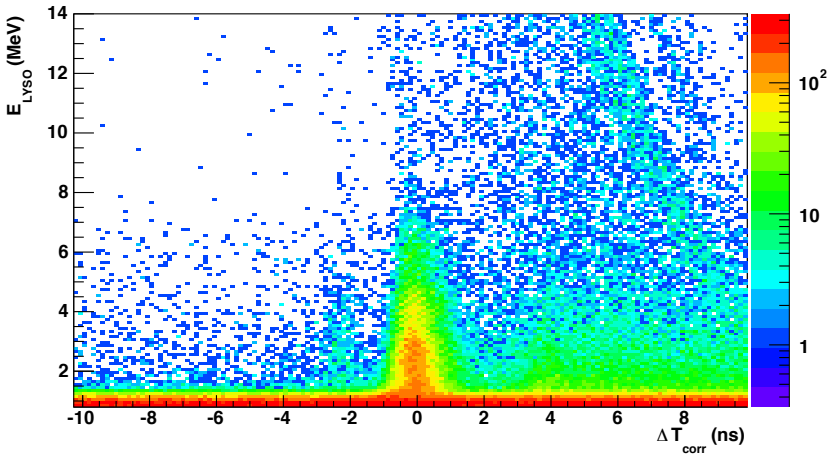

Figure 4.21. Prompt gamma energy deposition in the LYSO crystals (E_{LYSO}) as a function of the arrival time on the LYSO detector corrected for the time slewing effect (ΔT_{corr}).

The $E_{\mathrm{LYSO}} - \Delta T_{\mathrm{corr}}$ distribution is shown in Figure 4.21 for a data sample in the angular configuration at 90°. The horizontal, low energy band is due to the LYSO intrinsic noise, the prompt gamma signal is the vertical band around 0 ns, while the diffused cloud is mainly due to neutrons. In order to measure the energy spectrum of prompt photons produced within the PMMA target, the number of reconstructed prompt photons (N_{γ}^{rec}) detected with the LYSO crystals has to be evaluated, and unfolded for the detector efficiency and resolution effects to obtain the number of photons (N_{γ}) produced in the ^{12}C interactions with the target nuclei. The number of reconstructed prompt photons has been computed from the time pull distribution sampled in released, 0.1 MeV wide, energy bins (see equation 4.5 for the *pull* variable description). N_{γ}^{rec} in each energy bin has been obtained from an unbinned maximum likelihood fit, using the RooFit package from ROOT (*Verkerke and Kirby* [68]). A

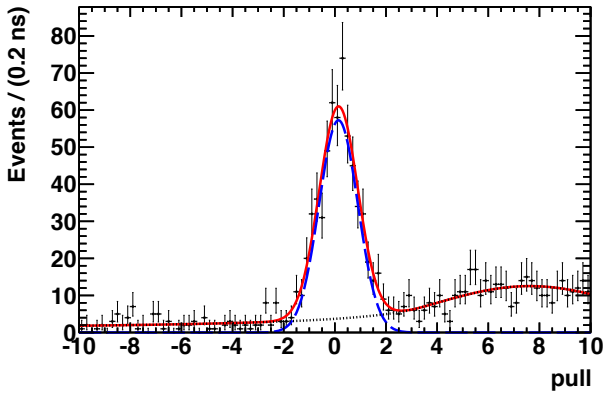

Figure 4.22. Example of the time pull distribution in one energy bin. The red solid line is the total fit function: the blue dashed line indicates the gaussian fit to the signal, while the black dotted line is the Crystal Ball function that fit the neutron background.

sample pull distribution in one energy bin (1.5 MeV $< E_{\mathrm{LYSO}} <$ 1.6 MeV) is shown in Figure 4.22 for a run in the experimental setup configuration at 90°. The prompt gamma signal is modeled by a gaussian probability density function (PDF, blue dashed line), while the neutron background is described by a Crystal Ball function (black dotted line). The red solid line represents the total PDF. The obtained raw energy spectra measured in the different angular configurations are shown in Figure 4.23.

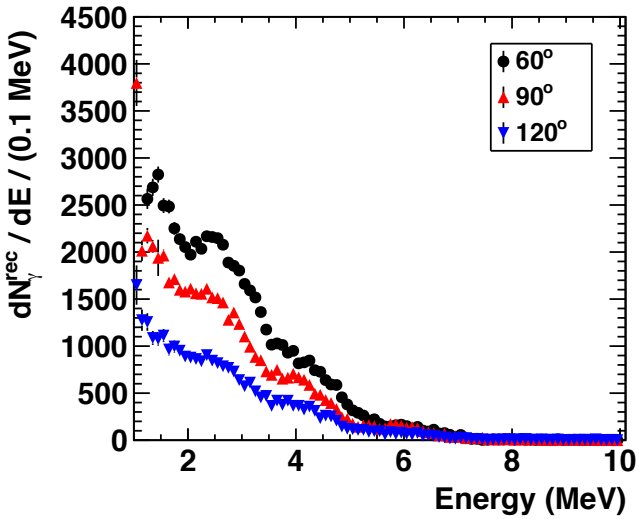

Figure 4.23. Raw energy spectra of prompt photons detected by the LYSO scintillator at 60°, 90° and 120°, corrected for the DAQ dead time inefficiency.

For each angular configuration, the raw spectrum is the sum of different data acquisitions collected with different carbon ion rates and so with different DAQ dead time. Therefore, in order to sum different samples at the same angular configuration, each data taking has been corrected for its proper dead time inefficiency (for the dead time inefficiency computation see details about equation 4.14).

In order to unfold the detector effects from the number of reconstructed photons, obtaining the number of prompt photons N_γ at production, an unfolding algorithm has been used. This procedure is necessary to take into account the detection efficiency, the detector resolution, and the fraction of the detected events that are due to neutral particles scattered by the materials surrounding the LYSO crystals.

The method has been tested on the full FLUKA Monte Carlo simulation of the ^{12}C ion beam impinging on the PMMA, reproducing the geometric and physical characteristics of all the experimental setup components. The algorithm, implemented in the ROOT software as TUnfold package, allowed to compute the production energy spectrum of the reconstructed photons.

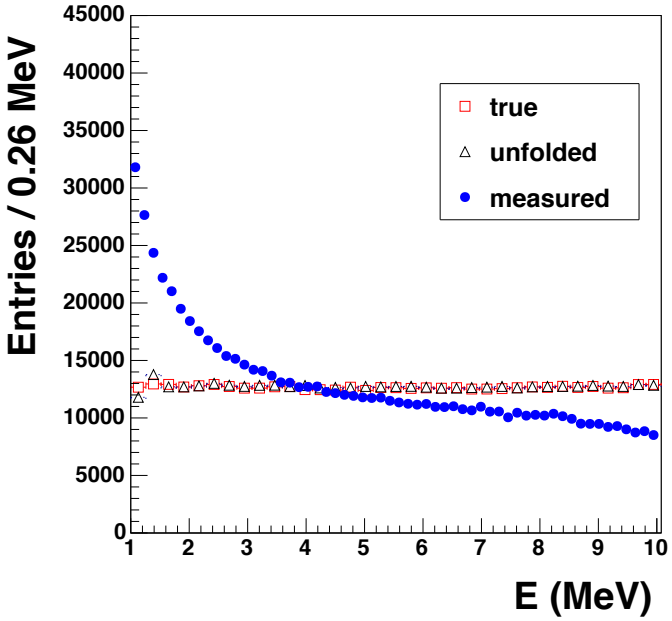

Figure 4.24. Unfolding test. The measured spectrum (blue circles) from the *FLAT* simulation has been unfolded, and the unfolded spectrum (black triangles) has been compared to the true production energy spectrum (red squares). The agreement between the unfolded and true spectra prove the soundness of the approach.

In order to verify the capabilities of the TUnfold software, it has been tested on a dedicated *FLAT* simulation, in which photons with a flat energy spectrum from 0 MeV to 15 MeV have been generated from the PMMA itself. For each event, the true and reconstructed energies were recorded and used to build the unfolding matrix. The decision to unfold the measured energy spectrum using the *FLAT* simulation has been taken since the electromagnetic interactions of photons with the experimental setup are well handled by FLUKA and are not depending on the true production spectra of the photons. Therefore, the unfolding procedure is decoupled from nuclear effects related to the photons production mechanism inside the PMMA, and, hence, it is reliable. The result of the unfolding test is shown in Figure 4.24 for the energy range of interest ($1 - 10$ MeV), where the measured spectrum (blue circles), the true spectrum (red squares) and the result of the unfolding (black triangles) are superimposed. The agreement between the unfolded and true spectra is the evidence

that the unfolding technique used is working.

In order to tune the unfolding parameters to be used in the unfolding procedure of the measured data, the *FLAT* based unfolding matrix has been applied to the simulated measured spectrum obtained from the full MC simulation. The unfolding tuning was done by varying the regularization method, the regularization strength (τ) and the input spectrum binning, scanning the parameters phase space and minimizing the chi-square of the unfolded distribution computed against the true generated energy spectrum. The final choice for the TUnfold algorithm foresee: regularization size scheme, 35 bins, and τ that is a function of the sample statistics and thus varies for the 60°, 90° and 120° analysis. To asses the systematic uncertainty related to the unfolding procedure, the unfolding parameters have been varied around the chosen values and the unfolding matrix from the full MC simulation has been used.

Once the produced prompt photons N_γ^i is measured from the unfolded spectrum in each energy bin E_i, it is possible to define the prompt photon rate in each energy bin as:

$$\Phi^\gamma(E_i) = \frac{N_\gamma^i}{N_{\mathrm{C}} \times \epsilon_{\mathrm{DT}} \times \epsilon_{\mathrm{geo}}} \tag{4.14}$$

where N_{C} is the number of carbon ions impinging on the PMMA, ϵ_{DT} is dead time inefficiency and ϵ_{geo} is the detector geometrical acceptance.

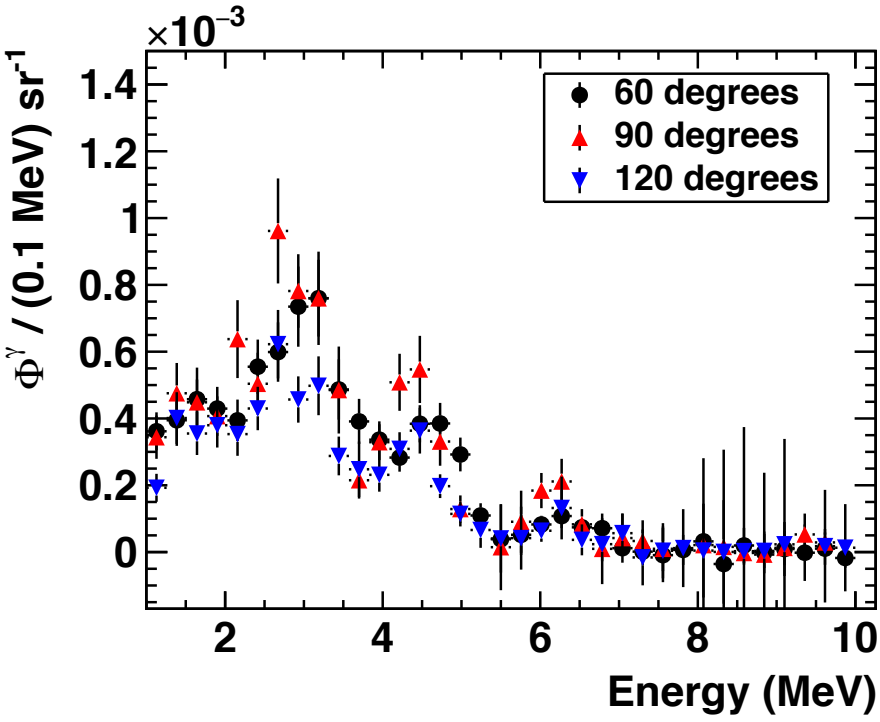

Figure 4.25. Production energy spectra of prompt photons detected by the LYSO scintillator at 60° (circles), 90° (up triangles) and 120° (down triangles). These spectra are normalized to the number of incident ^{12}C ions and are corrected for the dead time inefficiency, the detector efficiency and the detector geometrical acceptance.

The number of incident carbon ions N_C is measured counting the number of AND signals built from the Start Counter output with a scaler module (CAEN V560 N), that continuously counts the trigger signals produced, regardless of the busy signal of the DAQ. Thus N_C does not need to be corrected for the DAQ dead time inefficiency.
The dead time (DT) inefficiency ϵ_{DT} has been computed using the instantaneous event by event rate measured during the data acquisitions. Fitting the rate spectra in the [50 µs − 0.1 ms] range, the rate in the full [0 − 0.1 ms] range has been extrapolated. ϵ_{DT} was measured using the two range values to correct for the non zero DT during the data acquisition. Measured values, varying from few % to 20%, were found to be in good agreement with the different carbon ion mean rates observed during the data acquisition time, varying from 100 kHz to few MHz. To take into account for maximal and minimal DT configurations, we assign a systematic uncertainty to ϵ_{DT} by varying the fit model.
The detector geometrical acceptance ϵ_{geo} was calculated with FLUKA, simulating prompt photons impinging the LYSO crystal with different energies for all angular configurations.
Figure 4.25 shows the resulting prompt photons production rate as a function of the production energy, obtained for the angular configurations at 60° (circles), 90° (up triangles) and 120° (down triangles).

Prompt photon integrated rates

In order to check the feasibility of a prompt gamma on-line detection dose monitoring device, it is crucial to measure the prompt photon flux per number of carbon ions. The prompt photon production rate has been defined as the energy integral of the prompt photon spectrum between 2 MeV and 10 MeV, according to equation 4.14. The resulting integrated rates of prompt photons measured with the LYSO crystal in the angle configurations at 60°, 90° and 120° are listed below:

$$\Phi^{\gamma}(E > 2 \text{ MeV } @60^{\circ}) = (6.59 \pm 0.22_{\text{stat}} \pm 1.07_{\text{sys}}) \times 10^{-3}\ sr^{-1} \tag{4.15}$$

$$\Phi^{\gamma}(E > 2 \text{ MeV } @90^{\circ}) = (7.39 \pm 0.38_{\text{stat}} \pm 1.27_{\text{sys}}) \times 10^{-3}\ sr^{-1} \tag{4.16}$$

$$\Phi^{\gamma}(E > 2 \text{ MeV } @120^{\circ}) = (5.02 \pm 0.24_{\text{stat}} \pm 1.34_{\text{sys}}) \times 10^{-3}\ sr^{-1} \tag{4.17}$$

The main contributions to the systematic error come from:

i. the fit model variation of the dead time inefficiency ϵ_{DT};

ii. the TunfoldSys package of TUnfold, that evaluates a systematic error by using the full MC matrix for the unfolding instead of the *FLAT* matrix;

iii. the unfolding τ parameter scanning.

The impact on the results of a Geant4 (*Agostinelli et al.* [69], *Allison et al.* [70]) based unfolding matrix has also been checked: this systematic error is already accounted by the full instead of *FLAT* matrix.

Low energy charged particles can contribute to the N_γ^{rec} signal evaluated from the time pull distributions. However, such low energy electrons ($2 - 10$ MeV) that can mimic the signal from prompt gammas, should fire the DCH cells. Then, to test the robustness of the fluxes obtained, we use the Drift Chamber information to compute again the fluxes including a selection on the number of cells (N_{hits}) hit in the DCH. Charged particles are identified as events with $N_{hits} \geq 8$ with an efficiency of $\sim 98\%$. Therefore, the prompt gamma rates have been computed including the selection $N_{hits} < 8$. The new rates results are compatible with the ones obtained without a N_{hits} selection (eq. 4.15 - 4.17).

The rate at 90 degrees can be compared with *Agodi et al.* [53] [54]: with an 80 MeV/u ^{12}C beam, the measured rate is $(2.32 \pm 0.15) \times 10^{-3}$ sr^{-1}, as described in Section 4.3.2. Since both the path and the energy of the carbon ion in the target is related with the number of prompt photons emitted, a different rate is expected for different energy beams (the ion penetration depth is proportional to the incident beam energy). The rate measured with a 220 MeV/u ^{12}C beam is $(7.39 \pm 1.32) \times 10^{-3}$ sr^{-1}. The higher energy beam produces a higher prompt photon flux than the lower energy beam. The production rates obtained in the three different angular configurations (60°, 90° and 120°) are comparable with each other (see eq. 4.15 - 4.17), as expected for an almost isotropic emission of prompt photons coming from nuclear de-excitations.

4.3.4 Preliminary data from ^4He and ^{16}O ion beams

In the HIT experiment, the prompt photons radiation has been measured using helium and oxygen ion beams of different energies:

$$^4He \quad 102 \text{ MeV}/u \quad , \quad 125 \text{ MeV}/u \quad , \quad 145 \text{ MeV}/u$$

$$^{16}O \quad 210 \text{ MeV}/u \quad , \quad 300 \text{ MeV}/u$$

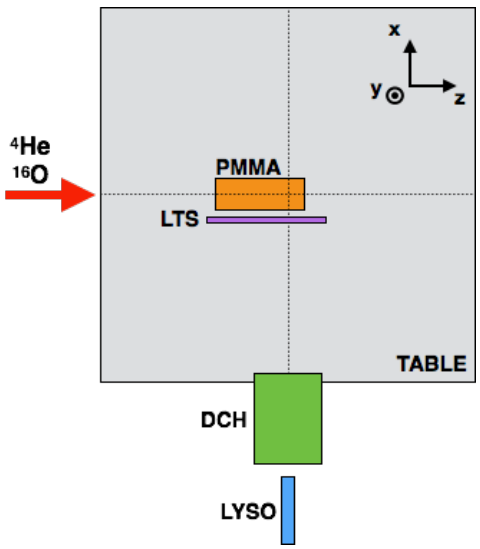

Figure 4.26. Sketch of the experimental setup of the HIT experiment for the prompt gamma measurement (not to scale).

The setup geometry for the prompt gamma measurement is shown in Figure 4.26, where the LYSO is the detector used in the GSI experiment as well as the DCH and SC (see Section 4.1). The TABLE is a 1 cm thick aluminum table of 50×50 cm^2 (the same used at GSI). The PMMA is 5×5 cm^2 in the x-y dimensions, while the z dimension varies as a function of the beam energy in order to have the BP always positioned on the TABLE center. The LTS is the Large Thin Scintillator, with dimensions of $0.2 \times 5 \times 15$ cm^3. Placed beside the PMMA exit face on the LYSO side, it is used together with the LYSO detector in order to provide the Time of Flight of secondary charged particles.

Since the HIT accelerator is a synchrotron, the beam time structure is bunched. An example of the HIT beam structure is given for a 102 MeV/u helium beam in Figure 4.27. The spill duration time is ~ 3 s while the time distance between two consecutive spills is ~ 7 s.

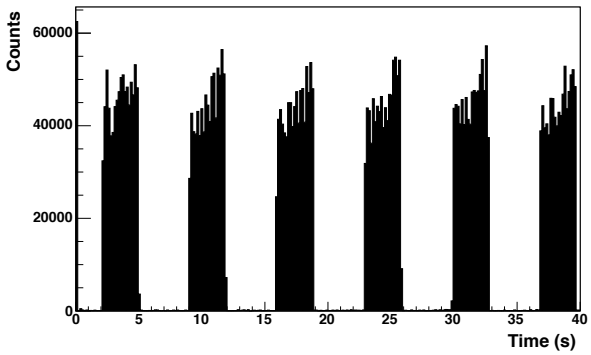

Figure 4.27. Example of a 102 MeV/u ^4He beam structure at HIT.

In order to obtain the prompt photons energy spectrum, for the HIT data analysis the same procedure involved for the LNS data analysis has been adopted. A preliminary plot for the deposited energy[1] in the LYSO detector as a function of the time difference between the LYSO and SC, corrected for the time slewing effect ($\Delta T_{\rm corr}$, as defined in equation 4.4 with a correction $C(E)$ specific for this analysis), is shown in Figure 4.28, for all helium (left) and oxygen (right) beams (all the beam energies are summed in order to make visible the photon band).
From the $E_{\rm LYSO} - \Delta T_{\rm corr}$ distribution, a dataset of the pull distribution (see equation 4.5) in each energy bin has been obtained. With the use of the RooFit toolkit, the unbinned fit to the pull dataset in each energy bin has been performed and from the likelihood minimization the number of photons can be extracted. This procedure is the one described in Section 4.3.3 for the same purpose. Figure 4.29 shows the preliminary raw prompt photons energy spectra (blue dots) for the helium beams (left column) and oxygen beams (right column). A structure at ~ 4 MeV due to the carbon ion de-excitation line is visible.

[1] A dedicated energy calibration of the LYSO detector for the HIT experiment has been performed. No calibration in the extended photon energy range $1 - 10$ MeV has been feasible for the HIT experiment as done for the GSI because of technical problems that will be investigated.

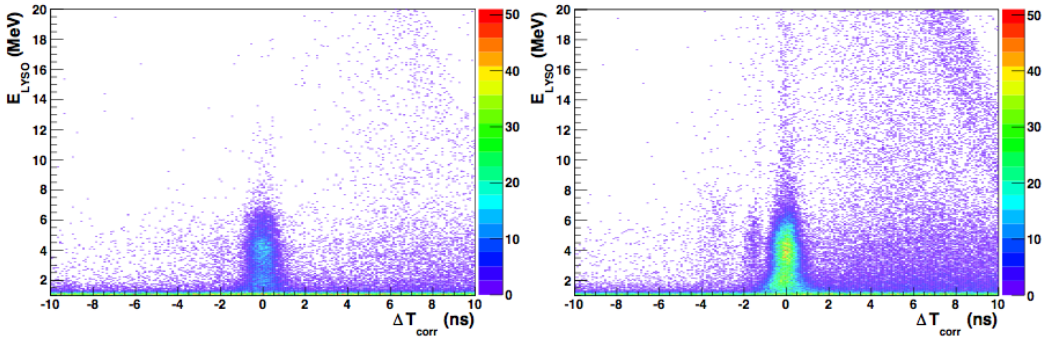

Figure 4.28. Deposited energy in the LYSO detector as a function of the corrected ToF between the LYSO and SC scintillator, for all energies of ^4He beam (left) and ^{16}O beam (right).

Also for the HIT data, a detailed simulation with the FLUKA Monte Carlo has been performed. Figure 4.29 shows also a comparison with the simulated prompt photons energy spectra (red line) normalized to the number of data events. A fairly good agreement between the measured and simulated data can be observed overall, even if the MC seems to show a better LYSO energy resolution with respect to the measured data.

More accurate studies on the HIT data are ongoing. Improvements are expected both on the data analysis as well as on the FLUKA simulation of the detector response.

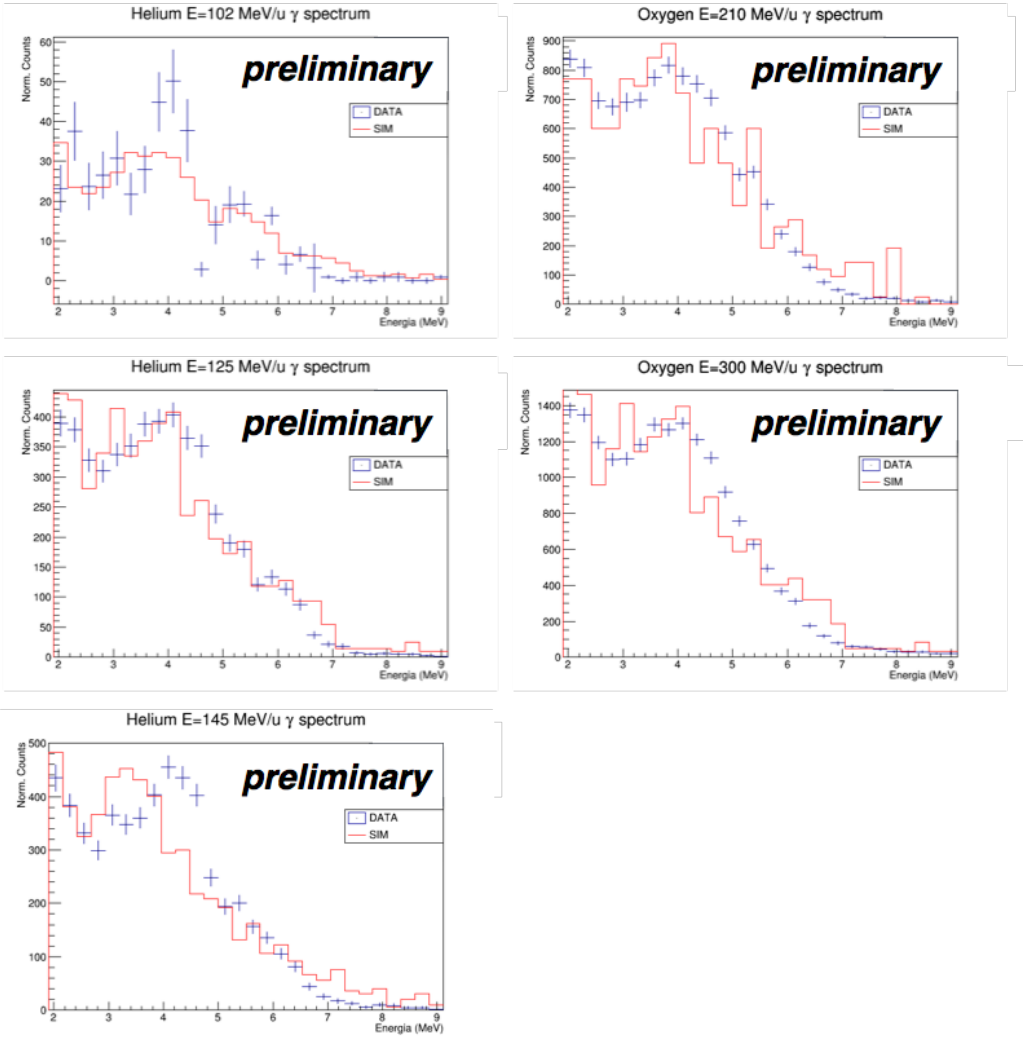

Figure 4.29. Prompt photons raw energy spectrum (blue dots) for the helium beam (left column) of energy 102 MeV/u (top), 125 MeV/u (middle) and 145 MeV/u (bottom) and for oxygen beam (right column) of energy 210 MeV/u (top) and 300 MeV/u (middle). All the spectra are shown from ~ 2 MeV in order to cut the component from the LYSO intrinsic background. The FLUKA simulations, normalized to the number of data events, are superimposed (red line).

4.4 Secondary Charged Particles Measurements

The novel idea to exploit the secondary charged radiation for on-line dose monitoring in particle therapy has been recently proposed and, following this idea, an experimental campaign has started. In this section the experiments performed at LNS and GSI laboratories, involving a carbon beam of 80 MeV/u and 220 MeV/u respectively and focused on the secondary charged particles study are presented. The data analysis and obtained results are here reported. Preliminary results from the HIT experiment, involving helium and oxygen ion beam at different energies, are also shown.

Using the setup geometry already described in Section 4.1, the LNS experiment assessed the possibility to use secondary charged radiation for dose monitoring purposes: secondary charged particles have been detected at 90° and a correlation between the secondary charged particles emission profile and the Bragg peak position has been observed. The measured fluxes have disclosed the opportunity to use such fragments in a real treatment for the Bragg peak position monitoring.
After the LNS measurements, in the GSI experiment some more quantitative aspects have been evaluated. The reconstruction of the emission profile distribution of secondary charged particles produced by a ^{12}C ion beam at a typical therapeutical energy has been characterized and some parameters have been identified to estimate the Bragg peak position inside the target. The energy spectra of secondary charged fragments have been measured, as well as the production rates. Measurements at different detection angles with respect to the beam direction (60°, 90° and 120°) have been performed in order to study the angular dependance of the secondary charged radiation emission.

4.4.1 Particle Identification

To detect charged particles exiting from the PMMA target, a Drift Chamber has been used (see Section 4.1.3), operating also as a neutral events veto, and the trigger signal for secondary charged events was provided by the time coincidence between the Start Counter and the LYSO crystals, within 80 ns. Considering the geometrical setup (see Figure 4.1), an ion traveling from the PMMA to the LYSO is likely to hit all the twelve Drift Chamber planes. Thus, an event selection based on the number of fired cells (*hits*) in the DCH has been performed.

Figure 4.30 shows the distribution of the number of hits (N_{hits}) in the Drift Chamber for events detected by the LYSO crystals, with a measured energy $E_{\text{LYSO}} >$ 1 MeV in the 90° configuration. Data and FLUKA Monte Carlo predictions are compared also for the hydrogen isotopes, which are the most abundant secondary charged particles. The clear peak at $N_{\text{hits}} = 12$ is clearly seen indicating the signature of the charged particles that crossed all the DCH planes, firing one cell per plane.

The main contribution to the data-MC disagreement observed in the $N_{\text{hits}} < 8$ range is mainly due to the absence of a detailed Monte Carlo simulation of the electronics cross-talk and of the beam halo inducing particle production. Events in which the reconstructed tracks satisfy the $N_{\text{hits}} > 8$ requirement have been selected for the secondary charged particles analysis.
The isotopes discrimination has been made using the correlation between the LYSO deposited energy (E_{LYSO}) and the charged particle Time of Flight (ToF). Knowing

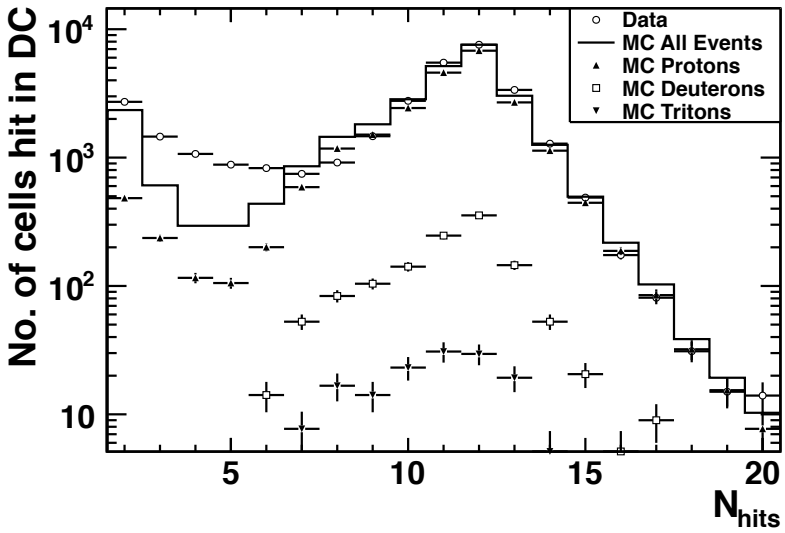

Figure 4.30. Data (circles) and MC (solid line) distributions of the number of hit cells in the Drift Chamber (N_{hits}) for events detected by the LYSO crystals ($E_{\text{LYSO}} > 1$ MeV) in the 90° configuration. Individual contributions from protons (up triangles), deuterons (squares) and tritons (down triangles), obtained from the simulation, are shown. The MC data have been normalized to the experimental data using the $N_{hits} = 12$ bin.

the measured charged particle arrival time on LYSO recorded by the TDC, the ToF is the sum of two contributions. The first contribution is the time taken by the primary carbon ion to travel from the Start Counter to its point of interaction inside the PMMA target where the secondary charged particle is produced ($T_{ch}(\overrightarrow{x}) - T_{^{12}C}$). The second contribution to the ToF is the time taken by the secondary charged particle to emerge from the PMMA and interact in the LYSO detector ($T_{LY} - T_{ch}(\overrightarrow{x})$).

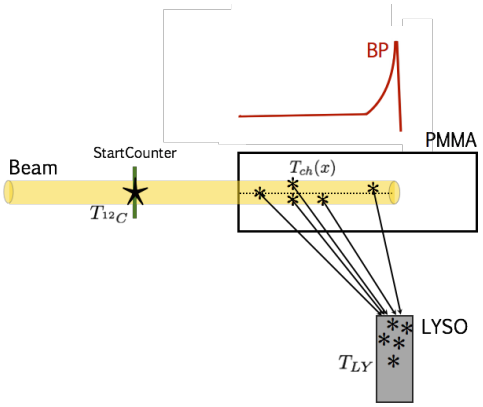

Figure 4.31. Scheme used for the evaluation of secondary charged particles ToF (not to scale). The beam spot size is shown (yellow cylinder) as well as the beam dose deposition inside the PMMA (red solid line).

A scheme of the ToF evaluation is shown in Figure 4.31. The time required by a ^{12}C ion to reach its interaction point in the PMMA target was evaluated by means of a dedicated full FLUKA MC simulation. It was properly taken into account for the GSI experiment, since the $T_{^{12}C}$ contribution is non negligible for the GSI beam energy. On the other hand, at LNS the beam propagation time has not been considered in the ToF computation, due to the small range of 80 MeV/u carbon ions in the PMMA ($\sim$ 1 cm).

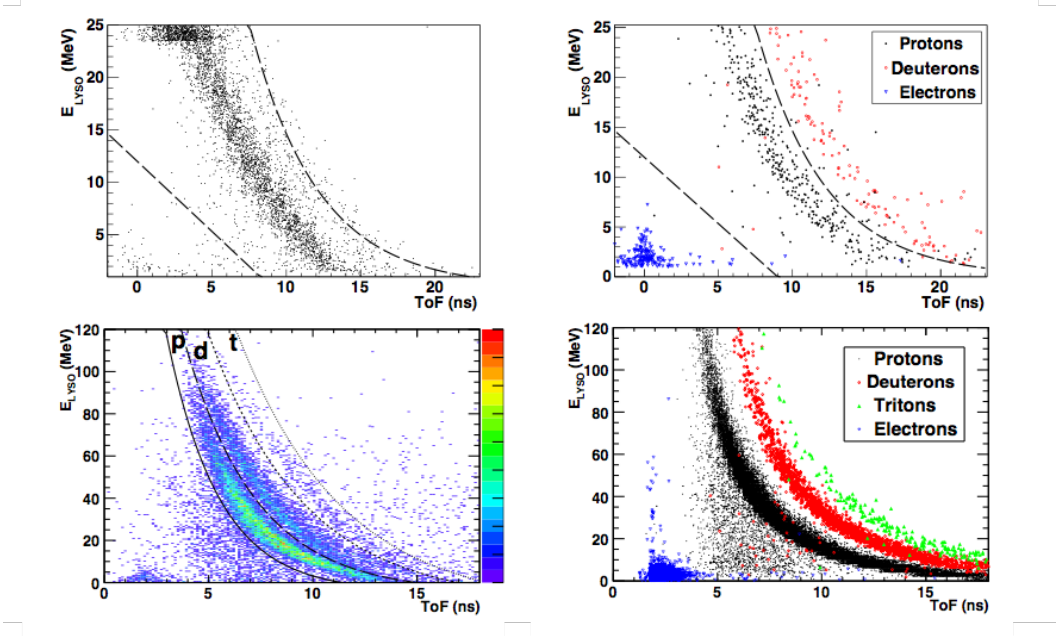

Figure 4.32. Distributions of the deposited energy in the LYSO crystals as a function of the Time of Flight for the LNS (top) and GSI (bottom) experiments, in the setup configuration at 90°, for the selected secondary charged particles. The experimental data (left) are compared with the FLUKA simulations (right). The PID functions are superimposed for the LNS experiment and GSI data in order to discriminate among different secondary charged particles populations.

Figure 4.32 shows the measured E_{LYSO} - ToF distribution (left column) compared with the simulated distribution (right column, already shown in Section 4.2, see Figure 4.14) for the LNS (top) and GSI (bottom) experiments, in the setup configuration at 90°. The Particle Identification (PID) functions are superimposed in order to discriminate among different secondary charged particles populations. In the LNS data sample (top left panel) a fast low-energy component due to electrons is clearly visible for ToF values around zero. These electrons are due to Compton scattering of the de-excitation photons produced by the beam interactions in the PMMA target. The central most populated band, delimited by the two dashed lines, are protons with detected energy within a very wide range. A saturation of the LYSO ADC for $E_{\mathrm{LYSO}} > 24$ MeV is visible. The LNS FLUKA simulation (right top panel) shows similar populations in the (ToF, E_{LYSO}) plane with an additional component of deuterons, which could not be resolved in data.

For the GSI experiment (bottom panels), the data (left) and MC (right) distributions show a similar trend, with three well separated regions for protons (p), deuterons (d) and tritons (t), identified by a solid, dashed and dotted lines respectively, that have been superimposed in Figure 4.32 (bottom left panel).

A contribution to the systematic uncertainty on the flux measurements, that will be described in Section 4.4.3, has been evaluated moving these separation lines, in order to account for the cross feed among different populations.

Figure 4.33 shows the E_{LYSO} - ToF distribution for the GSI experiment, in the setup configuration at 60° (left) and 120° (right). As it can be seen, there is a huge increase in statistics for the 60° angular configuration with respect to the one at 90°, while in the 120° setup there is a statistical drop (it has to be remembered that the secondary charged particles emission is not isotropic). For this reason, the following analysis will refer to the 90° and 60° angular configurations only.

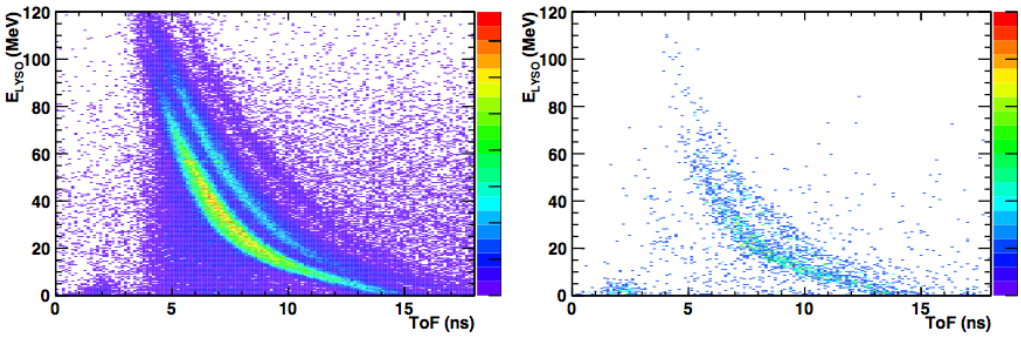

Figure 4.33. Data distributions of the deposited energy in the LYSO crystals as a function of the Time of Flight for the selected secondary charged particles in the GSI experiment, in the setup configurations at 60° (left) and 120° (right).

The differences between the data (left) and simulated (right) E_{LYSO} - ToF distributions shown in Figure 4.32 are due to different contributions. First of all, it has to be pointed out that the LYSO detector calibration, described in Section 4.1.2, as well as the assessment of the quenching, was performed involving radioactive sources providing photons with energy up to 9 MeV, while the energy of secondary charged particles spans a wider range, up to $\sim$ 30 MeV for the 80 MeV/u ^{12}C beam (LNS) and $\sim$ 120 MeV for the 220 MeV/u ^{12}C beam (GSI). The applied calibration is a linear calibration, without taking into account non-linear contributions or quenching effects that charged particles may have. Moreover, in the FLUKA Monte Carlo simulation, the energy resolution for charged particles has been modeled with the photons calibration, not accounting for particle type differences.
Furthermore, the nuclear models driving the charged particles production in the simulation are still under development and tuning on other published data.

4.4.2 Velocity distribution

As explained in the previous section, the LYSO deposited energy calibration is considered to be valid up to 9 MeV, while, for larger energies, saturation and nonlinear effects are expected to give a significant contribution. Therefore, in order to give an estimation of the true energy of the secondary charged particles detected, the distributions of $\beta = v/c$ (with c the speed of light and v the fragment velocity) and consequently the relative detected kinetic energy E_{kin} have been computed.
The kinetic energy measurement of charged fragments is very important in order to build a charged particle monitor for PT, since the secondary charged fragments must emerge from the patient to be detected, *i.e.* must be emitted with enough energy.

In the LNS experiment, the β evaluation has been obtained using the ToF and the PMMA-LYSO distance (d) measurement for all the identified protons:

$$\beta = \frac{ToF}{d \cdot c} \, . \tag{4.18}$$

The procedure used for the kinetic energy calculation was then to compute the detected kinetic energy, evaluated from the β measurement, and related it to the kinetic energy at emission time ($E_{\text{kin}}^{\text{Prod}}$) considering the energy loss in the PMMA target and the quenching effect of the scintillating light in the LYSO detector for low energy protons (see the previous section for the proton events selection). In Figure 4.34, the proton β distribution (left) and kinetic energy (right) are shown.

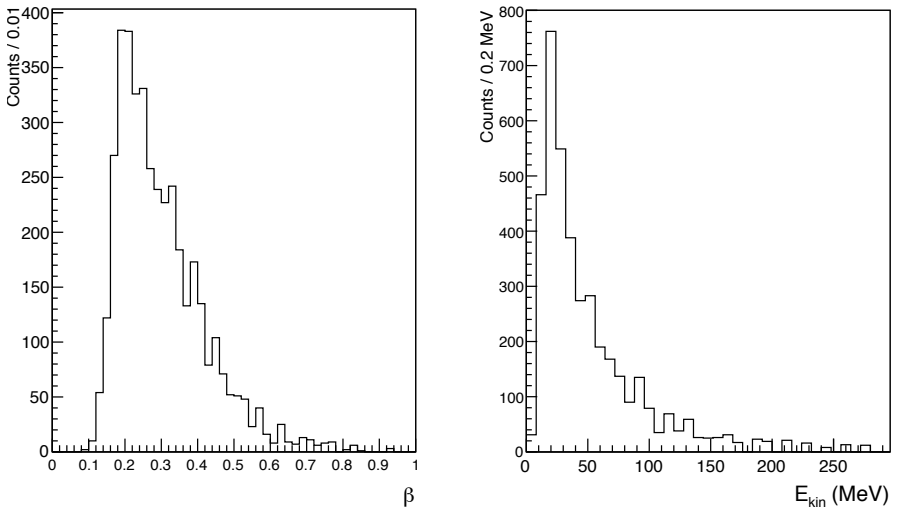

Figure 4.34. Distribution of β (left) and detected kinetic energy (right) of secondary charged particles identified as protons (LNS experiment).

To obtain the production kinetic energy from the detected one, the energy loss in the PMMA must be taken into account. Relating the E_{kin} to the $E_{\text{kin}}^{\text{Prod}}$, using the FLUKA simulation, the minimum required production energy to detect a proton in the LYSO crystals, in the LNS experimental configuration, is $E_{\text{kin}}^{\text{Prod}} = 48 \pm 5$ MeV. Moreover, it has to be remembered that also for a real on-line dose monitoring

purpose exploiting secondary charged particles, the crossing of some centimeters of patient's tissue has to be considered. Therefore, the most interesting detected kinetic energy range for application is $E_{\text{kin}} > 60$ MeV. An average detected kinetic energy of $E_{\text{kin}} = 60$ MeV corresponds to a production energy of $E_{\text{kin}}^{\text{Prod}} = 83 \pm 5$ MeV, where the uncertainty is mainly due to the beam spot size ($\mathcal{O}(1$ cm)).

In the GSI experiment, the evaluation of the β spectrum has been done with a more sophisticated procedure. As in the LNS experiment, the GSI β distributions were obtained using the ToF spectra shown in Figure 4.35, for the 90° (left) and 60° (right) angular configurations, for the identified protons, deuterons and tritons. The measured ToF distributions for the different isotopes were obtained taking into account several factors such as the different depths of interaction of each kind of particle giving different paths length from the emission point to the LYSO detector, and the different energy loss within the target. Moreover, the beam spot size and the multiple scattering effect of secondary charged particles contribute in smearing the ToF distributions.

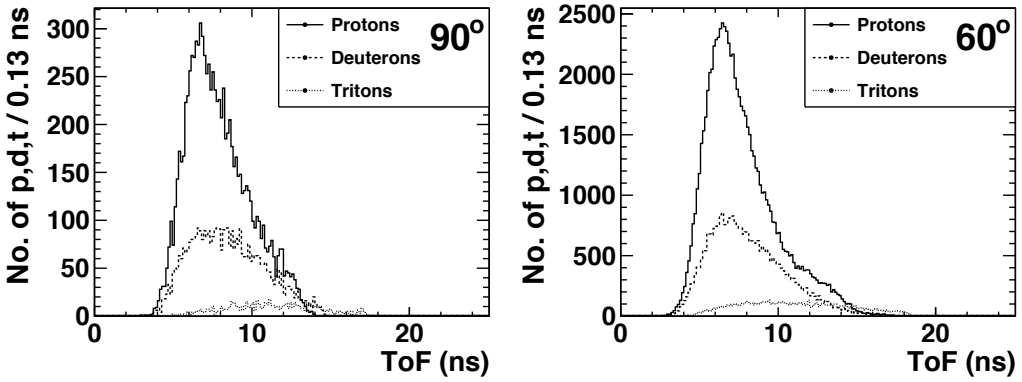

Figure 4.35. Measured Time of Flight distributions for protons (solid line), deuterons (dashed line) and tritons (dotted line) in the GSI setup angular configuration at 90° (left) and 60° (right).

It has to be underlined that for all the aforementioned processes, particles with the same ToF but different emission kinetic energy can occur, avoiding the possibility to compute the β quantity directly from the ToF measurement. Thus, the β spectrum for protons, deuterons and tritons has been evaluated with the help of a dedicated FLUKA simulation. Figure 4.36 shows the simulated spread of the ToF spectrum with respect to the β distribution for protons (β_p, top panel), deuterons (β_d, middle panel) and tritons (β_t, bottom panel) secondary fragments. β here is the production velocity.

Using the MC simulation, the probability matrix $P^{p,d,t}_{\beta \to ToF}$ was built using the known simulated values of β and their corresponding simulated ToF (Figure 4.36). Each matrix element gives the probability for a particle produced with a given β value to reach the LYSO detector with a certain ToF value. The non zero dimension of the GSI beam ($\sigma_{\text{beam}} \sim 1$ cm), and the corresponding differences in the deposited energy in the PMMA, is the main source of this ToF fluctuation.

Indicating with N_j^{β} the number of secondary particles emitted with a velocity β_j and with N_i^{ToF} the number of secondary particles reaching the LYSO crystals in a time ToF_i, the following relation follows:

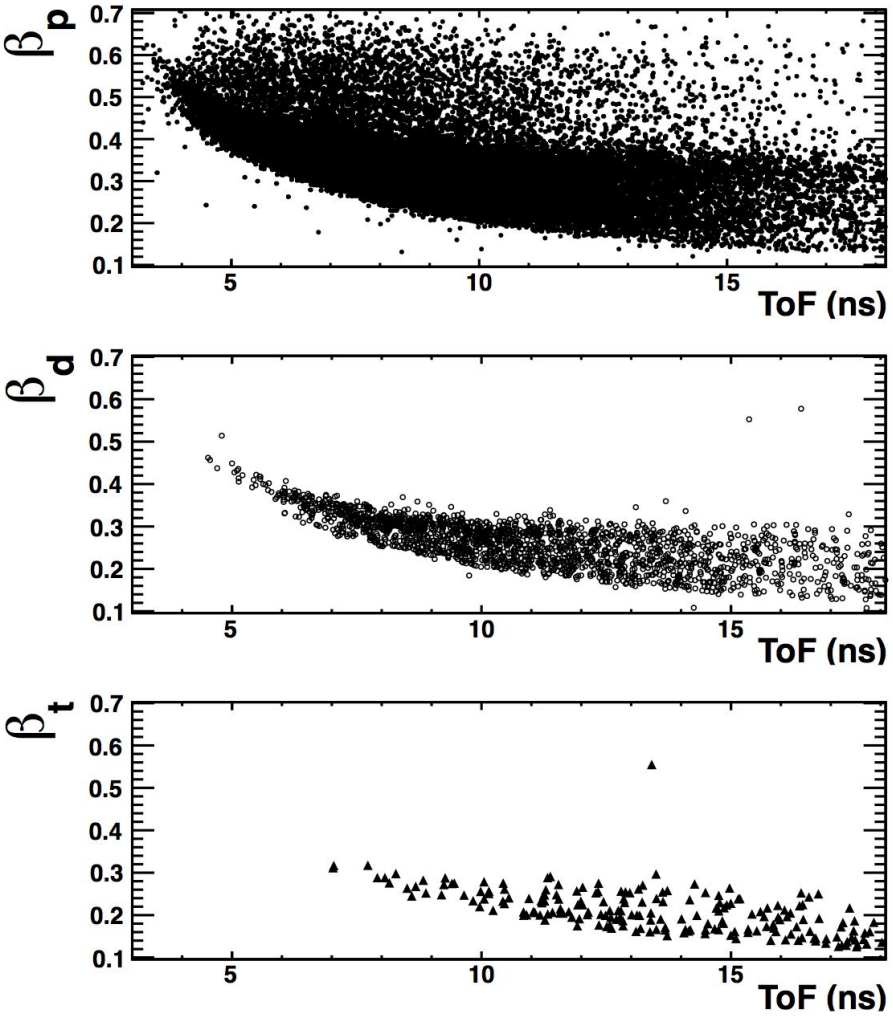

Figure 4.36. FLUKA simulations for protons (top), deuterons (middle) and tritons (bottom) production β spectrum as a function of the ToF for the 90° experimental setup.

$$N_i^{ToF} = \sum_j [P_{\beta \to ToF}]_{ij} \; N_j^{\beta} \; . \tag{4.19}$$

In order to extract the β distribution from the measured ToF, equation 4.19 has to be inverted:

$$N_j^{\beta} = \sum_i [P_{\beta \to ToF}]_{ji}^{-1} \; N_i^{ToF} \; . \tag{4.20}$$

This relation has been solved with the unfolding procedure described by *Mosegaard and Tarantola* [71]. A probabilistic approach to find the best N_i^{β} configuration has

been used in order to minimize the following function:

$$\chi^2 = \sum_j \left[\frac{N_j^{ToF} - [\sum_i (P_{\beta \to ToF})_{ji} \; N_i^{\beta}]}{\sqrt{N_j^{ToF}}} \right]^2 . \tag{4.21}$$

The reconstructed emission velocity β_{rec} and the measured ToF distributions were binned in 20 equally spaced bins, evaluating the impact on the unfolding result of the binning. The differences in the unfolded spectra β_{rec} with different binning were used to compute a systematic uncertainty on the β values.

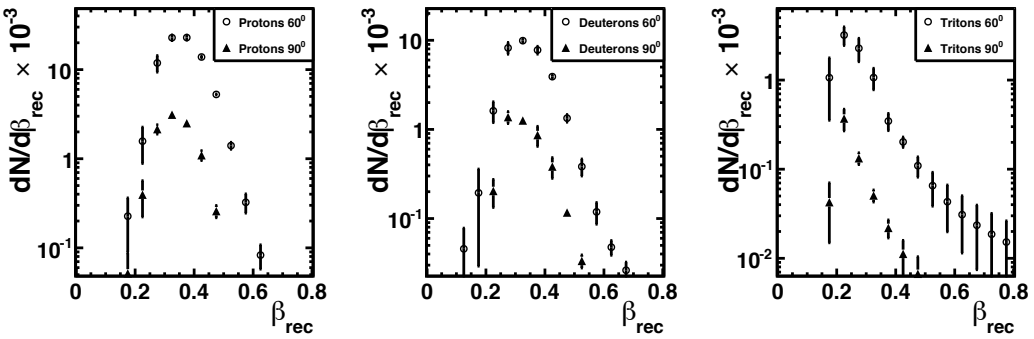

Figure 4.37. Measured emission velocity (β_{rec}) distributions for protons (left), deuterons (middle) and tritons (right) in the angular configuration at 90° (triangles) and 60°(circles). The error bars show the total (statistical plus systematic) uncertainty.

Figure 4.37 shows the reconstructed emission β distributions for protons (left), deuterons (middle) and tritons (right) obtained after the unfolding, for the experimental configuration at 90° (triangles) and 60° (circles). For each angular configuration, all spectra were normalized to the relative number of isotope species detected by the LYSO crystals. The error bars show the total (statistical and systematic) uncertainty.

4.4.3 Production Rates

The measurements of production rates of secondary charged fragments produced in the interaction of a carbon ion beam with a PMMA target is necessary in order to exploit the feasibility of an on-line dose monitoring technique based on the secondary charged particles detection. Therefore, using the 80 MeV/u ^{12}C beam at LNS and the 220 MeV/u ^{12}C beam at GSI, in the setup configurations sketched in Figure 4.1, the secondary charged particles production rates have been evaluated.

The secondary charged particles production rate has been computed using the same relation for the prompt photons production rate evaluation described in equation 4.12, taking into account also the Drift Chamber tracking efficiency:

$$\Phi^{ch}(\Omega_{\mathrm{LYSO}}) = \frac{1}{N_{\mathrm{C}}} \left[\frac{N_{\mathrm{ch}}}{\epsilon_{\mathrm{DT}} \epsilon_{\mathrm{LYSO}} \epsilon_{\mathrm{track}} \Omega_{\mathrm{LYSO}}} \right] . \tag{4.22}$$

For the LNS experiment, in the 90° setup configuration, for the triggering LYSO crystals, having a surface of 3×3 cm^2 and placed at a distance of 74 cm from the PMMA centre, the detector solid angle is $\Omega_{\mathrm{LYSO}} \sim 1.6 \times 10^{-3}$ sr. The LYSO detection efficiency ϵ_{LYSO} for secondary protons with $E_{\mathrm{LYSO}} > 1$ MeV has been evaluated using the FLUKA simulation, having included the measured proton's kinetic energy spectrum (Figure 4.34, right). The obtained value is $\epsilon_{\mathrm{LYSO}} = (98.5 \pm 1.5)\%$, with the uncertainty mainly due to the Monte Carlo statistics. The number of emitted secondary protons N_{P} has been obtained by the number of identified and tracked protons and corrected for the Drift Chamber tracking efficiency $\epsilon_{\mathrm{track}} = (98 \pm 1)\%$ (*Abou-Haidar et al.* [64]). The other quantities are the same as the ones used to compute the LNS prompt photon flux (see Section 4.3.2).
Figure 4.38 shows the production rate of secondary protons (all energy protons and protons with detected kinetic energy $E_{kin} > 60$ MeV) produced by an 80 MeV/u carbon ion beam impinging on a PMMA target at LNS, that are detected at 90° with respect to the beam direction, as a function of the carbon ions rate R_{C} arriving to the PMMA.

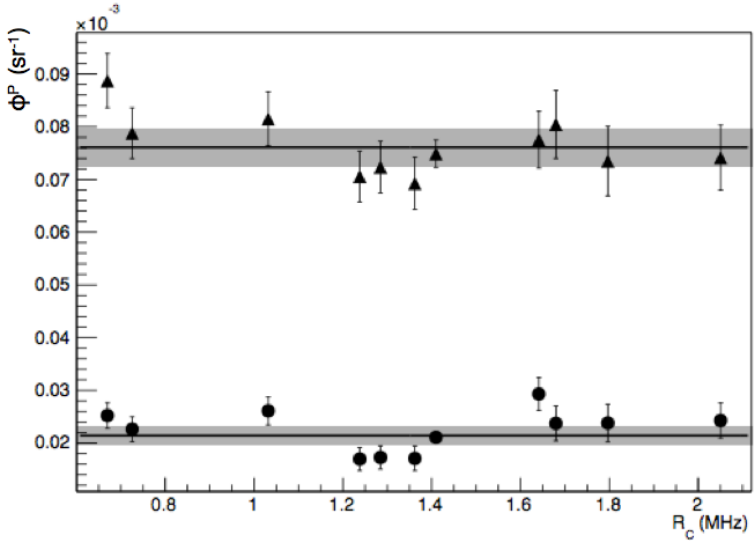

Figure 4.38. Production rate of all identified secondary protons (triangles) and secondary protons with detected $E_{\mathrm{kin}} > 60$ MeV (circles) detected in the angular configuration at 90°, as a function of the carbon rate R_{C} arriving to the PMMA target.

The obtained results are the following:

$$\begin{aligned} \Phi^P(\Omega_{\mathrm{LYSO}})_{\theta=90^\circ} &= (0.761 \pm 0.014_{\mathrm{stat}} \pm 0.032_{\mathrm{sys}}) \times 10^{-4} sr^{-1} \ , \\ \Phi^P(\Omega_{\mathrm{LYSO}})_{E_{\mathrm{kin}}>60\ \mathrm{MeV},\theta=90^\circ} &= (0.214 \pm 0.006_{\mathrm{stat}} \pm 0.010_{\mathrm{sys}}) \times 10^{-4} sr^{-1} \end{aligned}$$

with the systematic contribution mainly due to the proton identification (see Section 4.4.1) and to the uncertainty on the production kinetic energy related to the beam's transversal profile uncertainty.

The production rate has been computed also at the GSI experiment using the same relation in equation 4.22, measuring secondary fragments such as protons, deuterons and tritons (p, d, t) produced in the interaction of a 220 MeV/u carbon beam impinging on a PMMA target. Since the geometry of the experimental setup is slightly different as well as the Data Acquisition chain with respect to the LNS experiment, some quantities have been re-computed. The number of protons $N_{\rm p}$, deuterons $N_{\rm d}$ and tritons $N_{\rm t}$ have been calculated from the selected tracks measured after the PID selection application (see Section 4.4.1). The angular acceptance $\Omega_{\rm LYSO} \sim 2\times10^{-3}\ sr$ has been evaluated from the FLUKA full simulation (see Section 4.2). The Drift Chamber tracking efficiency and the LYSO scintillator detection efficiency were computed using a high-statistics FLUKA MC simulation. The LYSO scintillator detection efficiency for each isotope (p, d, t) and angle configuration (90°, 60°), has been evaluated and found to be in the range $\epsilon_{\rm LYSO} = 96\% - 97\%$, depending on the isotope and detection angle, with a negligible statistical uncertainty. The DCH tracking efficiency $\epsilon_{\rm track} = 93 \pm 3\%$ was computed using the $N_{\rm hits}$ distribution shown in Figure 4.30, where the main contribution to the uncertainty is systematic. The systematic uncertainty was evaluated by variating the cut on the $N_{\rm hits}$ distribution for the charged particles selection. The dead time inefficiency $\epsilon_{\rm DT}$ was measured as described in Section 4.3.3, as well as the number of impinging carbon ions $N_{\rm C}$.

The measured integrated production rates for p, d and t secondary fragments produced in the interaction of a 220 MeV/u carbon beam with a PMMA target, in the 60° and 90° angular configurations are:

$$\begin{aligned}
\Phi^p(\Omega_{\rm LYSO})_{\theta=60^\circ} &= (8.78 \pm 0.07_{\rm stat} \pm 0.64_{\rm sys}) \times 10^{-3}\ sr^{-1}\ , \\
\Phi^d(\Omega_{\rm LYSO})_{\theta=60^\circ} &= (3.71 \pm 0.04_{\rm stat} \pm 0.37_{\rm sys}) \times 10^{-3}\ sr^{-1}\ , \\
\Phi^t(\Omega_{\rm LYSO})_{\theta=60^\circ} &= (0.91 \pm 0.01_{\rm stat} \pm 0.21_{\rm sys}) \times 10^{-3}\ sr^{-1}\ ,
\end{aligned}$$

$$\begin{aligned}
\Phi^p(\Omega_{\rm LYSO})_{\theta=90^\circ} &= (1.83 \pm 0.02_{\rm stat} \pm 0.14_{\rm sys}) \times 10^{-3}\ sr^{-1}\ , \\
\Phi^d(\Omega_{\rm LYSO})_{\theta=90^\circ} &= (0.78 \pm 0.01_{\rm stat} \pm 0.09_{\rm sys}) \times 10^{-3}\ sr^{-1}\ , \\
\Phi^t(\Omega_{\rm LYSO})_{\theta=90^\circ} &= (0.128 \pm 0.005_{\rm stat} \pm 0.028_{\rm sys}) \times 10^{-3}\ sr^{-1}\ .
\end{aligned}$$

The uncertainties are dominated by the systematic errors of the PID procedure (see Section 4.4.1 for details) and DAQ dead time computation (see Section 4.3.3).

4.4.4 Bragg peak position monitoring

Up to now, the secondary charged particles produced in the interaction of a ^{12}C beam with a PMMA target and arriving to a LYSO detector placed at 90° or 60° with respect to the beam direction have been identified (Section 4.4.1). It has been performed the characterization of the energy of such incoming particles (Section 4.4.2) and their production rates have been measured (Section 4.4.3). Now it has to be investigated if secondary charged particles can be actually used for on-line dose monitoring purposes in PT.

Charged particles can be tracked in order to reconstruct their emission profile and relate it to the path of the carbon ion beam inside the phantom, so to the maximum dose release, *i.e.* the Bragg peak position. At the low energy LNS experiment, in

order to determine if there is a correlation between the reconstructed secondary charged particles emission profile and the BP position, a PMMA position scan has been performed. The PMMA was mounted on a single axis movement stage allowing the position scan along the beam direction with a 0.2 mm accuracy. Moving the PMMA, the BP position in the reference frame changes, since the beam penetration depth in the target remains the same and the beam energy loss in air is negligible for the minimal differences in air thickness between the beam exit window and the PMMA front face during the scan. A study on the emission profile as a function of the BP position has then been developed.

In the LNS experiment, the PMMA target is a $4 \times 4 \times 4$ cm^3 cube and the PMMA position scan was along the x-axis. The configuration with the centers of PMMA, Drift Chamber and LYSO detector aligned along the z-axis has been taken as the reference configuration and the PMMA position in the stage reference frame is taken as 0. In this position the PMMA front face is at $x = 20$ mm. Figure 4.39 shows how the target has been moved up of 13 mm and down of 19 mm along the x-axis.

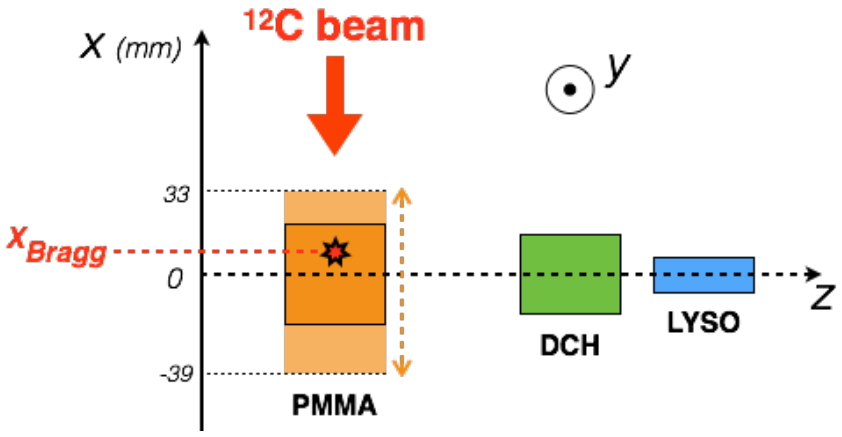

Figure 4.39. Schematic view of the Bragg peak position scanning performed during the LNS experiment (not to scale). According to the FLUKA simulation, the Bragg peak position in the reference configuration is: $x_{\text{Bragg}}|^{\text{Ref}} = (9.0 \pm 0.5)$ mm.

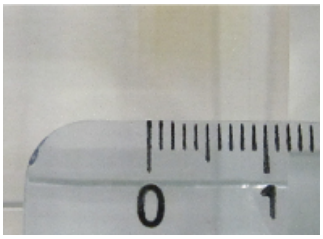

Figure 4.40. Zoommed picture of the PMMA target traversed by the 80 MeV/u ^{12}C beam at LNS. The yellow band is an indication of the target deterioration. Using the ruler, the BP is at ~ 1.1 cm from the PMMA front face, as expected from the FLUKA simulation (*Agodi et al.* [42]).

Since the 80 MeV/u ^{12}C beam penetrates ~ 11 mm through the PMMA target, the Bragg peak position in the reference frame is $x_{\text{Bragg}}|^{\text{Ref}} = (9.0 \pm 0.5)$ mm, and it has been evaluated from a dedicated FLUKA simulation of the experiment. The BP position has also been confirmed by a direct observation of the PMMA target after the data taking, showing a visible yellow band as an indication of the target deterioration (see Figure 4.40).

Each charged track reconstructed by the Drift Chamber is associated with a secondary particle detected in the LYSO crystals. The track has then been backward extrapolated to the beam axis in order to obtain the emission profile distribution within the PMMA target. The x and y coordinates of the estimated emission point of the secondary track have been measured, namely x_{PMMA} and y_{PMMA} (see Figure 4.39).

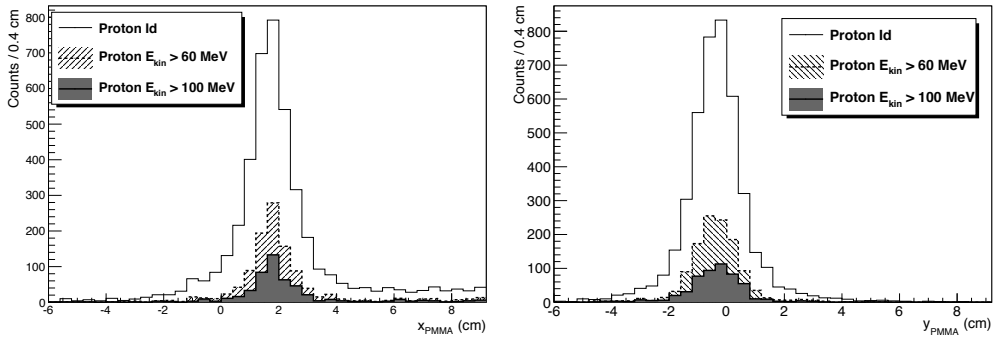

Figure 4.41. Distribution of x_{PMMA} (left) and y_{PMMA} (right) obtained for all the secondary charged particles identified as protons (black solid line), for protons with $E_{\text{kin}} > 60$ MeV (dashed line) and with $E_{\text{kin}} > 100$ MeV (grey). The PMMA front and back faces are at $x_{\text{PMMA}} = 2$ cm and $x_{\text{PMMA}} = -2$ cm, and $y_{\text{PMMA}} = 1.6$ cm and $y_{\text{PMMA}} = -2.4$ cm.

Figure 4.41 shows the distribution of the reconstructed x_{PMMA} and y_{PMMA} in the reference configuration, with different detected kinetic energy E_{kin} thresholds: all the identified protons (solid line), protons with $E_{\text{kin}} > 60$ MeV (hatched) and protons with $E_{\text{kin}} > 100$ MeV (grey). These distributions show no dependency of the emission profile from the kinetic energy of the secondary charged fragments (protons), so the resolution on x_{PMMA} will not vary critically with the kinetic energy of the secondary charged particles for this short beam range.

For each run with different target position, $\bar{x}_{\text{PMMA}}$ and $\bar{y}_{\text{PMMA}}$ have been evaluated from a gaussian fit to the x_{PMMA} and y_{PMMA} distributions, for protons with $E_{\text{kin}} > 60$ MeV. Fig. 4.42 shows the obtained $\bar{x}_{\text{PMMA}}$ and $\bar{y}_{\text{PMMA}}$ as a function of x_{Bragg} assuming different values during the PMMA scan as the beam energy remains the same. A clear linear correlation between $\bar{x}_{\text{PMMA}}$ and x_{Bragg} is observed, indicating that the secondary charged particles emission profile follows accurately the Bragg peak displacement. On the other hand, $\bar{y}_{\text{PMMA}}$ is related to the beam transversal profile and no dependence on x_{Bragg} is observed, as expected from a PMMA translation along the x-axis only.

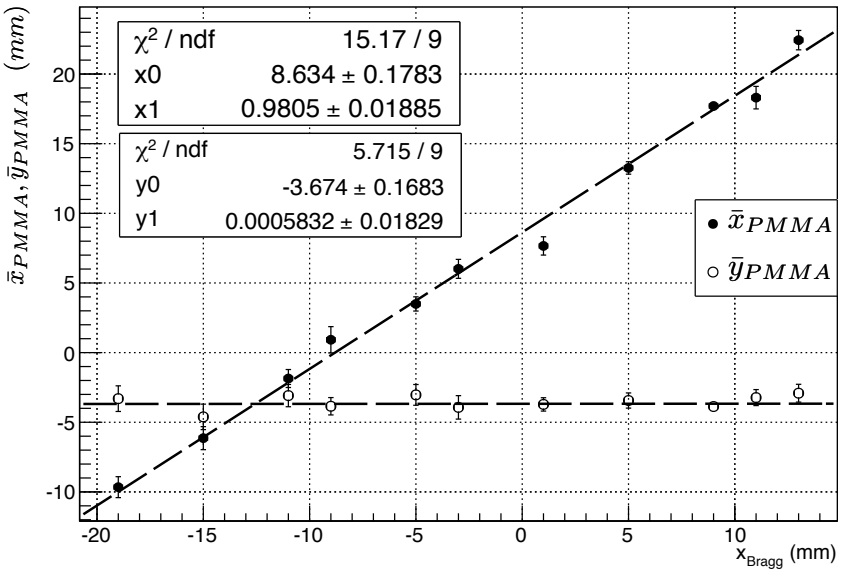

Figure 4.42. Reconstructed peak position of the secondary protons emission profile $\bar{x}_{\mathrm{PMMA}}$ and $\bar{y}_{\mathrm{PMMA}}$ with $E_{\mathrm{kin}} > 60$ MeV as a function of the expected Bragg peak position x_{Bragg}.

The existence of a relationship between the expected Bragg peak position and the emission profile distribution of the secondary charged particles can thus be exploited to find a Bragg peak position monitoring technique based on the x_{PMMA} measurement. Moreover, since $\bar{y}_{\mathrm{PMMA}}$ is related to the fixed beam position in the transverse plane, its behaviour as a function of the PMMA position could provide an estimation of the method uncertainty. The main uncertainties on the Bragg peak position evaluation are due to the multiple scattering interactions undergone by secondary charged particles within the target and the available statistics.
The difference $\Delta_{\mathrm{ProtonBragg}} = \bar{x}_{\mathrm{PMMA}} - x_{\mathrm{Bragg}}$ has been computed both for all identified protons and for the proton sample with $E_{\mathrm{kin}} > 60$ MeV and the obtained root mean square is $\sigma_{\Delta_{\mathrm{ProtonBragg}}} \simeq 0.9$ mm for the two samples. The same value between the two samples is due to the compensation of the multiple scattering interactions and statistics. For all the identified protons the statistics is high as well as the multiple scattering undergone by low energy protons, while for the $E_{\mathrm{kin}} > 60$ MeV selected sample the multiple scattering interactions are suppressed but the statistics is lower.
The total uncertainty on the emission point of secondary charged particles has been estimated as follows:

$$\sigma_{\mathrm{Emission}} = \sqrt{\sigma^2_{\Delta_{\mathrm{ProtonBragg}}} - \sigma^2_{\mathrm{Extrapol}} - \sigma^2_{\mathrm{Stage}}} \sim 0.7 \text{ mm} \tag{4.23}$$

with $\sigma_{\Delta_{\mathrm{ProtonBragg}}} \simeq 0.9$ mm, as discussed before, $\sigma_{\mathrm{Extrapol}} = 0.5$ mm the uncertainty due to the backward extrapolation of the track from the drift chamber to the beam line and $\sigma_{\mathrm{Stage}} = 0.2$ mm the uncertainty due to the PMMA positioning. The value

of σ_{Extrapol} has been obtained from the y_{PMMA} distribution: in principle y_{PMMA} is given by the transverse size of the beam ($\sigma_{\text{beam}} \sim 1$ cm) convoluted with the extrapolation function from the DCH to the beam line.

It has to be stressed that the obtained value on the precision achievable in the Bragg peak position using secondary protons is very preliminary with respect to a possible clinical application. Considering a real treatment case, for instance the lateral thickness traversed by the secondary fragments exiting the patient is the main contribution to the possible worsening on the measured σ_{Emission} during a real therapy treatment. On the other hand, the precision on the BP position determination can be improved increasing, for example, the detector solid angle and so the collected statistics. It must be stressed that in this experiment has been tested the possibility to track the very last part of the beam range, *i.e.* the BP.

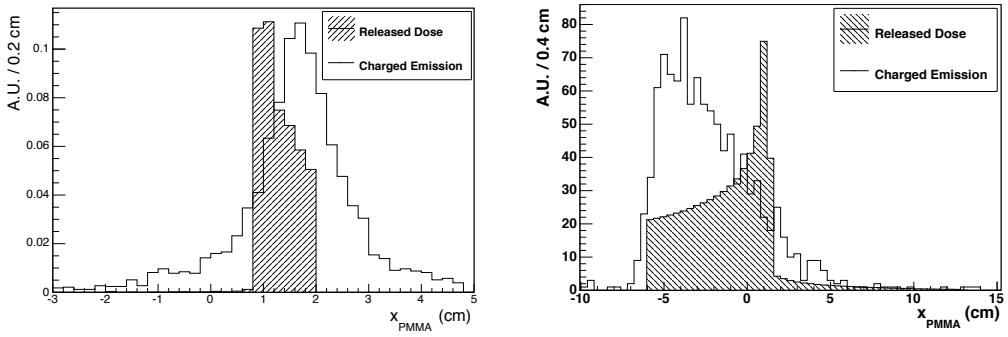

Figure 4.43. FLUKA evaluation of the expected dose deposition in the PMMA target (hatched area) compared to the x_{PMMA} data distribution (solid line). In the LNS data (left), the beam travels from right to left and the PMMA front face is at $x_{\text{PMMA}} = 2$ cm. In the GSI data (right), the beam travels from left to right and the PMMA front face is at $x_{\text{PMMA}} = (-6.15 \pm 0.02)$ cm.

Figure 4.43 shows an example of the reconstructed x_{PMMA} at the LNS (left) and GSI (right) experiments, both in the setup configuration at 90°, compared to the expected distribution (FLUKA MC) of the released dose in the target from the 80 MeV/u LNS ^{12}C beam and 220 MeV/u GSI ^{12}C beam, respectively. The x_{PMMA} distribution for the high energy beam (GSI) covers a wider range with respect to the low energy beam (LNS) as the beam path within the target is longer. Moreover, the rising edge of the x_{PMMA} distribution is related to the beam entrance position inside the PMMA, as can be observed in Figure 4.43 for the GSI beam energy (right). It is not possible to assess the same thing for the LNS x_{PMMA} distribution: the low energy ^{12}C beam (80 MeV/u) produces low energy secondary protons that suffers from a non negligible multiple scattering effect also in the first part of their path inside the target, broadening too much the emission profile distribution with respect to the beam entrance position in the PMMA.

Figure 4.44 shows how the beam penetration inside the PMMA is described by the x_{PMMA} and y_{PMMA} distributions from a dataset collected at the GSI laboratory in the angular configuration at 90° (the beam travels from left to right). The dashed vertical lines indicate the beam entrance position (left, $x^{BE}_{PMMA} = -6.45 \pm 0.02$ cm)

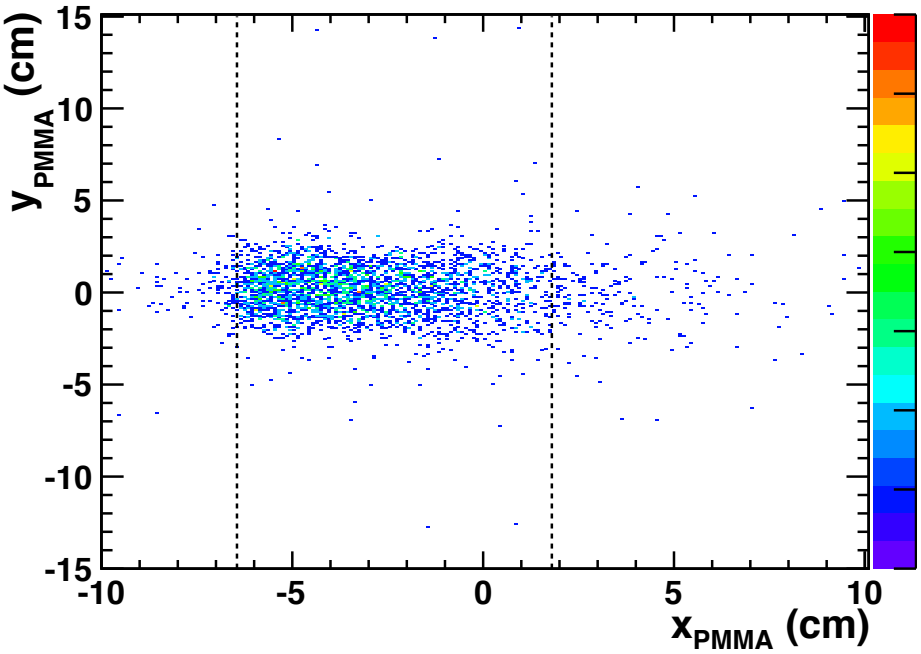

Figure 4.44. Distribution of the emission positions (x_{PMMA}, y_{PMMA}) of the secondary charged particles inside the PMMA for the angular configuration at 90° in the GSI experiment. The vertical dotted lines indicate the beam entrance position in the target (left) and the theoretical calculation of the Bragg peak position (right) for this particular dataset.

and the Bragg peak position determined from the FLUKA MC simulation (right, $x^{BP}_{PMMA} = 1.8 \pm 0.02$ cm).

Since a relationship between the BP position and the charged emission profile distribution has been found at the LNS experiment (see Figure 4.42), in the GSI experiment the aim was to provide a method to parametrize the emission shape and so the Bragg peak position, focusing on the falling edge of the charged particles emission profile. In order to do so a function $f(x)$ describing the GSI x_{PMMA} distribution has been built and the corresponding parameters have been evaluated, as shown in Figure 4.45:

$$f(x) = p_0 \frac{1}{1 + exp(\frac{x-p_1}{p_2})} \frac{1}{1 + exp(-\frac{x-p_3}{p_4})} + p_5 \ . \tag{4.24}$$

Parameters p_3 and p_1 are related to the rising and falling edge of the distribution, respectively, while p_4 and p_2 refer to the rising and falling slopes of the function. Parameter p_5 models the flat background contribution while p_0 is the normalization parameter. Handling the cases with a detection angle different from 90°, following the geometry of Figure 4.2, the function $f(x)$ has been convoluted with a beam shadow function given by a Gaussian with $\sigma \simeq \sigma_{\mathrm{beam}}/\tan(\theta)$. The profile function in equation 4.24 has been used to describe all the different isotopes (protons, deuterons,

tritons) profiles and all the data samples recorded with different geometrical conditions (PMMA positions, *i.e.* beam entrances) and angular configurations (60° and 90°).

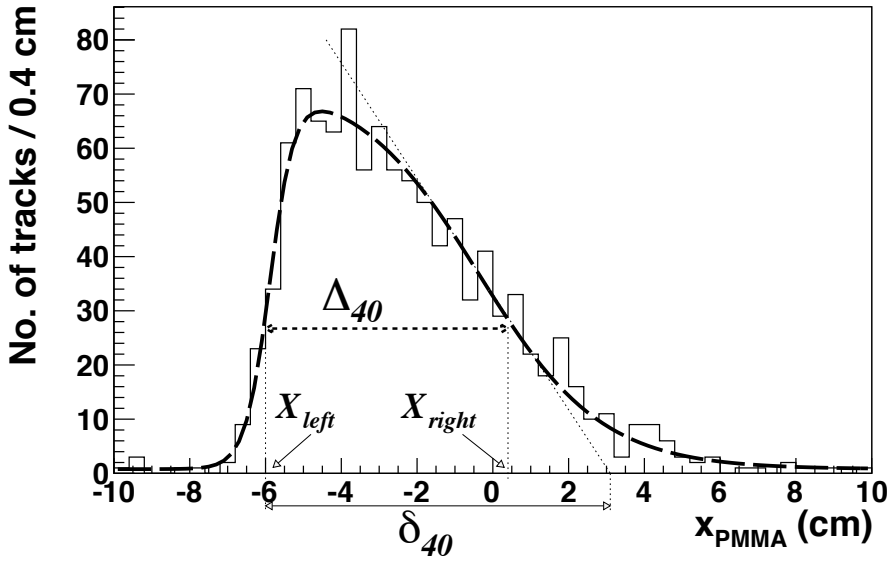

Figure 4.45. Distribution of the emission position inside the PMMA and along the beam line x_{PMMA} of the secondary charged particles for the GSI angular configuration at 90°. The beam entrance in this geometrical configuration is at ~ -6.15 cm. The PDF from eq. 4.24 is superimposed (dashed line). The dotted and solid arrows show the graphical representation of Δ_{40} and δ_{40}, respectively, as well as the variables X_{left} and X_{right}.

The proposed quantities characterizing the longitudinal charged emission profile that have been investigated in order to monitor the BP position are shown in Figure 4.45 as Δ_{40} and δ_{40}. Δ_{40} is the width of the $f(x)$ function at the 40% of its maximum with X_{left} and X_{right} the corresponding x coordinates at the rising and falling edge, respectively. Instead, δ_{40} is the distance between X_{left} and the x-intercept of the tangent to $f(x = X_{right})$.
The accuracy achievable with this measurements in monitoring the Bragg peak position is limited by several factors: the multiple scattering undergone by secondary charged fragments inside the phantom and the acquired statistics, as previously assessed, as well as the intrinsic fluctuations of the emission processes due to nuclear interactions.

The multiple scattering contribution is evaluated studying the transversal emission profile, *i.e.* the y_{PMMA} distribution, that is independent from the Bragg peak position inside the target (see Figure 4.42) and that represents the vertical component of the beam profile.

Figure 4.46 shows the measured (left) and simulated (right) distributions of the y_{PMMA} profiles, for the GSI 90° setup configuration.

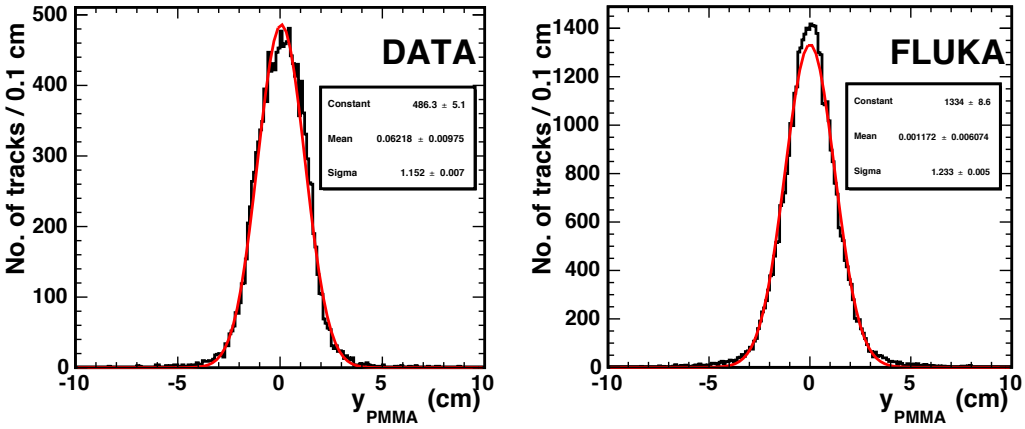

Figure 4.46. Measured (left) and simulated (right) vertical emission profile of secondary charged fragments inside the PMMA target for the GSI experimental configuration at 90°.

The resolution $\sigma_{y_{\mathrm{PMMA}}} = (1.152 \pm 0.007)$ cm of the y_{PMMA} data distribution is a convolution of several elements, as can be observed in the following equation:

$$\sigma^2_{y_{\mathrm{PMMA}}} = \sigma^2_{\mathrm{MS}} + \sigma^2_{\mathrm{beam}} + \sigma^2_{\mathrm{DCH}} \tag{4.25}$$

where $\sigma_{\mathrm{beam}} \simeq 1$ cm is the primary beam profile with $\sim 1\%$ relative uncertainty, σ_{MS} is the MS effect contribution and σ_{DCH} is the Drift Chamber tracking resolution. This latter contribution has been evaluated at the charged particle emission point (~ 40 cm far from the Drift Chamber centre) using the reconstructed charged track parameters covariance matrix and the single track resolution ($\simeq 200$ µm) measured at the Drift Chamber centre. The total Drift Chamber tracking resolution is $\sigma_{DCH} \sim 1.1$ mm. Therefore, the obtained value of the MS resolution is:

$$\sigma_{\mathrm{MS}} = \sqrt{\sigma^2_{y_{\mathrm{PMMA}}} - \sigma^2_{\mathrm{beam}} - \sigma^2_{\mathrm{DCH}}} \simeq 6 \text{ mm} \ . \tag{4.26}$$

In a real-case treatment scenario, the charged particle can traverse several centimeters of tissue thickness before exiting the patient, exceeding by a factor 3 or 4 the 2.5 cm of PMMA at the GSI experiment. Therefore, since σ_{MS} scales with the square root of the material thickness traversed by the particles, the contribution of the MS to the total resolution on a chosen parameter that has been evaluated from the x_{PMMA} distribution can increase up to a factor 2 with respect to the present measurement. However, if we take into account the measured kinetic energy spectra obtained with the 220 MeV/u GSI carbon ion beam that are shown in Figure 4.47, it is possible to select a sample with high energy (for example protons with $E_{\mathrm{kin}} > 100$ MeV) in order to reduce the multiple scattering effect on the secondary fragments inside the target.

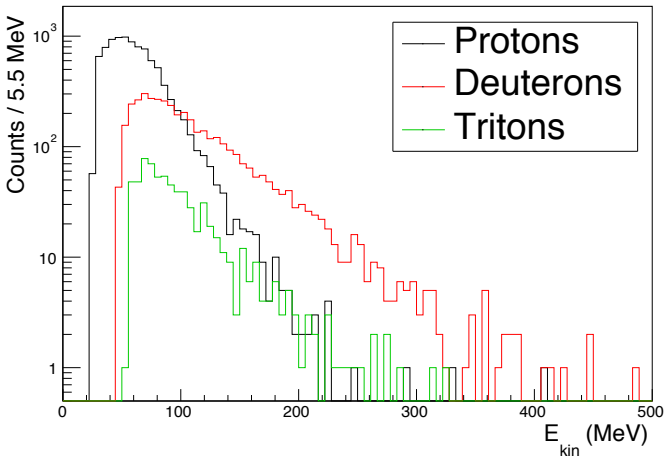

Figure 4.47. Measured kinetic energy of secondary charged fragments, such as protons (black), deuterons (red) and tritons (green), for the GSI experimental configuration at 90°.

The other limiting factor in the achievable resolution of a BP position monitoring technique is the secondary charged particles collected statistics that strongly depends on the delivered dose in a real treatment and on the detector geometrical acceptance. This contribution has been investigated choosing a fixed statistics (10^3) of detected fragments. For each angular configuration, data samples of 10^3 tracked charged fragments were used (13 samples at 90° and 100 samples at 60°) in order to measure the fluctuation of the corresponding values of Δ_{40} and δ_{40}. The beam spot size σ_{beam} has been taken into account for the Δ_{40} and δ_{40} comparison at different angular configurations. Table 4.2 reports the measured resolutions of Δ_{40}, δ_{40} and X_{left} parameters and the average values of Δ_{40} and δ_{40} that are related to the beam path inside the target ($\Delta_{\text{beam}} \simeq 8.3$ cm from FLUKA MC).

The reference sample of 10^3 charged fragments has been used as a reference sample collected in a standard treatment. It can be obtained using a $\Delta\Omega \simeq 10^{-3}$ sr detector solid angle, if $N_{\text{C}} \simeq 2.3 \times 10^8$ carbon ions hit the PMMA target, with the detector placed at 90° with respect to the beam direction. The same sample of 10^3 collected fragments can be obtained with $N_{\text{C}} \simeq 4.7 \times 10^7$ in the experimental configuration at 60°, according to the differential production rates measured in Section 4.4.3.

To make a comparison with a standard hadrontherapy treatment involving a carbon beam, considering a single pencil beam reaching the distal part of the tumor, where the performance of the dose monitoring technique is crucial, the carbon ions density is of the order of $10^7 - 10^8$ carbon ions per cm^3. Since in a full treatment there are many single pencil beams involved in order to cover all the tumor volume each beam adds its own contribution to the overall reconstructed emission shape, with its own emission pattern. Maximize the geometrical acceptance of the monitor device is then crucial in order to collect a satisfactory statistics for the desired tracks sample, minimizing the superimposition of different pencil beams impinging on different voxels.

As well as the Bragg peak position monitoring, the secondary charged particles detection can be exploited also for patient positioning monitoring, as mentioned before. For this purpose, the X_{left} parameter, whose accuracy is listed in Table 4.2, can be related to the beam entrance position in the patient, providing a fast and precise feedback on possible patient mispositioning during the treatment.

angle (deg)	σ_{Δ}(cm)	σ_{δ}(cm)	$\sigma_{X_{left}}$(cm)	$\overline{\Delta}_{40}$(cm)	$\overline{\delta}_{40}$(cm)
90	0.34	0.37	0.08	6.60 ± 0.09	9.40 ± 0.10
60	0.31	0.28	0.09	6.83 ± 0.03	9.44 ± 0.03

Table 4.2. Values and dispersions of the Δ_{40} and δ_{40} parameters. The resolutions (σ), for 90° and 60° experimental configurations, have been computed as the RMS of the delta distributions measured in the different beam entrance configurations and for different data samples.

In order to determine an indirect measurement of the Bragg peak position that can be actually used on-line, during real treatments, an extensive calibration campaign with different pencil beam energies, *i.e.* penetration depths, should be performed to validate the proposed monitoring technique.

4.4.5 Preliminary data from ^4He and ^{16}O ion beams

In the HIT experiment a preliminary analysis on the secondary charged radiation is ongoing, as well as the study on the prompt photon radiation described in Section 4.3.4. In Section 4.3.4, some details on the HIT experiment, as the setup geometry (see Figure 4.26), have been overviewed. It has to be remarked that at the HIT centre two different angular configurations with the LYSO detector and DCH placed at 90° and 60° have been investigated and helium and oxygen beams with different energies have been employed.
Since the Bragg peak has been kept in a constant position during the different data taking, several PMMA targets of different lengths (z_{PMMA}) have been used for each energy value and ion type (^4He,^{16}O), as shown in Table 4.3. The same analysis

^4He(MeV/u)	z_{PMMA}(cm)	^{16}O(MeV/u)	z_{PMMA}(cm)
120	7.65	210	7.65
125	10.0	300	12.65
145	12.65		

Table 4.3. Helium and oxygen beam energies with the corresponding PMMA target length.

described for the GSI data in Section 4.4.4 has been replicated for the beams and energies involved in the HIT experiment. Figure 4.48 shows the longitudinal emission profile (x_{PMMA}) of secondary charged particles for helium beams at different energies and in different setup configurations. The fit function described in equation 4.24 is superimposed (red solid line). As can be observed, the x_{PMMA} distribution, for each angular configuration, broadens with the increasing beam energy: beams with higher energies have a deeper penetration lengths inside the target. Therefore, the

longer is the beam range, the longer is the spatial emission of charged fragments in the longitudinal view.

The evaluation of the X_{left}, Δ_{40} and δ_{40} parameters outlined in Figure 4.45 is ongoing, and a table equivalent to Table 4.2 will be computed in order to assess the achievable resolution on the BP position with helium ions at different beam energy values. The production rate of secondary charged fragments will also be estimated. The same study for the oxygen beam is ongoing.

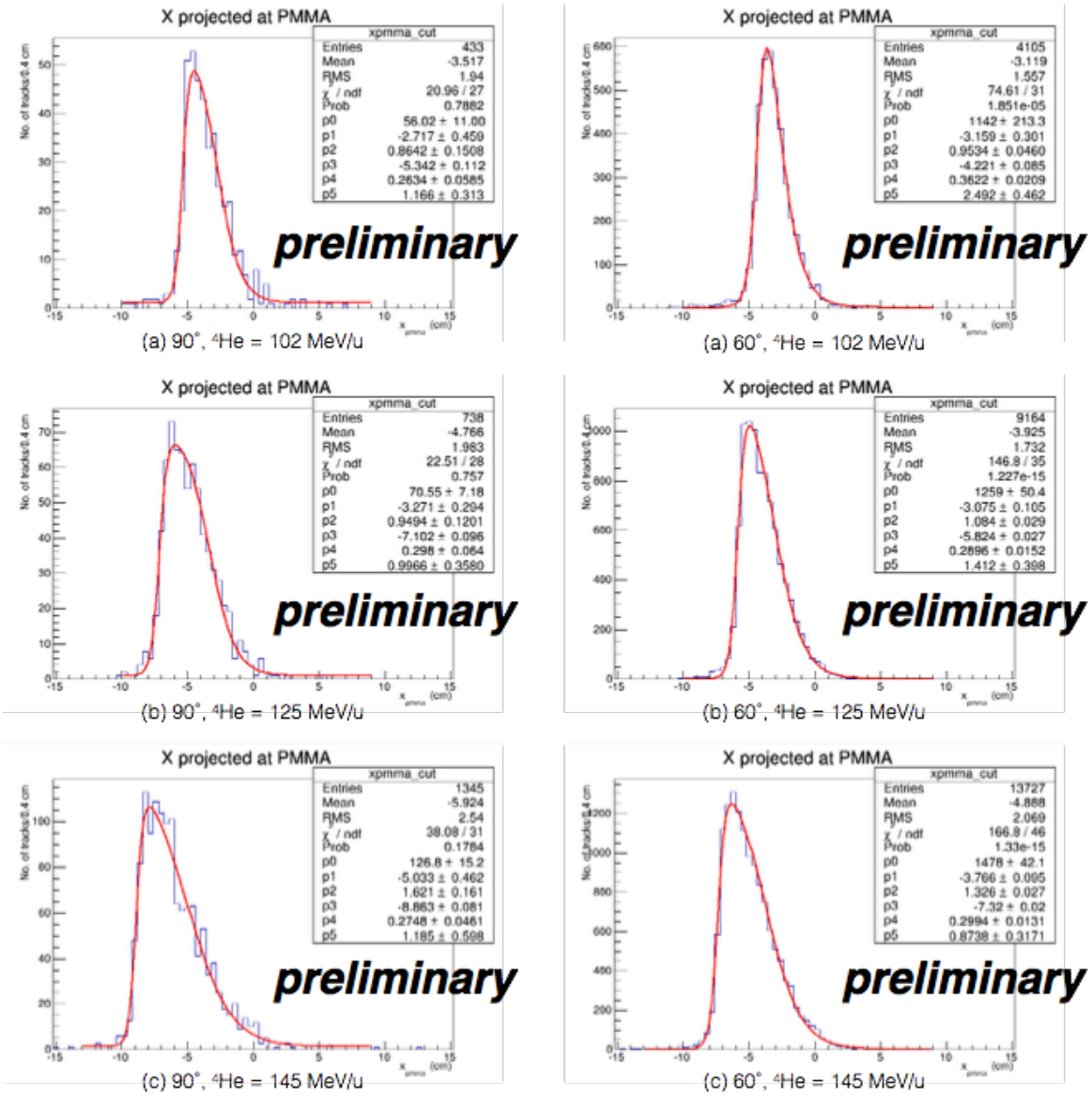

Figure 4.48. Secondary charged fragments emission profile for the HIT ^4He beam of different energies and in the angular configuration at 90° (left column) and 60° (right column).

Chapter 5

The Dose Profiler project

Nowadays, the off-line PET technique based on PET photons detection, described in Section 3.1.1, is the unique possibility of dose monitoring usually performed off-line, *i.e.* just after the treatment. No tools for a direct control of the beam range, *i.e.* on the Bragg peak position, have already been implemented in a clinical environment. Since the therapeutic hadron beam doesn't leave the patient, but it stops at the Bragg peak, secondary particles produced during the treatment must be used for a dose monitoring on-line, *i.e.* during the patient irradiation. Such secondaries can be PET photons, prompt photons, produced by the de-excitation of nuclei excited in the interactions between the hadron beam and the target, and secondary charged particles, mainly protons, produced by hadrons nuclear interactions with the traversed medium (see Chapter 3). In Chapter 4 the measurements performed on prompt photons within the $1 - 10$ MeV range and on secondary charged particles produced by a carbon ion beam impinging on a PMMA target have shown the possibility to rely on these particles for dose monitoring purposes. Prompt photons and secondary charged particles fluxes have been measured at large angles (90° and 60°) with respect to the primary beam direction, and a correlation between the secondary charged particles emission profile and the beam dose deposition inside the irradiated target has been observed.

Figure 5.1. Picture of a CNAO treatment room.

The performed measurements and the obtained results have led to the development of the project of a new device, named *Dose Profiler* (DP) based on the detection of both secondary neutral (prompt photons) and charged (mainly protons) radiation. Such device is under construction at the Scienze di Base Applicate per l'Ingegneria (SBAI) department of the Sapienza University (Roma, Italy) and in the next years it is foreseen to be tested in a treatment room of the CNAO centre, in Pavia. Figure 5.1 shows a picture of a CNAO treatment room, while Figure 5.2 is a 3-D reconstruction of the Dose Profiler possible use during a patient treatment at CNAO.

In this chapter it is presented the design of the dual-tracking device, the Dose Profiler, capable to on-line monitor the beam released dose through the simultaneous detection of prompt photons and secondary charged particles produced by the beam. The two-fold nature of this single detector is a unique feature that will allow to maximize the information on the dose deposition. This feature aims to overcome the eventual low statistics of prompt gammas and charged secondaries detected during a standard treatment session, with a 2 Gy per fraction dose delivery[1]. Geometrical parameters as acceptance and the detection angle of the DP should be carefully chosen in order to maximize the collected statistics in the boundary condition of the actual treatment rooms.

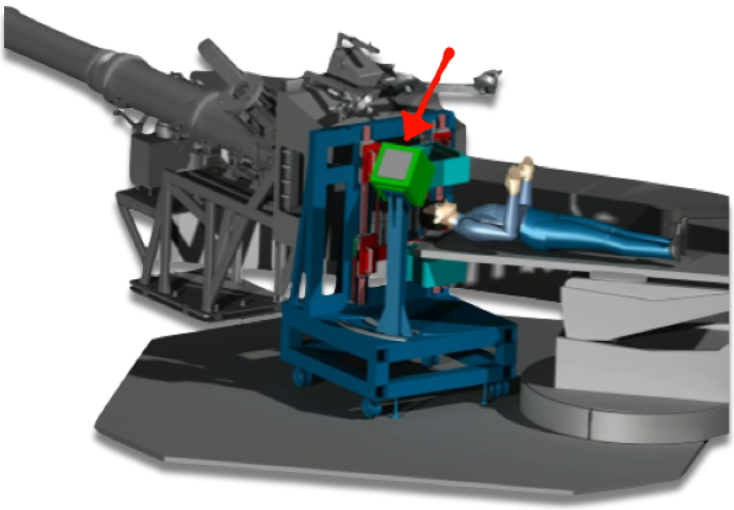

Figure 5.2. Reconstruction of the Dose Profiler employment during a patient treatment at CNAO (Pavia, Italy). The device is indicated with a red arrow.

To take into account all the issues reported in Section 4.1 that affect the device resolution (as the beam halo contribution to the accuracy on the emission shape determination of secondary charged particles), the Dose Profiler will be mounted on a structure that will allow the device to cover detection angles between $60° \div 90°$ with respect to the primary beam direction.

[1]In the PT hypofractionation, a dose of $5 \div 10$ Gy/$fraction$ can be delivered, improving the produced secondary fragments statistics.

In Section 5.1, the detector operation principles are overviewed and the detector main components are described. In Section 5.2 and 5.3, the FLUKA Monte Carlo simulation used to optimize the detector design and to evaluate the detector expected response is presented as well as the reconstruction algorithm to track prompt photons and protons. The last section is dedicated to the Dose Profiler performances in terms of the achievable spatial resolution on the reconstructed emission point of prompt photons and secondary protons.

5.1 Detector overview

The Dose Profiler has been designed to operate simultaneously as a charged particle and neutral radiation tracker. Such charged particles are mainly protons with kinetic energy $E_{kin} > 50$ MeV, coming from the target (and projectile, for heavy charged ion beams) nuclear fragmentation (see Section 1.1.3, 2.4.1 and 3.1.3). The neutral radiation, prompt gammas with energies ranging between $1 \div 10$ MeV, arises from the nuclear de-excitations (see Section 3.1.2). Therefore, a Compton camera could reconstruct the prompt gamma incoming direction, tracking Compton electrons ($1 \div 10$ MeV photons undergo mainly Compton scattering on low Z materials, see Section 1.3.2 and 3.1.2). Figure 5.3 shows a scheme of the detector: six planes of scintillating fibers with orthogonal views (in the XY plane) compose the tracker, a plastic scintillator (in cyan) absorbs low energy electrons while the energy deposit information is provided by a calorimeter of pixelated LYSO crystals (in red).

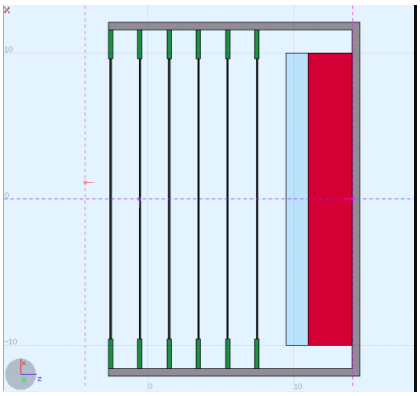

Figure 5.3. Scheme of the Dose Profiler layout (longitudinal view): six tracking planes (black), front-end electronic frames (green), electron absorber (cyan), LYSO calorimeter (red) and detector case (gray).

Figure 5.4 shows the principle of the DP dual operation mode. The tracker layers (green), the absorber (blue) and the LYSO calorimeter (grey) are shown. A prompt gamma (γ) interacts with a tracker plane where the Compton scattering occurs. A charged track from the scattered electron (e^-) with an energy deposit in the electron absorber and an energy deposit in the calorimeter due to the scattered photon (γ') characterize the prompt gamma event (left). Instead, the secondary charged particle event (right) can be identified by an almost linear track and a high energy deposit in the calorimeter, having a reconstructed position related to the

track, as the secondary charged particle passes through the tracker layers without suffering from a large multiple scattering effect (since the low scintillating fibers thickness) and releasing almost all its energy in the pixelated calorimeter.

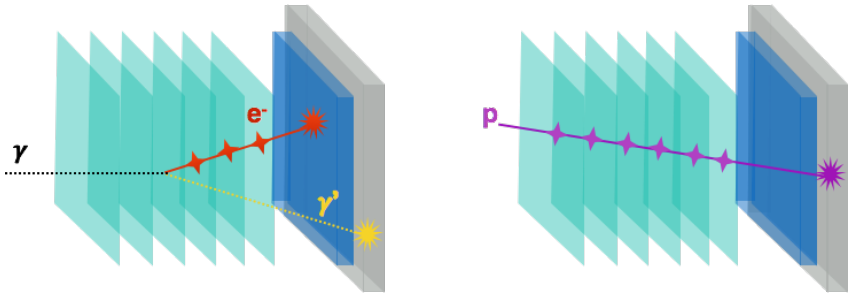

Figure 5.4. Characterization of a prompt photon event undergone by Compton interaction in the tracker (left) and secondary charged particle (*e.g.* proton) event (right) (not to scale).

5.1.1 The tracker

The tracker is composed by six planes each made by two orthogonally placed scintillating fiber layers (384 fibers each) to provide an XY bi-dimensional view. The planes dimensions, spacing, thickness and materials have been optimized using Monte Carlo simulations in order to maximize the detector geometrical acceptance and the Compton scattering cross section for prompt photon events, and to control the multiple scattering contribution to secondary charged particles trajectories. Square 0.5×0.5 mm^2 scintillating fibers (Saint-Gobain single-cladding BCF-12) have been chosen, with the minimal plane separation (2 cm) allowed by fibers front-end electronics readout in order to increase the geometrical acceptance and the compactness of the detector. The readout will be performed by means of 1×1 mm^2 silicon photomultipliers (SiPM Hamamatsu S12571 – 050P) hosted on the same FR-4 board (4 cm wide) that supports the front-end (FE) electronics. Each SiPM will be coupled with two adjacent fibers of the same layer. Due to the lateral dimension of the SiPM case (1.9 mm), couple of fibers are alternatively read from the two fibers ends (96 SiPMs on one side and 96 SiPMs on the opposite side). The total detector sensitive area is of 19.2×19.2 cm^2 read by 192 channels per layer. For each front-end board $96 + 96$ SiPM of two contiguous planes are read by 6 custom integrated chip (BASIC32_ADC). Since the adopted BASIC32_ADC readout ASIC has 16 input channels per side, the compactness of the device requires that each FE board manages 192 double fibers of one plane and 192 double fibers of the contiguous plane. On top of the FE "analogical" board, a digital one is used to produce the SiPM HV to distribute the trigger signal and to send data to a further concentrator board. The design of the tracker and its electronic read out are shown in Figure 5.5 (a) and (b), respectively. Considering the tracker geometrical and physical characteristics, and also the electronic read out system, the expected spatial single hit resolution is ~ 300 µm while the hit energy resolution is expected to be $\sim 9\%\sqrt{(E(\text{MeV}))}$, compatible with the preliminary SBAI laboratory measurements on a Minimum Ionizing Particle (MIP). Therefore, the expected fibers energy resolution is $\sim 20\%$ for a Compton electron and $\sim 10\%$ for a proton.

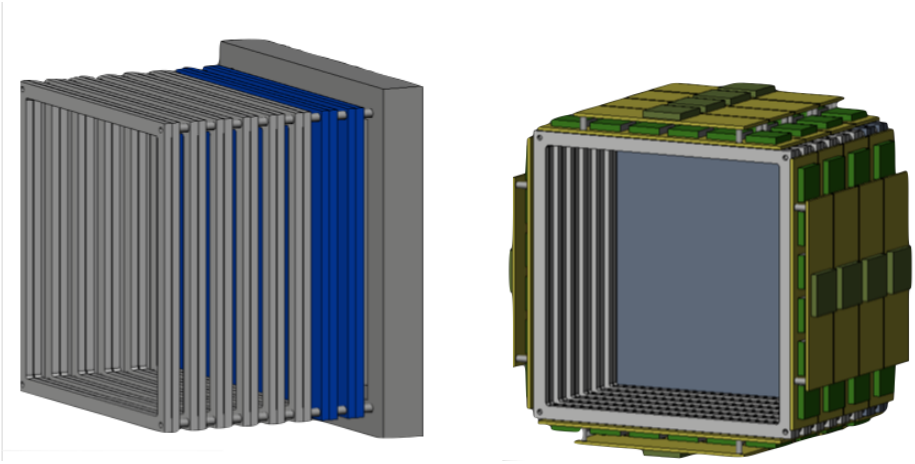

(a) (b)

Figure 5.5. Mechanical drawings of the profiler. The six scintillating fibers planes (grey), the two electron absorber plane (blue) and the final calorimeter box (grey) are shown (a). The fibers and electron absorber planes are drawn together with their electronic read out (b).

5.1.2 The electron absorber

In order to prevent any Compton electron from reaching the calorimeter and its back-scattering from the LYSO crystal to the tracker, deteriorating the pattern recognition, a plastic scintillator (Eljen EJ-200) made of polystyrene has been placed at a distance of 2 cm after the tracker. Due to its low atomic number ($Z_{eff} = 3.5$), the polystyrene drastically reduces the amount of back-scattered electrons with respect to a situation where there is only the LYSO calorimeter after the tracker. To avoid the development of a dedicated readout subsystem, the front-end board of a fiber plane is also used to read the electron absorber. For this reason, the absorber is made of 4 independent slabs ($2 + 2$), for total dimensions of the plastic scintillator volume of $21.2 \times 21.2 \times 2.4$ cm^3. The design of the electron absorber and its electronic read out are shown in Figure 5.5 (a) and (b), respectively. As evaluated for the tracker, the electron absorber expected energy resolution is $\sim 11\%\sqrt{(}E(\text{MeV}))$.

5.1.3 The calorimeter

The calorimeter is a 4×4 matrix of pixelated LYSO crystals (see Table 4.1), $5 \times 5 \times 2$ cm^3 each (Hamamatsu LFS 16×16 pixels matrix). The active volume of the calorimeter is $20 \times 20 \times 2$ cm^3. Such pixelated crystals can be used in order to weight secondary charged particles tracks according to their kinetic energy (assigning a higher weight to harder particles that suffer less the multiple scattering effect) and to reconstruct the Compton photon direction (see Section 5.3). The high LYSO atomic number ($Z_{eff} = 66$) allows a compact design together with an expected energy resolution of $\sim 9\%/\sqrt{(}E(\text{MeV}))^2$. The pixel layout allows to insulate the photon position in the transverse plane, although loosing the depth of interaction

[2]The energy resolution of the LYSO calorimeter has been computed from SBAI laboratory measurements, using a pixelated LYSO crystal with a non dedicated electronic read out different from the one that will be used in the DP calorimeter construction.

reconstruction capability. The crystal readout will be performed by means of Multi Anode Photo-Multiplier Tube (Hamamatsu MAPMT H8500). The 4×4 scintillator blocks are mechanically contained in a square aluminum structure 2 cm thick, 3 cm wide, also used to sustain the tracker and the electron absorber on the front and to house, on the back, the MAPMT, the acquisition board (based on BASIC32_ADC ASIC) and the data concentrator.
The Dose Profiler calorimeter and the aluminum case structure are shown in Fig 5.6.

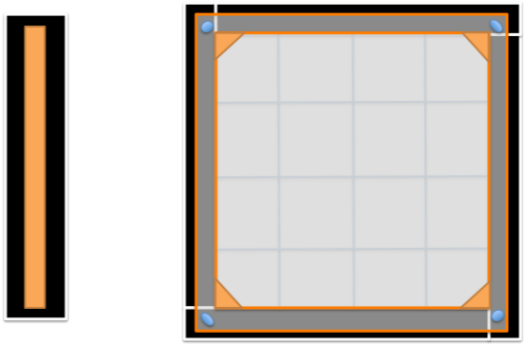

Figure 5.6. LYSO calorimeter: lateral view (left) and front view (right).

5.2 Simulation

A detailed simulation of the detector has been developed in order to optimize its design. The Monte Carlo software used for the Dose Profiler simulations is FLUKA, release 2011.2 (*Ferrari et al.* [7], *Böhlen et al.* [65]). The Monte Carlo data have been organized in ROOT-trees (*Brun et al.* [67]) mirroring the foreseen DAQ output format. Some detector geometrical parameters are summarized in Table 5.1.
When running a simulation, in order to score an event, a realistic trigger condition must occur: at least three tracking planes must be fired or an energy release of $E_{rel} > 100$ keV must be detected inside the electron absorber or in the calorimeter. The quenching effect of the scintillators has been included in the Monte Carlo according to *Koba et al.* [66].

Component	**Thickness (cm)**	**Material**	**Density (g/cm^3)**	**Zeff**
Printed circuit boards (4)	0.4	FR-4	1.70	4.3
Fibers planes (6)	0.05	polystyrene	1.05	3.5
Tracker frames (6)	1.2	aluminum	2.70	13
Electron absorber (4)	2.4	polystyrene	1.05	3.5
Calorimeter frame (1)	3.0	aluminum	2.70	13
Calorimeter (1)	2.0	LYSO	7.40	66

Table 5.1. Dose Profiler components, materials and geometrical parameters.

5.3 Event reconstruction and analysis

In order to reconstruct the prompt photon or proton incoming direction, the expected event has to be characterized: the probability of having a Compton interaction with at least three scintillating fiber planes hit and an energy deposition from the scattered photon in the LYSO calorimeter is $\sim 0.1\%$ in the energy range of interest, while protons interacts in all the crossed fiber planes. Charged tracks are reconstructed with a track finding algorithm that starts from deposits in the fibers grouped together to form 3-dimensional clusters, while prompt photons are reconstructed starting from the light pattern in the pixelated LYSO crystal.
The software for the data analysis has been developed in C/C++ and has been directly interfaced with ROOT.

5.3.1 Event selection

Compton and proton events are distinguished on the basis of the number of tracker planes hit by the simulated particle and of the energy deposit in the electron absorber.

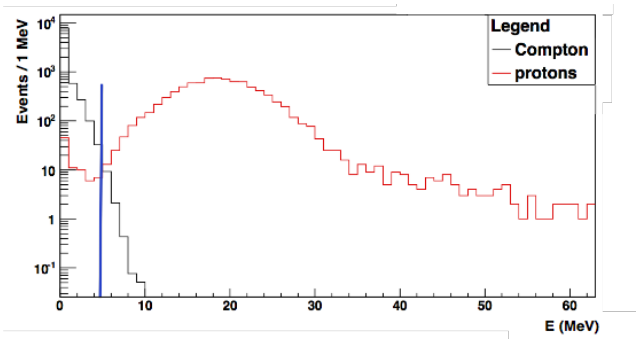

Figure 5.7. Energy deposit in the plastic scintillator for Compton events (black histogram) and proton events (red histogram). The vertical blue line indicates the energy cut for the event selection.

Figure 5.7 shows the distribution of the energy release in the electron absorber from the Monte Carlo simulation. Events with an energy deposit $E > 4.5$ MeV are taken into account as protons, while for $E < 4.5$ MeV a Compton event is considered. This cut is almost 100% efficient on proton events while the efficiency on the Compton event selection is 0.26%. Considering the tracker planes hit selection, a proton event has been selected if the number of planes hit is $nhit \geq 6$, while a Compton event has been taken into account if $3 \leq nhit < 6$. The efficiency of this selection is $> 99\%$ for protons and $\sim 0.5\%$ for Compton events.
An additional help for prompt photon event reconstruction could come from the detection of electron-positron pairs produced in the photon-tracker interaction (see Section 1.3.3). This contribution is negligible for low energy photons. Figure 5.8 shows the percentage comparison of Compton events (blu) and pair production events (red) as a function of prompt photon initial energy. Pair production events are not classified nor analyzed in the simulation yet and contaminate by $\sim 20\%$ the Compton sample.

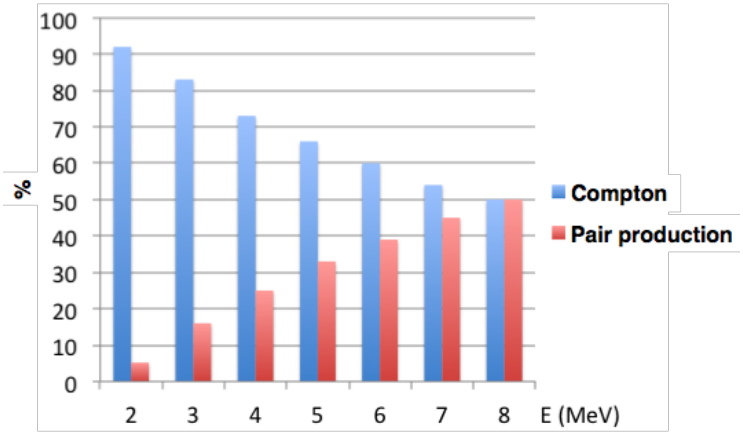

Figure 5.8. Percentage comparison of Compton events (blu) and pair production events (red) as a function of prompt photon initial energy.

5.3.2 Track reconstruction

In order to reconstruct the track in the fiber planes from a Compton electron or a proton event, fiber hits[3] in the X and Y transverse coordinates are clustered separately by grouping consecutive hits to form 2-dimensional clusters (XZ and YZ views) being Z the coordinate along the longitudinal detector axis. The Z coordinate of the cluster is given by the middle position of the fiber plane while the X and Y coordinates are given by the average spatial coordinate of two consecutive fibers belonging to the same layer, read out by the same SiPM channel. 3-dimensional (3D) clusters are then formed taking all the possibile combinations of X and Y clusters in a Z plane. It should be noticed that in Compton events about half of the times the primary photon interaction occurs in the second fiber layer of a plane so in these cases a 3D cluster cannot be built.
Track candidates are found using a *track finding* algorithm, starting from the list of 3-D clusters as it is illustrated in Figure 5.9. The track finding algorithm procedure can be summarized as follows:

- starting from the first fiber layer hit, track segments (*seeds*) are built considering all the hits combination in the first two adjacent planes ($s1$, $s2$, $s3$ in Figure 5.9);
- each seed is linearly extrapolated to the subsequent plane;
- the hit that minimizes the distance between the expected position (computed by prolonging the seed in the previous step) and the measured position (black star in the figure) is clustered to the corresponding seed;
- once the last plane is reached, a list of track candidate is built.

After the track finding algorithm has been applied, a *track fitting* procedure has been developed. The track candidates are first linearly parametrized and a χ^2 fit is performed in order to obtain a first estimation of the track parameters. If $nhit < 6$, the track angular coefficients (for the X and Y coordinates) obtained with

[3] A hit is an energy deposit on a fiber greater than 40 keV.

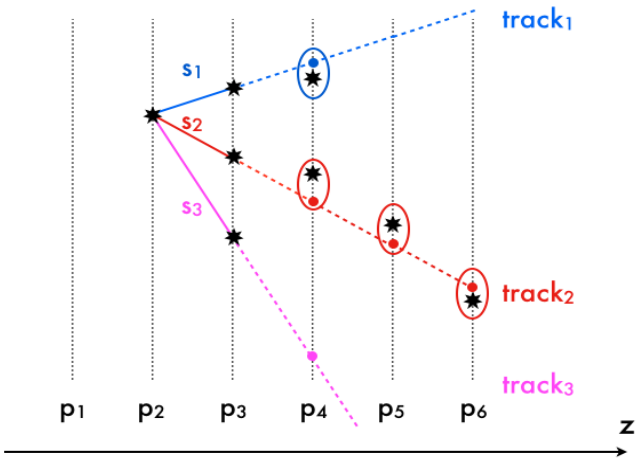

Figure 5.9. Scheme of the track finding algorithm.

the linear fit are then passed to a Kalman filter(*Kalman* [72], *Kalman and Bucy* [73]). The Kalman filter takes into account the multiple scattering effect undergone by Compton electrons in the detector tracker material (scintillating fibers), and it consists of a three step process: *prediction*, *filtering* and *smoothing*. The prediction process starts at the first fiber hit and it predicts the location of the next hit in the subsequent plane, until the end of the track is reached. Then the "filter" corrects the predicted track parameters using the measurement of the hit coordinates. The "smoother" traces back the hits from the track end to the beginning, refining the track parameters at each step using the information from the previous hit, which in the smoothing procedure corresponds to the kinematically subsequent.

5.3.3 Prompt photon reconstruction

Photons reconstruction algorithm is applied only on events that are classified as Compton events, following the event selection procedure described in Section 5.3.1. The position of the scattered Compton photon in the XY plane is reconstructed using the center of gravity (CG) of the occupancy distribution obtained from the MAPMT read-out of the pixelated LYSO crystal:

$$CG = \frac{\sum_{i,j=1}^{n} N_{ij} \cdot r_{ij}}{\sum_{i,j=1}^{n} N_{ij}} \,. \tag{5.1}$$

N_{ij} is the number of optical photons in a single pixel and r_{ij} is the pixel coordinate in the XY plane (the i/j index is relative to the row/column of the pixelated LYSO matrix). The position along the z-axis is assumed to be half of the LYSO crystal thickness.

After the direction of the scattered photon and Compton electron have been reconstructed (see Section 5.3.2), using the information on the deposited energy in the electron absorber and in the LYSO calorimeter of the Compton electron and scattered photon, respectively, some considerations on the momentum unit vectors have been taken into account in order to evaluate the production point of the incoming prompt

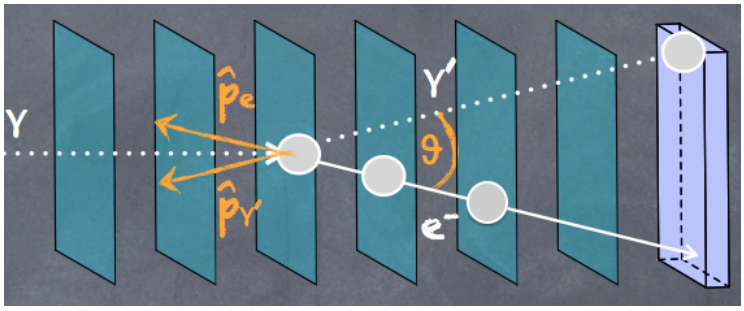

Figure 5.10. Scheme of a Compton event: the scattered photon and Compton electron are outlined, as well as their reconstructed momenta unit vectors ($\hat{p_{\gamma'}}$ and $\hat{p_e}$ respectively). θ is the angle between the scattered photon and Compton electron direction.

photon. Figure 5.10 shows the kinematic of a Compton event, where the primary prompt photon is γ, γ' and e^- are the scattered photon and Compton electron, while $\hat{p_{\gamma'}}$ and $\hat{p_e}$ are their respective reconstructed momentum unit vectors and θ is the angle between the scattered photon and the Compton electron direction. Assuming the initial electron at rest, the momentum conservation can be written as:

$$\vec{p_\gamma} = \vec{p_{\gamma'}} + \vec{p_e} \tag{5.2}$$

that can be rewritten as follows

$$\hat{p_\gamma} = c_1 \hat{p_{\gamma'}} + c_2 \hat{p_e} \tag{5.3}$$

with the coefficients c_1 and c_2 defined by:

$$c_1 = \frac{|\vec{p_{\gamma'}}|}{|\vec{p_\gamma}|}; \qquad c_2 = \frac{|\vec{p_e}|}{|\vec{p_\gamma}|} \ . \tag{5.4}$$

The normalization condition is:

$$c_1^2 + c_2^2 + 2c_1c_2\cos\theta = 1 \ . \tag{5.5}$$

Therefore, once the direction of the scattered particles is known, it is possible to reconstruct the direction of the primary photon using the mean values of c_1 and c_2 distributions obtained from the Monte Carlo simulations ($\bar{c}_1 = 0.45$, $\bar{c}_2 = 0.69$). The reconstructed unit vector $\hat{p_\gamma}$ is then evaluated from the track vertex backward to the patient position and imaging reconstruction techniques will be used.
The described algorithm based on the evaluation of the c_1 and c_2 coefficients can be used to evaluate the incoming prompt photon direction in a first approximation.

5.3.4 Proton Reconstruction

Once that an event is classified as a proton event according to the event selection described in 5.3.1, the track is extrapolated from the first hit fiber plane to the target position, following the track finding algorithm described in Section 5.3.2. Afterwards, imaging reconstruction techniques will be used as for prompt photon events reconstruction.

5.4 Performances

In this section, the results from the FLUKA Monte Carlo simulation developed in order to evaluate the Dose Profiler performances for the on-line dose monitoring purpose are presented. The obtained spatial resolution on the emission position of reconstructed prompt photons from Compton events, as well as for reconstructed protons, is provided.

5.4.1 Performances on Compton events

A dedicated FLUKA simulation has been developed in order to evaluate the detector performances in terms of spatial resolution on the reconstructed primary prompt photons emission point. A prompt photons point-like source has been placed 30 cm before the first tracking plane, where it is expected to operate, aligned with its longitudinal axis (z) and centered with respect to the other two coordinates (x,y). The source emits photons in the first tracking plane solid angle of ~ 0.4 sr, while the LYSO calorimeter solid angle is ~ 0.2 sr. The simulated prompt photons energy spectrum has the same shape of the one measured from an 80 MeV/u carbon ion beam impinging on a PMMA target, described in Section 4.3 from *Agodi et al.* [53] [54] measurements (see Figure 4.19). Compton events have then been selected with the selection criteria outlined in Section 5.3.1. In the simulation, a 20% energy resolution has been assumed for the fibers, a 25% for the plastic scintillator (electron absorber), while a 7% energy resolution has been assumed for the LYSO calorimeter (actually, these energy resolution values are worst with respect to the one expected, see Section 5.1).

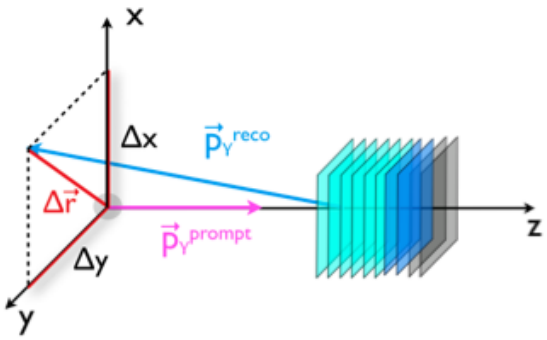

Figure 5.11. Scheme of the reconstructed ($\vec{p}_{\gamma^{reco}}$) and true ($\vec{p}_{\gamma^{prompt}}$) directions of the incoming prompt photon, defining the error vector $\Delta\vec{r}$.

Once the reconstructed direction of the incoming prompt photon ($\vec{p}_{\gamma^{reco}}$) has been evaluated following the track reconstruction process for a Compton event presented in Section 5.3.2, $\vec{p}_{\gamma^{reco}}$ is projected on the XY plane where the prompt photon source has been placed (30 cm before the first tracker plane). $\vec{p}_{\gamma^{prompt}}$ is the true direction of the incoming prompt photons. Thus, the error vector $\Delta\vec{r}$ is the distance between the true and reconstructed prompt photon production point, as shown, for example, in Figure 5.11, defined by the following equation:

$$|\Delta\vec{r}| = \sqrt{\Delta x^2 + \Delta y^2}\ . \tag{5.6}$$

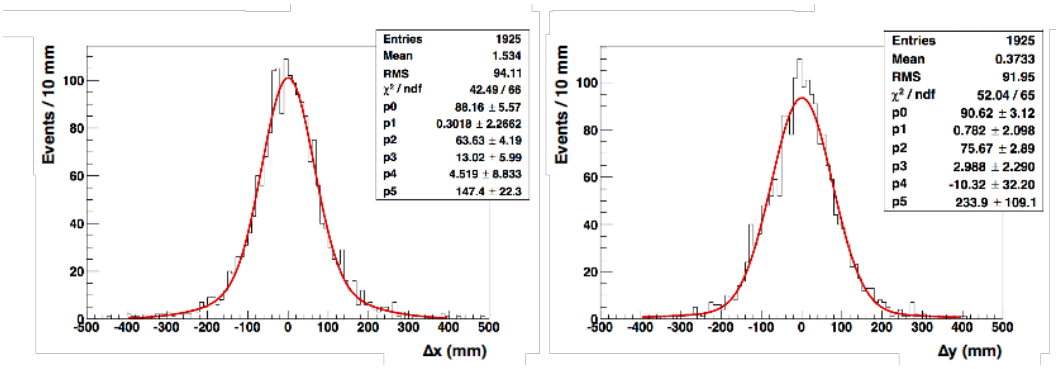

Figure 5.12. Δx (left) and Δy (right) distributions of a single reconstructed prompt photon production point.

Therefore, the width of the $\Delta\vec{r}$ distribution is the detector spatial resolution for single reconstructed photons. Figure 5.12 shows the obtained Δx (left) and Δy (right) distributions used to extract the spatial resolution on the X and Y coordinates of a single reconstructed prompt photon. The spatial resolution on a single prompt photon event reconstructed is $RMS \sim 9$ cm. The dominant contributions to the resolution are the electron momentum resolution (multiple scattering, ~ 50 mm) and the use of the c_1c_2 method (~ 50 mm). Other contributions come from the photon momentum resolution (~ 15 mm) and the neglected electron momentum in the nucleus (~ 8 mm).
Taking into account the total sample of reconstructed prompt photons (1925 events), the spatial resolution on the X and Y coordinates is $\frac{9 \text{ cm}}{\sqrt{1925}} \sim 2$ mm.

In order to evaluate the spatial resolution of the reconstructed prompt photon emission point expected in a real treatment, the average number of emitted photons (N_γ^{ave}) from the irradiation of a tumor slice with a dose of n Gray in a real carbon ion therapy treatment can be computed:

$$N_\gamma^{ave} = n[\text{Gy}] \cdot \frac{dN_C}{slice \cdot \text{Gy}} \cdot \Phi^\gamma(\Omega) \cdot \Omega \, . \tag{5.7}$$

Considering a delivered dose $n = 2$ Gy, the second term of eq. 5.7 can be obtained from *Krämer et al.* [74] and it is $3 \cdot 10^7 \frac{^{12}C}{slice \cdot \text{Gy}}$. A prompt photons flux $\Phi^\gamma(\Omega) = 2.32 \cdot 10^{-3} \frac{N_\gamma}{^{12}C \cdot sr}$ has been evaluated by *Agodi et al.* [53] [54] (see Section 4.3.2), while the detector solid angle is $\Omega = 0.22$ sr.
Therefore:

$$N_\gamma^{ave} = 2 \text{ [Gy]} \cdot 3 \cdot 10^7 \left[\frac{^{12}C}{slice \cdot \text{Gy}}\right] \cdot 2.32 \cdot 10^{-3} \left[\frac{N_\gamma}{^{12}C \cdot sr}\right] \cdot 0.22 \, [sr] =$$

$$\sim 30600 \left[\frac{N_\gamma}{slice}\right] \, .$$

From the MC spatial resolution on a single prompt photon event, the expected spatial resolution of the reconstructed prompt photons emission point in a real treatment is $\sim$ 1 cm. This result is strongly dependent on the dose delivered to the tumor and on its geometry and hence it has to be considered only as an indicative result. Moreover, improving the method of reconstruction of the prompt gamma incoming direction, including in the c_1, c_2 algorithm (see Section 5.3.3) other kinematics variables as the informations on the energy deposition in fibers, in the electron absorber and in the calorimeter, the expected resolution on the reconstructed prompt photon emission point can increase.

5.4.2 Performances on proton events

In order to measure the detector performances on proton events, a FLUKA Monte Carlo simulation has been modeled, schematizing a patient head by a sphere of 10 cm radius, with an outer ring 1 cm thick made of cortical bone and the inner made of brain (ICRU [20] certified materials).

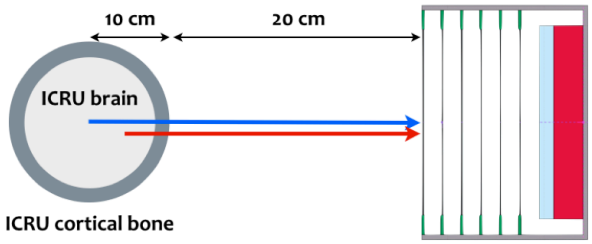

Figure 5.13. Simulated setup for proton performances evaluation, described in the text.

The simulation has been performed using two proton sources, one placed in the center of the brain sphere (blue arrow) and the other placed at 5 cm from the center (red arrow), as shown in Figure 5.13. In this way, two clinical scenarios have been reproduced: a worst case where the tumor is located exactly in the center of the patient head, and an intermediate case where the tumor is closer to the patient cortical bone. The initial protons kinetic energy has been varied between 75 MeV and 250 MeV for the centered source and between 70 MeV and 140 MeV for the displaced source. Figure 5.14 shows the results of the percentage number of protons reaching the Dose Profiler (N_{p}) as a function of the initial proton kinetic energy for the two simulated source configurations. As expected, a clear energy threshold effect is present for charged particles detection: once the energy threshold is exceeded, protons can escape from the patient head and can be tracked with high efficiency. For the detector performance results, the proton beam kinetic energy values lower than 80 MeV and 120 MeV respectively for the source placed at 5 cm and 10 cm inside the patient head have not been considered.

In order to obtain the spatial resolution on tracked proton events, the same procedure described for Compton events in Section 5.4.1 has been followed. From a gaussian fit to the proton's Δx and Δy distributions, the resolutions in the X and Y coordinates on a single reconstructed proton emission point, for the two

different geometrical configurations of the source and for several initial protons kinetic energies, have been evaluated.

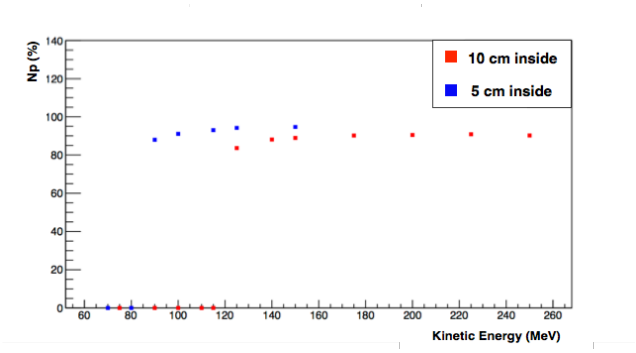

Figure 5.14. Percentage number of protons reaching the Dose Profiler for the simulated proton source in the two geometrical configurations as a function of the protons initial kinetic energy. An energy threshold is present for charged particles: the produced secondary proton has to exceed such threshold in order to exit the patient head and be detected.

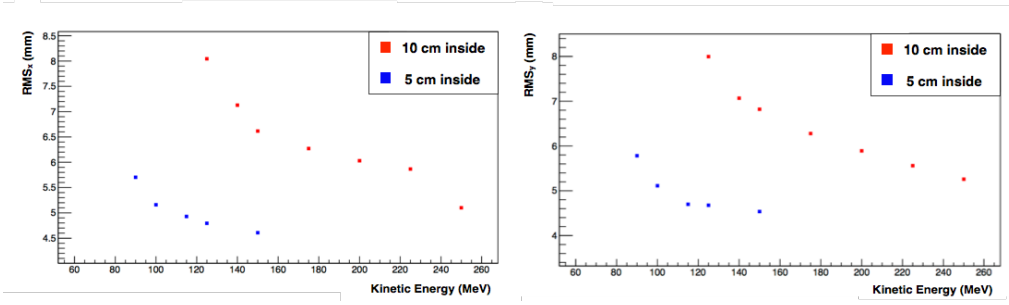

Figure 5.15. Detector spatial resolution on the X (left) and Y (right) coordinates of a single proton reconstructed emission point, for the two source geometrical configurations.

The obtained results are shown in Figure 5.15: for both source positions, RMS_x (left) and RMS_y (right) have values between $4 \div 8$ mm. The better spatial resolution on a single proton event is achieved for high kinetic energies in both source position configurations but the best value is reached for the source closer to the cortical bone. In fact, high energy charged particles suffer less the multiple scattering effect which is the main contribution to the spatial uncertainty in protons track reconstruction (see Section 1.2.2). Moreover, the MS is lower for charged particles traversing smaller path inside tissues (as for the source in the 5 cm inside configuration with respect to the 10 cm inside one).

In order to evaluate the spatial resolution of the reconstructed proton emission point expected in a real treatment, the average number of emitted protons (N_P^{ave}) has been computed following the same procedure described for prompt photons, using equation 5.7.

Including the proton flux $\Phi^P(\Omega) = 2.14 \cdot 10^{-5} \frac{N_P}{^{12}C \cdot sr}$ computed by *Agodi et al.* [60] [61] (see Section 4.4.3):

$$N_P^{ave} = 2\ [\text{Gy}] \cdot 3 \cdot 10^7 \left[\frac{^{12}C}{slice \cdot \text{Gy}}\right] \cdot 2.14 \cdot 10^{-5} \left[\frac{N_P}{^{12}C \cdot sr}\right] \cdot 0.22\ [sr] =$$

$$\sim 280 \left[\frac{N_P}{slice}\right]$$

and therefore, the expected spatial resolution of the reconstructed protons emission point in a real treatment, for protons produced with a kinetic energy of 140 MeV, is ~ 0.4 mm.

Conclusions

This thesis documents the work done to implement a novel on-line dose monitoring technique to be applied in particle therapy treatments. The first research was the study of the secondary radiation produced in the interactions of hadron beams of therapeutical energies with PMMA phantoms. Experimental data have been collected in order to characterize the production of secondary fragments such as prompt photons and charged particles, from 80 MeV/u and 220 MeV/u carbon ion beams. Preliminary results obtained using helium and oxygen beams were also reported. Secondary charged particles have been measured for the first time at large angles (90° and 60°) with respect to the beam incoming direction and a technique based on the reconstruction of the secondary charged fragments emission profile has been developed in order to relate such profile to the Bragg peak position. A clear correlation between the charged particles emission profile falling edge and the BP position inside the target has been observed and two parameters characterizing the charged profile have been proposed to monitor the maximum dose release. The spatial resolutions obtained on such parameters are of the order of $\sim 3-4$ mm, detecting the charged particles in a solid angle $\Omega \sim 2 \times 10^{-3}$ sr and using a drift chamber for tracks reconstruction. Moreover, the correlation between the rising edge of the charged fragments emission distribution and the beam entrance position inside the target has been proved: a parameter describing the distribution rising edge that could be used as a variable to monitor on-line the patient positioning has been identified with a spatial resolution of $0.8-0.9$ mm. No dependency from the charged fragments kinetic energy has been observed for the emission profile, so the resolution on the reconstructed emission distribution, that is related to the beam range, will not vary critically with the kinetic energy of secondary charged particles. The main limits in the achievable resolution of a BP position monitoring technique based on the detection of charged fragments are due to the multiple scattering suffered from charged particles inside the tissues and to the available statistics, that strongly depends on the dose delivered in a real treatment and to the depth of the tumor under treatment. Selecting only secondary charged particles with high kinetic energy values and increasing the detector geometrical acceptance would reduce the impact of the aforementioned limitations.

The secondary radiation energy spectrum, as well as its production rate (flux), have been measured: prompt photons (γ) in the energy range $1 \div 10$ MeV and charged particles (mainly protons) with kinetic energies up to 150 MeV have fluxes that allow the exploitation of such particles as monitoring probes during a real PT treatment. From an 80 MeV/u ^{12}C beam impinging on a PMMA phantom, the measured production rates are the following ($\Omega_{\mathrm{LYSO}} \sim 1.6 \times 10^{-3}$ sr):

$$\Phi^{\gamma}(\Omega_{\mathrm{LYSO}})_{E>2\mathrm{MeV},\theta=90^{\circ}} = (2.32 \pm 0.01_{stat} \pm 0.15_{sys}) \times 10^{-3}\ sr^{-1}\ ,$$

$$\begin{aligned}
\Phi^{P}(\Omega_{\mathrm{LYSO}})_{E^{\mathrm{Prod}}_{\mathrm{kin}}>7\ \mathrm{MeV},\theta=90^{\circ}} &= (0.761 \pm 0.014_{\mathrm{stat}} \pm 0.032_{\mathrm{sys}}) \times 10^{-4} sr^{-1}\ , \\
\Phi^{P}(\Omega_{\mathrm{LYSO}})_{E^{\mathrm{Prod}}_{\mathrm{kin}}>83\ \mathrm{MeV},\theta=90^{\circ}} &= (0.214 \pm 0.006_{\mathrm{stat}} \pm 0.009_{\mathrm{sys}}) \times 10^{-4} sr^{-1}\ .
\end{aligned}$$

Using a 220 MeV/u ^{12}C beam interacting with a PMMA, the measured production rates for secondary fragments such as protons (p), deuterons (d) and tritons (t) are ($\Omega_{\mathrm{LYSO}} \sim 2.1 \times 10^{-3}\ sr$):

$$\begin{aligned}
\Phi^{p}(\Omega_{\mathrm{LYSO}})_{\theta=60^{\circ}} &= (8.78 \pm 0.07_{\mathrm{stat}} \pm 0.64_{\mathrm{sys}}) \times 10^{-3}\ sr^{-1}\ , \\
\Phi^{d}(\Omega_{\mathrm{LYSO}})_{\theta=60^{\circ}} &= (3.71 \pm 0.04_{\mathrm{stat}} \pm 0.37_{\mathrm{sys}}) \times 10^{-3}\ sr^{-1}\ , \\
\Phi^{t}(\Omega_{\mathrm{LYSO}})_{\theta=60^{\circ}} &= (0.91 \pm 0.01_{\mathrm{stat}} \pm 0.21_{\mathrm{sys}}) \times 10^{-3}\ sr^{-1}\ ,
\end{aligned}$$

$$\begin{aligned}
\Phi^{p}(\Omega_{\mathrm{LYSO}})_{\theta=90^{\circ}} &= (1.83 \pm 0.02_{\mathrm{stat}} \pm 0.14_{\mathrm{sys}}) \times 10^{-3}\ sr^{-1}\ , \\
\Phi^{d}(\Omega_{\mathrm{LYSO}})_{\theta=90^{\circ}} &= (0.78 \pm 0.01_{\mathrm{stat}} \pm 0.09_{\mathrm{sys}}) \times 10^{-3}\ sr^{-1}\ , \\
\Phi^{t}(\Omega_{\mathrm{LYSO}})_{\theta=90^{\circ}} &= (0.128 \pm 0.005_{\mathrm{stat}} \pm 0.028_{\mathrm{sys}}) \times 10^{-3}\ sr^{-1}\ .
\end{aligned}$$

Starting from the measured fluxes, for a real PT treatment with a 220 MeV/u carbon beam, in a scenario considering a detector with an angular acceptance of $\Delta\Omega \sim 0.8 \cdot 10^{-1}\ sr$, for a deep seated tumor ($\sim$ 10 cm from the patient's skin), a delivered dose of 2 Gy and an energy threshold for protons exiting the target giving a $\sim$ 20% reduction of the statistics, the expected resolution on the BP linked parameters is $\sim$ 4 mm for a single pencil beam.

The obtained results from the described measurements fully supported the feasibility of a novel on-line dose monitoring technique based on the simultaneous detection of secondary neutral and charged particles. A dual-mode device, named *Dose Profiler* (DP), is under construction at the SBAI department laboratory (Sapienza University, Rome, Italy). Working as a Compton camera and a secondary charged particles tracker, the Dose Profiler principal aim is to provide a prompt feedback on the quality of the treatment during the patient irradiation time. The main DP constituents are the tracker, composed of six planes of orthogonal layers of scintillating fibers, an electron absorber, made of plastic scintillator, and a LYSO calorimeter. Such device has been designed to track both neutral and charged particles during a PT treatment, measuring the secondary particles emission distribution and correlating it to the dose release inside the patient. From the DP full Monte Carlo simulation performed using the FLUKA code, the expected spatial resolution on the reconstructed emission point of secondary fragments has been evaluated for a head tumor treatment: a resolution of $\sim$ 1 cm has been obtained for prompt photons while $\sim$ 0.4 mm have been obtained for secondary protons. Despite the discouraging outcome on prompt photons, it has to be noticed that in proton therapy, gamma production fluxes are two order of magnitude higher with respect to secondary charged particles fluxes and, moreover, prompt photons are not affected by MS. It has also to be noted that

the current algorithms and detector setting for the prompt photon detection and reconstruction have not been yet optimized.
The target resolution on the reconstructed Bragg peak position is ~ 2 mm, based on the beam range separation of the energy steps in a typical clinical treatment to create the Spread Out Bragg Peak in order to cover the whole tumor region.

The Dose Profiler device has been developed as part of the INSIDE PRIN project aiming for a combined multi-mode on-line dose release monitor, compact and manageable, that will be integrated in a treatment room at the CNAO center in Pavia (Italy) in 2016.

Bibliography

[1] J. Jackson, "Classical electrodynamics," *2nd ed. New York: John Wiley & sons*, 1975.

[2] H. Bethe and J. Ashkin, "Passage of radiations through matter," *Experimental Nuclear Physics*, vol. 1, 1953.

[3] W. Leo, "Techniques for nuclear and particle physics experiments: A how-to approach," *2nd ed. New York, Berlin, Heidelberg: Springer-Verlag*, 1994.

[4] R. Serber, "Nuclear reactions at high energies," *Physical Review*, vol. 72, pp. 1114–1115, 1947.

[5] J. D. Bowman, W. J. Swiatecki, and C. F. Tsang, "Abrasion and ablation of heavy ions," *(unpublished) LBL Report No LBL-2908 University of California*, 1973.

[6] R. Pleskac, Z. Abou-Haidar *et al.*, "The first experiment at gsi," *Nuclear Instruments & Methods in Physics Research Section A: Accelerators, Spectrometers, Detectors and Associated Equipment*, vol. 678, pp. 130–138, 2012.

[7] A. Ferrari, P. Sala *et al.*, "Fluka: a multi-particle transport code," *CERN 2005-10, INFN/TC-05/11, SLAC-R-773*, 2005.

[8] V. L. Highland, "Some practical remarks on multiple scattering," *Nuclear Instruments and Methods*, vol. 129, no. 2, pp. 497–499, 1975.

[9] T. Tabata, R. Ito *et al.*, "An empirical equation for the backscattering coefficient of electrons," *Nuclear Instruments and Methods*, vol. 94, no. 3, pp. 509–513, 1971.

[10] O. Klein and Y. Nishina, *Z. Physik*, vol. 52, pp. 853–868, 1929.

[11] U. Amaldi, "History of hadrontherapy in the world and italian developments," *Rivista Medica*, vol. 14, no. 1, pp. 7–22, 2008.

[12] R. R. Wilson, "Radiological use of fast protons," *Radiology*, vol. 47, pp. 487–491, 1946.

[13] C. Tobias, J. Lyman *et al.*, "Radiological physics characteristics of the extracted heavy ion beams of the bevatron," *Science*, vol. 174, pp. 1131–1134, 1971.

[14] E. Pedroni, R. Bacher *et al.*, "The 200-mev proton therapy project at the paul scherrer institut: conceptual design and practical realization," *Medical Physics*, vol. 22, no. 1, pp. 37–53, 1995.

[15] T. Haberer, W. Becher *et al.*, "Magnetic scanning system for heavy ion therapy," *Nuclear Instruments and Methods in Physics Research Section A: Accelerators, Spectrometers, Detectors and Associated Equipment*, vol. 330, no. 1, pp. 296–305, 1993.

[16] T. Haberer, J. Debus *et al.*, "The heidelberg ion therapy center," *Radiotherapy and Oncology*, vol. 73, no. 2, pp. S186–S190, 2004.

[17] *Centro di adroterapia e applicazioni nucleari avanzate. Available online: http://www.lns.infn.it/CATANA/CATANA/.*

[18] P. therapy co-operative group home. Available online: http://www.ptcog.ch.

[19] *Centro nazionale di adroterapia oncologica per il trattamento dei tumori. Available online: http://www.cnao.it.*

[20] *ICRU report 51, Quantities and units in radiation protection dosimetry. Bethesda, Md: International Commission on Radiation Units and Measurements, 1993.*

[21] E. Fokas, G. Kraft *et al.*, "Ion beam radiobiology and cancer: Time to update ourselves," *Biochimica et Biophysica Acta (BBA) - Reviews on Cancer*, vol. 1796, no. 2, pp. 216–219, 2009.

[22] D. Schardt, P. Steidl *et al.*, "Precision bragg-curve measurements for light-ion beams in water," *2008, GSI-Report 2008-1 (GSI Scientific Report 2007)*, unpublished.

[23] D. Schardt, T. Elsässer *et al.*, "Heavy-ion tumor therapy: physical and radiobiological benefits," *Rev. Mod. Phys.*, vol. 82, pp. 383–425, 2010.

[24] M. Scholz, "Effects of ion radiation on cells and tissues," *Radiation Effects on Polymers for Biological Use, ser. Advances in Polymer Science. Springer Berlin Heidelberg, 2003*, vol. 162, pp. 95–155.

[25] E. Hall, "Radiobiology for the radiologist," *Philadelphia: Lippincott Williams and Wilkins*, 2000.

[26] E. A. Blakely, C. A. Tobias *et al.*, "Inactivation of human kidney cells by high-energy monoenergetic heavy-ion beams," *Radiation Research*, vol. 80, no. 1, pp. 122–160, 1979.

[27] G. W. Barendsen, C. J. Koot *et al.*, "The effect of oxygen on impairment of the proliferative capacity of human cells in culture by ionizing radiations of different let," *International Journal of Radiation Biology*, vol. 10, no. 4, pp. 317–327, 1966.

[28] D. K. Bewley, "A comparison of the response of mammalian cells to fast neutrons and charged particle beams," *Radiation Research*, vol. 34, no. 2, pp. 446–458, 1968.

[29] Y. Furusawa, K. Fukutsu *et al.*, "Inactivation of aerobic and hypoxic cells from three different cell lines by accelerated 3he-, 12c- and 20ne- ion beams," *Radiation Research*, vol. 154, no. 5, pp. 485–496, 2000.

[30] A. Staab, D. Zukowski *et al.*, "Response of chinese hamster v79 multicellular spheroids exposed to high-energy carbon ions," *Radiation Research*, vol. 161, no. 2, pp. 219–227, 2004.

[31] T. Terasawa *et al.*, "Systematic review: Charged-particle radiation therapy for cancer," *Annals of Internal Medicine*, vol. 151, no. 8, pp. 556–565, 2009.

[32] *Heidelberg ion-beam therapy center (HIT). Available online: http://www.klinikum.uni-heidelberg.de.*

[33] B. Gottschalk and E. Pedroni, "Treatment delivery systems in proton and charged particle radiotherapy," *T. F. DeLaney and H. M. Kooy, Eds. Philadelphia: Lippincott Williams and Wilkins, 2008, ch. 5*, pp. 33–49.

[34] M. Durante and J. S. Loeffer, "Charged particles in radiation oncology," *Nature Reviews Clinical Oncology*, vol. 7, no. 1, pp. 37–43, 2010.

[35] H. I. E. Haettner and D. Schardt, "Experimental investigation studies with 12c therapy beams," *Rad. Prot. Dos.*, vol. 122, no. 11, pp. 485–487, 2006.

[36] E. Haettner, "Experimental study on carbon ion fragmentation in water using gsi therapy beams," *Master of Science Thesis, KTM, Stockholm*, 2006.

[37] A. Mairani, "Nucleus-nucleus interaction modeling and applications in ion therapy treatment planning," *PhD thesis, University of Pavia*, 2007.

[38] G. Battistoni, F. Broggi *et al.*, "The fluka code and its use in hadron therapy," *Nuovo Cimento*, vol. C, no. 31, pp. 69–75, 2008.

[39] C. P. Karger, O. Jäckel *et al.*, "Clinical dosimetry for heavy ion therapy," *Zeitschrift für Medizinische Physik*, vol. 169, pp. 159 –169, 2002.

[40] E. Pedroni and U. Schneider, "Proton radiography as a tool for quality control in proton therapy," *Medical Physics*, vol. 22, no. 4, pp. 353–363, 1995.

[41] K. Parodi *et al.*, "Pet imaging for treatment verification of ion therapy: Implementation and experience at gsi darmstadt and mgh boston," *Nuclear Instruments and Methods in Physics Research Section A: Accelerators, Spectrometers, Detectors and Associated Equipment*, vol. 591, no. 1, pp. 282–286, 2008.

[42] C. Agodi, F. Bellini *et al.*, "Study of the time and space distribution of β^+ emitters from 80 mev/u carbon ion beam irradiation on pmma," *Nuclear Instruments and Methods in Physics Research Section B: Beam Interaction with Materials and Atoms*, vol. 283, no. 0, pp. 1–8, 2012.

[43] K. Parodi, "On the feasibility of dose quantification with in-beam pet data in radiotherapy with 12c and proton beams," *PhD Thesis, Technische Universität Dresden Germany*, 2004.

[44] R. D. Badawi, U. Medical, D. S. of Guy's, and S. T. Hospitals, *Aspects of Optimisation and Quantification in Three Dimensional Positron Emission Tomography.* University of London, 1998. [Online]. Available: http://books.google.it/books?id=XH1RNAAACAAJ

[45] J. Pawelke *et al.*, "In-beam pet imaging for the control of heavy-ion tumour therapy," *IEEE Transactions on Nuclear Science*, vol. 44, pp. 1492–1498, 1997.

[46] P. Crespo *et al.*, "Direct time-of-flight for quantitative, real-time in-beam pet: a concept and feasibility study," *Physics in Medicine and Biology*, vol. 52, no. 23, p. 6795, 2007.

[47] K. Parodi, H. Paganetti *et al.*, "Patient study of in vivo verification of beam delivery and range, using positron emission tomography and computed tomography imaging after proton therapy," *International Journal of Radiation Oncology, Biology, Physics*, vol. 68, pp. 920–934, 2007.

[48] K. Parodi, W. Enghardt *et al.*, "In-beam pet measurements of β^+ radioactivity induced by proton beams," *Physics in Medicine and Biology*, vol. 47, no. 1, pp. 21–36, 2002.

[49] K. Parodi *et al.*, "In-beam pet measurements of β^+ radioactivity induced by proton beams," *Physics in Medicine and Biology*, vol. 47, no. 1, p. 21, 2002.

[50] P. Crespo *et al.*, "On the detector arrangement for in-beam pet for hadron therapy monitoring," *Physics in Medicine and Biology*, vol. 51, no. 9, p. 2143, 2006.

[51] C. H. Min *et al.*, "Prompt gamma measurements for locating the dose falloff region in the proton therapy," *Applied Physics Letters*, vol. 89, no. 18, p. 183517, 2006.

[52] E. Testa *et al.*, "Dose profile monitoring with carbon ions by means of prompt-gamma measurements," *Nucl. Instr. and Meth. Phys. Research B*, vol. 267, pp. 993–996, 2009.

[53] C. Agodi, F. Bellini *et al.*, "Precise measurement of prompt photon emission from 80 mev/u carbon ion beam irradiation," *Journal of Instrumentation*, vol. 7, p. P03001, 2012.

[54] ——, "Erratum: Precise measurement of prompt photon emission from 80 mev/u carbon ion beam irradiation," *Journal of Instrumentation*, vol. 8, no. 11, p. E11002, 2013.

[55] F. Bellini, T. T. Boehlen *et al.*, "Extended calibration range for prompt photon emission in ion beam irradiation," *Nuclear Inst. and Methods in Physics Research, A*, vol. 745, no. 0, pp. 114–118, 2014.

[56] J. C. Polf *et al.*, "Measurement and calculation of characteristic prompt gamma ray spectra emitted during proton irradiation," *Physics in Medicine and Biology*, vol. 54, no. 22, p. N519, 2009.

[57] S. Kabuki, K. Ueno *et al.*, "Study on the use of electron-tracking compton gamma-ray camera to monitor the therapeutic proton dose distribution in real time," *Nuclear Science Symposium Conference Record (NSS/MIC), 2009 IEEE*, vol. 745, pp. 2437–2440.

[58] T. Kormoll, F. Fiedler *et al.*, "A compton imager for in-vivo dosimetry of proton beams, a design study," *Nuclear Instruments and Methods in Physics Research Section A: Accelerators, Spectrometers, Detectors and Associated Equipment*, vol. 626Ð627, no. 0, pp. 114–119, 2011.

[59] B. Braunn, M. Labalme *et al.*, "Nuclear reaction measurements of 95 mev/u 12c interactions on pmma for hadrontherapy," *Nuclear Instruments and Methods in Physics Research Section B: Beam Interactions with Materials and Atoms*, vol. 269, no. 22, pp. 2676–2684, 2011.

[60] C. Agodi, G. Battistoni *et al.*, "Charged particle's flux measurement from pmma irradiated by 80 mev/u carbon ion beam," *Physics in Medicine and Biology*, vol. 57, no. 18, p. 5667, 2012.

[61] ——, "Corrigendum: Charged particles flux measurement from pmma irradiated by 80 mev u?1 carbon ion beam (*Phys. Med. Biol.* 57 5667)," *Physics in Medicine and Biology*, vol. 59, no. 23, p. 7563, 2014.

[62] L. Piersanti, F. Bellini *et al.*, "Measurement of charged particle's yields from pmma irradiated by a 220 mev/u 12c beam," *Physics in Medicine and Biology*, vol. 59, no. 7, p. 1857, 2014.

[63] K. Gwosch, B. Hartmann *et al.*, "Non-invasive monitoring of therapeutic carbon ion beams in a homogeneous phantom by tracking of secondary ions," *Physics in Medicine and Biology*, vol. 58, no. 11, pp. 3755 – 3773, 2013.

[64] Z. Abou-Haidar, C. Agodi *et al.*, "Performance of upstream interaction region detectors for the first experiment at gsi," *Journal of Instrumentation*, vol. 7, p. P02006, 2012.

[65] T. T. Böhlen, F. Cerutti *et al.*, "The fluka code: Developments and challenges for high energy and medical applications," *Nuclear Data Sheets 120*, pp. 211 – 214, 2014.

[66] Y. Koba, H. Iwamoto *et al.*, "Scintillation efficiency of inorganic scintillators for intermediate-energy charged particles," *Progress in NUCLEAR SCIENCE and TECHNOLOGY*, vol. 1, pp. 218–221, 2011.

[67] R. Brun and F. Rademakers, "Root: An object oriented data analysis framework," *Nuclear Instruments and Methods in Physics Research Section A: Accelerators, Spectrometers, Detectors and Associated Equipment*, vol. A389, pp. 81–86, 1997.

[68] W. Verkerke and D. Kirkby, "The roofit toolkit for data modeling," SLAC, Stanford, CA, Tech. Rep. physics/0306116, Jun 2003.

[69] S. Agostinelli *et al.*, "G4–a simulation toolkit," *Nuclear Instruments and Methods in Physics Research Section A: Accelerators, Spectrometers, Detectors and Associated Equipment*, vol. 506, no. 3, pp. 250 – 303, 2003. [Online]. Available: http://www.sciencedirect.com/science/article/pii/S0168900203013688

[70] J. Allison *et al.*, "Geant4 developments and applications," *Nuclear Science, IEEE Transactions on*, vol. 53, no. 1, pp. 270 –278, feb. 2006.

[71] K. Mosegaard and A. Tarantola, "Probabilistic approach to inverse problems," *International Handbook of Earthquake & Engineering Seismology (Part A), Academic Press*, vol. 237, 2002.

[72] R. E. Kalman, "A new approach to linear filtering and prediction problems," *Transactions of the ASME. Series D, Journal of Basic Engineering*, vol. 82, pp. 35–45, 1960.

[73] R. E. Kalman and R. S. Bucy, "New results in linear filtering and prediction theory," *Transactions of the ASME. Series D, Journal of Basic Engineering*, vol. 83, pp. 95–107, 1961.

[74] M. Krämer, O. Jäkel *et al.*, "Treatment planning for heavy-ion radiotherapy: physical beam model and dose optimization," *Physics in Medicine and Biology*, vol. 45, no. 11, p. 3299, 2000.